Particles in Complex Fluids

Daniëlle D. van 't Zand

A thesis submitted in fulfilment of the requirements
for the degree of Doctor of Philosophy
to the
University of Edinburgh
October 2009

Abstract

This thesis describes experimental studies of colloidal particles dispersed in solvents which themselves have phase transitions. One common definition of soft matter is: a material characterized by a mesoscopic length scale. This length scale is, for example, the colloid size or the ordered domain size. Here we combine a complex host with one characteristic length scale with dispersed particles that have a different size. It might be anticipated that new behaviour will occur. Two limits of particle characteristics are probed: the case of dilute sterically-stabilized particles and the case of a weak gel of attractive particles. The two systems are polymer particles dispersed in a phase-separating microemulsion and silica nanoparticles dispersed in a low molecular weight liquid crystal. In each system a temperature driven phase transition plays a crucial role. In the microemulsion case we observe how transitional and pre-transitional phenomena create effective interactions between particles and how new behaviour emerges in the host solvent in the late stage of the phase separation. We show that the pre-transitional clustering of the PMMA particles is due to an adsorbed layer of dodecane. Subsequently heterogeneous nucleation of the gas phase is seen. After phase separation has occurred in off-critical samples the particles remain in either the continuous or dispersed phase depending on the original microemulsion composition. In the late stage of the phase-separation the coalescence and coarsening behaviour changes significantly, after more material exchange between the phases has taken place. This behaviour is reminiscent of viscoelastic phase separation in polymer based samples.

In the liquid crystal case we discover the anisotropy of the liquid crystal persists over large length scales and modifies the local dynamics of the gel. Using electron microscopy and scattering techniques we demonstrate that the silica embedded in the liquid crystal forms agglomerates with a fractal structure. Rheological characterization demonstrates that the resulting composite is a gel. Investigation of the composite's local dynamics using x-ray photon correlation spectroscopy shows anisotropy and intermittency in the dynamics on significant length scales.

In both systems we have studied new behaviour seen due to the influence of one component on the dynamic characteristics of the other The pre- and post- phase-

transition phenomena are only crucial in the microemulsion case where the particles have purely repulsive interactions. Our results illustrate the subtle balances that occur in soft composite systems.

Declaration

I do hereby declare that this thesis was composed by myself and that the work described within is my own, except where explicitly stated otherwise.

Daniëlle D. van 't Zand
October 2009

Acknowledgements

I would like to thank a number of people for their inspiration and support during this project. Firstly I would like to thank my first supervisor Paul Clegg for his dedicated support en encouragement during this project en my second supervisor Wilson Poon for valuable input.

I wish to thank Andrew Schofield for supplying me with colloids and helping me out numerous times in the lab.

I thank Yuriy Chushkin and Lhoussaine Belkoura for welcoming me in their institutions, the ESRF and the University of Cologne, and collaboration. Thanks to the ESRF and SoftComp for providing funds for carrying out experiments.

Many thanks to Paul Harris and Eric Davidson, for their expertise and helpfulness. I am also thankful to Jane Patterson for her support during my PhD.

I am very grateful to Rut and Lucio for teaching me IDL on many occasions. Thank you Laurence for teaching me to do dynamic light scattering. I am very thankful to Job, whose guidance in the rheology experiments was indispensable.

I wish to thank Martin Li for valuable discussions in the lab about microscopy and research experiences. I am grateful to Grace for trying to teach me Korean cooking. Thank you Louisa, for taking me on so many trips, especially our journey to Poland. Many thanks to Iain for accompanying me in the writing experience for several months, and continuously feeding me.

I wish to thank Stefan, Esther, Sandra, Dennis, Maarten, and Robert for their online support.

Special thanks to my friends, to Iris for keeping me sane and for having lots of fun, and to Andy for not only the numerous colloids but also the education on beer and the road trips.

Thanks to John for being there.

Finally I would like to thank my family.

Contents

Chapter 1

Introduction

When different components are mixed a new material or composite can be formed with properties that are different to those of the individual components. In this thesis the properties of fluids that exhibits phase transitions with particles inserted are investigated.

1.1 Soft condensed matter

Soft condensed matter is the study of materials which are neither crystalline solids, nor simple liquids, but somewhere in between. Soft matter includes emulsions, colloids, surfactant solutions, foams, polymers, and powders. The study of soft matter is of high interest because of its wide variety of applications. Many soft materials are familiar, examples are soaps, paints, glues, viruses, talc, engine oil, bacteria, toothpaste, and foods like milk, mayonnaise and margarine. The mesoscopic length scale is the common feature in soft matter systems, and lies between the bulk (∼1mm) and atomic (∼1nm), see fig. 1.1. The behaviour of this type of material is not mostly influenced by the

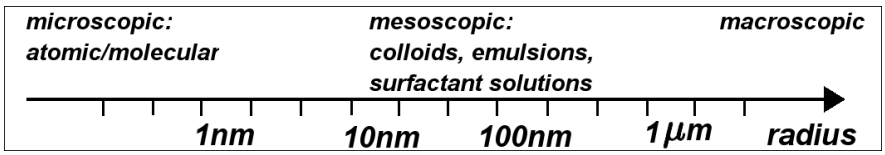

Figure 1.1: Mesoscopic length scales important in soft matter systems. Examples of soft matter systems are colloidal suspensions, proteins, surfactant solutions, and foams [1].

chemical composition of the material, but the relevant length scales dominate the physical behaviour of soft matter systems.

Colloids, micelles and macromolecules are small enough to undergo Brownian motion, which means that they are subjected to random forces from the thermal motion of the surrounding molecules [2]. Because of this soft matter systems are permanently moving, for example lipid membranes are not rigid, but are continually buckling and

stretching.

Soft matter has the ability to self-assemble, which leads to ordering that is generally intermediate between that of a crystalline solid and that of a liquid. Systems are able to move towards equilibrium when subject to external changes, which leads to phase behaviour. Typically colloidal particles are described as interacting with each other via an effective potential. This potential of mean force represents the relationship between the colloid and the host solvent. In the context of this thesis this is important - the phase behaviour and the likelihood of arrest out-of-equilibrium can be modified by changing the host solvent. By this route it is possible to control self-assembly without modifying the particles themselves.

1.2 Phase behaviour

Systems will always attempt to be in the lowest free energy state possible, its equilibrium state. When the fluid is in equilibrium large scale rearrangements will not occur because the system is in a stable state. However, this situation can be modified. The system can be subjected to a change in the environment, such as the increase of temperature, application of pressure or addition of a new component. It is possible to bring the system out of equilibrium in these ways and as a result the system will respond, trying to achieve a state in which it will be in equilibrium again. Under some circumstances the process by which the system attempts to move towards equilibrium again is dramatic. The system undergoes a 'phase transition', in which reorganization of constituents takes place [2–4]. This can be a phase transition from isotropic to nematic or liquid phase separation. Two processes by which a liquid system can undergo phase separation are 'spinodal decomposition' and 'nucleation', see fig. 1.2. In spinodal

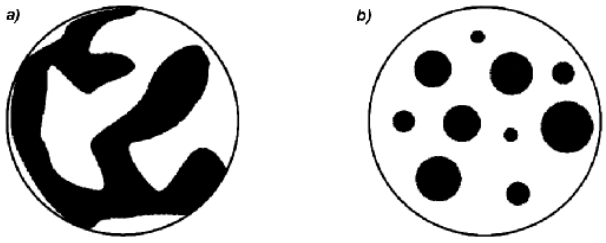

Figure 1.2: Schematic illustration of the structures that are observed in the early stage of phase separation. (a) Spinodal decomposition and (b) nucleation and growth [5].

decomposition phase separation takes place via a continuous change in the composition by means of diffusion, while in the nucleation process large enough nuclei of the new phase need to be formed for this phase to grow [5]. Liquid crystalline materials can change their phase upon increasing temperature, for example from nematic to isotropic

as illustrated in fig. 1.3

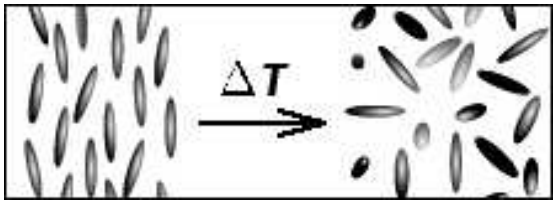

Figure 1.3: Phase behaviour example of liquid crystalline material, upon increasing temperature the molecular arrangement changes from nematic to isotropic.

1.3 Composite manipulation

In this thesis composites, in which two types of materials are combined, are the subject of study. Composites are interesting materials because the properties can be tuned via combining the appropriate components and via the preparation route. Usually a stiff and a flexible component constitute the composite. Via varying the relative amounts of the components the strength and stiffness of composite materials can be tuned to satisfy possible requirements. In other cases the composite can have properties unlike those of the constituents by themselves.

The composites that are examined in this thesis are fluids that can exhibit a phase transition with particles in them. The fluids used in the project are on one hand a microemulsion and on the other hand a liquid crystal. The phase transition process exhibited by the microemulsion is known as 'binary-liquid demixing', a process that can occur in two well-defined fashions depending on its chemical composition and the rate of temperature change: it occurs via spinodal decomposition or nucleation and growth. The process by which the liquid crystal displays the phase transition is the aligning of the liquid crystal molecules in a different arrangement to achieve equilibrium. This occurs via nucleation in the chosen system.

The properties of the microemulsion and liquid crystal systems are different when particles are added to them. When particles are embedded in the respective fluids new interactions will arise and the manners in which these systems attempt to achieve equilibrium can be modified.

The focus of this thesis is on investigating the properties of the composites before, during and after the phase transition has completed.

1.4 Thesis outline

Here we outline the layout of the rest of the thesis.

Chapter 2 presents the theoretical foundations of this thesis. We introduce colloidal systems and interactions between colloids. Surfactant systems and their phase behaviour are discussed as are liquid crystals.

In chapter 3 we introduce the experimental techniques that are used in these explorations. Initially the tools to observe the behaviour of the samples in real-time are discussed, such as optical, confocal and electron microscopy (EM). This is followed by an introduction on the scattering technique used to study the dynamics of systems: x-ray photon correlation spectroscopy. Finally rheology measurement techniques specific to the system under study are presented.

In chapters 4 and 5 the studies concerning the microemulsion with PMMA colloids inserted are presented.

Chapter 4 deals with the behaviour of the microemulsion with PMMA colloids inserted. Pre-transitional clustering of the PMMA colloids upon approaching the binodal via increasing the temperature is observed. This is found to be due to an adsorbed layer of dodecane. During the phase separation it is observed the PMMA particles partition in the gas phase, which is either the continuous or dispersed phase depending on the chemical composition of the initial microemulsion prior to the phase separation.

In chapter 5 the focus is on the late stage in the phase separation of the microemulsion with PMMA colloids inserted. Interestingly, the system is found to exhibit changed coalescence and coarsening behaviour.

Chapters 6 and 7 present the studies of the silica-5CB composite.

To start with the investigation of the structure of the composite using electron microscopy, static scattering and rheology is presented in chapter 6. The silica particles form agglomerates in the liquid crystal that are fractal in character and provide the liquid crystal with a yield stress.

In chapter 7 the dynamics of the silica-5CB composite are studied using x-ray photon correlation spectroscopy. Intriguing behaviour is observed, the dynamics are anisotropic on length scales larger than the local structure of the silica gel, and intermittent behaviour is observed.

Finally we draw conclusions and present suggestions for further investigations.

Chapter 2

Background

2.1 Background

The studies performed in this project both concern systems that exhibit a phase transition. In one case a phase separating microemulsion with colloidal particles inserted is studied, and in the other case a liquid crystal system exhibiting a isotropic-nematic transition with particles inserted is studied. In this chapter first phase transitions in general will be introduced, followed by the specific cases of phase transition occurring in the systems studied. The effect of particle surfaces prior to and during these transitions will also be described.

2.1.1 Phase Transitions

General considerations about phase transitions and critical phenomena

A phase consists of one or more components, and is uniform over its volume. An example of a phase can be a mixture of various gases or a liquid solution. Phases can coexist with each other, in which case the system is termed heterogeneous.

Any system will always try to be in the lowest free energy state possible, the equilibrium state. Here the system is stable and will not change. When a field variable, a variable that is always identical in coexisting phases, e.g. temperature, is varied, the current phase may no longer have the lowest free energy, a phase transition can occur [2]. This can be a phase transition from liquid to gas, isotropic to nematic, liquid to solid, unaligned system to ferromagnetic or liquid demixing. In a phase diagram of, for example, a simple fluid one can distinguish solid, liquid and gas states, see Fig. 2.1. The lines between the states are well defined phase boundaries; when a phase boundary is crossed there is a jump in the density and a latent heat, which is the amount of energy in the form of heat required for the material to undergo the change of phase. The quantity that changes (such as density, composition, orientation) at a phase transition is often called the order parameter. If the order parameter jumps discontinuously to

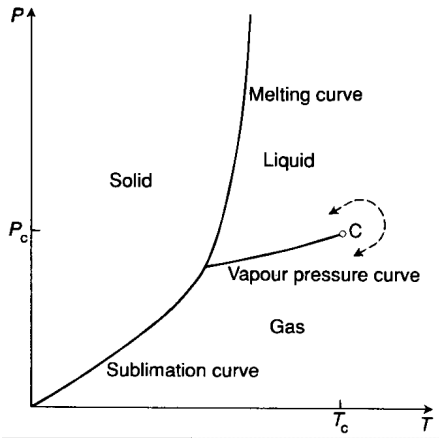

Figure 2.1: Phase diagram of simple fluid, figure adapted from [6].

a nonzero value the transition is first order, accompanied by latent heat and there is usually a jump in the entropy. If the order parameter rises continuously from zero the transition is second order and occurs at, what is called, the critical temperature T_c. In the case of gas-liquid phase separation depicted in Fig. 2.1 both first and second order transitions occur. The line of liquid-gas coexistence (at which a first order transition occurs) is not infinite, as the temperature increases the difference between the densities of the gas and liquid decreases continuously towards zero. It becomes zero at the *critical point*, above which it is possible to move from a liquidlike state to a gaslike state continuously rather than with a jump. The difference in densities is the order parameter for the liquid-gas transition. In a binary liquid mixture the order parameter for the transition, phase separation, is the concentration difference between the two liquid phases. The order parameter in liquid crystalline transition is related to the molecular orientation (see section 2.2). The phase behaviour of solutions of surfactants are determined mainly by the concentration of surfactant molecules (the solute) in water. When the surfactant concentration increases spherical micelles can form (see section 2.1.2), and a further increase of the concentration can lead to a phase transition from the spherical micellar state to a state consisting of micelles ordered in a hexagonal or cubic array where the intervening spaces are filled with water. In some systems a second transition to the lamellar phase can occur and sponge phases are also found. The definition of an order parameter can become increasing complex or ambiguous.

It is clear that there are many different kinds of phase transitions, and that they have several properties in common. The phenomena associated with continuous phase transitions are called critical phenomena, due to their association with critical points. A major feature of critical phenomena is that, when sufficiently close to a critical point,

all physical quantities vary as simple powers of the deviations of the field variables from their critical values [7]. There exist different *critical exponents* to describe the power law behaviour of different physical quantities of the system (e.g. heat capacity, correlation length and concentration difference between phases) that turn out to be true for various phase transitions, which means the exponents are *universal*.

In this project soft condensed matter systems (sections 2.1.2 and 2.1.3) exhibiting a phase transition are studied, a microemulsion and liquid-crystal system. A remarkable feature of the components of soft matter is that they can self-assemble in complicated arrangements without any assistance, which is the case in both surfactant and liquid-crystal systems. By changing an external parameter (e.g. temperature) a phase transition can be induced. First I study a micellar solution which shows a phase separation analogous to that exhibited by binary-liquid systems, with particles inserted. Second I study a liquid-crystal system which shows a isotropic-nematic transition with nanoparticles dispersed in it. The existence of a phase transition in both studies is crucial as are the dispersed particles. Soft matter has components of length scales intermediate between the atomic and macroscopic. The two systems under study in this project both contain two of such length scales. In the microemulsion system there are the micelles and the colloidal particles, and in the liquid crystal system there is the particles and the nematic domain size. In the following background relevant to the micellar system is outlined in more detail, starting with binary-liquid phase separation.

Phase separation occurs in binary liquid systems and elsewhere. When two liquids are put together it is likely they will be mixed or phase separate, depending on the state of the system described by the Gibbs free energy, $G \equiv H - TS$. For a system to be in equilibrium it needs to minimize its Gibbs free energy, which can be achieved via either increasing the entropy S or decreasing the enthalpy $H = U + pV$, in which U is the internal energy, a property that is determined by molecular interactions. Upon lowering the temperature the entropy term loses importance and the enthalpy term becomes more and more dominant, which means that the solution behaviour more and more depends on molecular interactions rather than entropy. Generally it is the case that the energy due to intermolecular interactions (van der Waals) between the same species is lower than that due to the intermolecular interactions between different species, which means that the system will be in a phase separated state at lower temperatures and mixed at higher temperatures. The result of this behaviour leads to a phase diagram with an upper critical solution temperature (UCST). When enough properties of the system are known, the phase behaviour of the system can be predicted as described below in the **regular solution model**.

There are systems, however, for which another miscible region occurs at lower temperatures, which means these systems have a lower critical solution temperature

(LCST). Upon lowering the temperature the two liquids mix. These systems exhibit stronger association forces at lower temperatures which creates additional behaviour to that described above. Cooling can induce mixing again, when interactions between the two components become more favorable due to, for example, the formation of hydrogen bonds. For most glycol ethers the binary mixture with water exhibits a LCST below which the mixture is completely miscible [8]. When hydrogen bonds are formed the entropy is affected, compositional entropy is gained, but orientational entropy is lost as hydrogen bond formation requires molecular alignment, which means that the total entropy can be decreased. Attraction due to hydrogen bonds is stronger than van der Waals attraction and hence lower the enthalpy more. The effect of the decrease of enthalpy is stronger than the increase of the entropy on the free energy, which means that this mixed state including hydrogen bonds is favorable at this certain temperature. When cooling further, more and more loss of entropy will be encountered when more and more molecules will align due to hydrogen bond formation. At some point the enthalpy does not lower the free energy enough to overcome the loss of entropy in this mixed state, and eventually the mixture will phase separate again to lower the free energy. This process is illustrated in this Fig. 2.2.

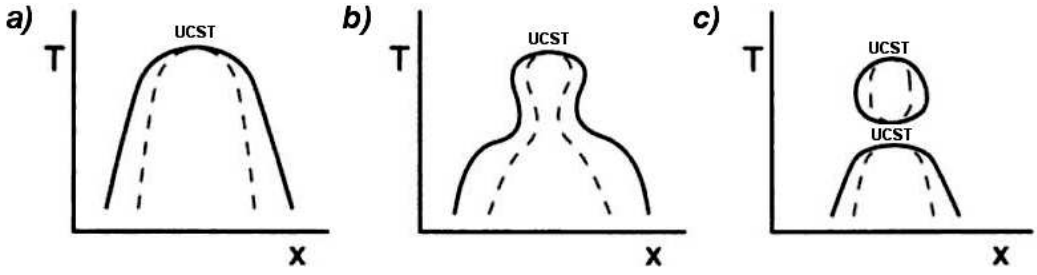

Figure 2.2: A simple illustration of a phase diagram of a binary liquid mixture. The binodal and spinodal lines are indicated. From (a) to (c) the association forces (e.g. hydrogen bonds) between the two components become stronger, figure adapted from [3].

Regular solution model, to find one shape of the free energy curve

The microemulsion system studied in the project shows a phase separation analogous to that of a binary liquid. To understand this example of a phase transition (liquid-liquid unmixing) the regular solution model can be used, which is a mean field theory [2]. The main idea in mean-field theory is to focus on one particle and its interaction with all other particles. The multi-body problem is then reduced to a one-body problem, and the interactions of the one particle is summed over all the particles present in the system. Here it assumed the volume remains constant, which means $H_{mix} = U_{mix}$, the change of enthalpy on mixing equals the change of energy on mixing.

To understand the phase behaviour of the system, it is the *free energy of mixing*

that needs to be predicted. By considering the possible arrangements of the phases in the mixed and unmixed state the entropy of mixing can be evaluated, and the intermolecular interactions determine the enthalpy. From using the equation for free energy $G = H - TS$ the free energy of mixing can be found [2]:

$$\frac{\Delta G_{mix}}{k_B T} = \phi_L ln\phi_L + \phi_G ln\phi_G + \chi\phi_L\phi_G \tag{2.1}$$

Here the free energy of mixing is expressed as a function of concentration of the mixture (expressed in volume fractions ϕ_G and ϕ_L), that depends only on the dimensionless parameter χ which expresses the strength of energetic interaction between the components. The shape of the curve of the free energy against composition changes with varying values of χ. Depending on the value of χ, the graph either has one minimum, or two minima separated by a maximum, see Fig. 2.3.

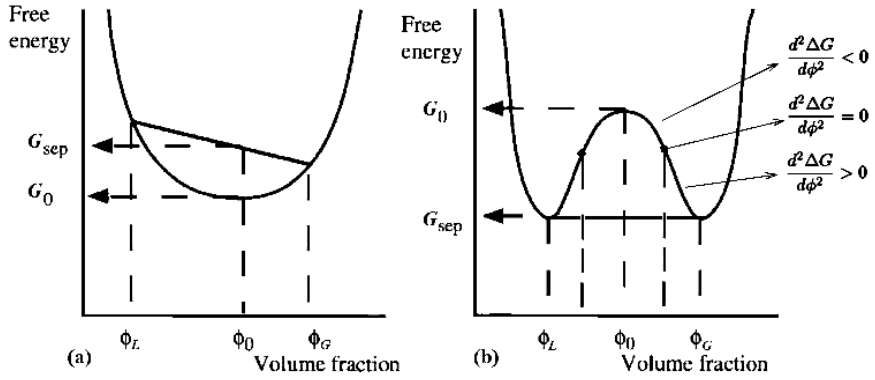

Figure 2.3: Free energy curves, figure adapted from [2]. In (a) χ has a low value, meaning that the interaction between the components is weak, and in (b) χ has a higher value, indicating stronger interaction between the molecules.

In the situation where there is only one minimum the system has the lowest free energy possible in the mixed state, denoted as G_0 in Fig. 2.3(a). When the system is brought to the situation that two minima exist in the graph (Fig. 2.3(b)), there are two compositions for which the free energy is the lowest, and the energy for the mixed state which here is then represented by the maximum, has a higher free energy and is thus an unstable state, because here the free energy can be lowered by phase separating into two phases, located near the minima in the graph. The two coexisting phases are joined by a common tangent from which their compositions can be found. For different temperatures, and thus different values of the interaction parameter χ, the location of the minima changes. These locations of the minima for different temperatures are known as the *coexistence curve* or the *binodal*, indicated in Fig. 2.4. For compositions that fall within the coexistence curve, which means between the two minima, the curve

has either positive or negative curvature. By considering what a small perturbation would do to the system, unstable and metastable regions of the curve can be identified. When the curvature is positive ($\frac{d^2G}{d\phi^2} > 0$) a small perturbation would lead to a slight increase in the free energy, which means no phase separation will happen. In this region larger perturbations will overcome an free energy barrier which is needed to be overcome to achieve the global free energy minimum. Compositions for which this is true, are called *metastable*. For regions where the curvature is negative perturbations of any strength will lead to phase separation, which means that these compositions are *unstable*. The local stability regions are separated by the locations where the curvature is zero, the locus of these points is known as the *spinodal*, indicated in Fig. 2.4. There

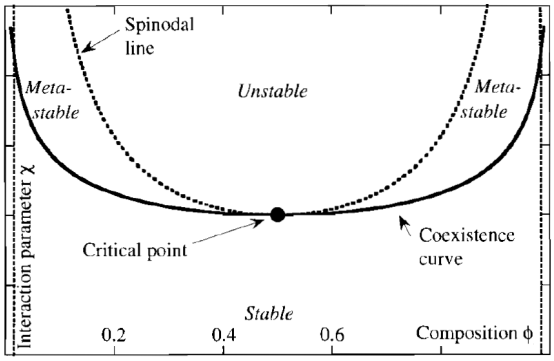

Figure 2.4: Phase diagram, figure adapted from [2]. The different stability regions as function of χ and composition are shown.

exists a critical temperature T_c, which is at the point where the binodal and spinodal line meet. The critical temperature separates the two situations, one for which the mixture is always stable and the situation for which there are compositions in which phase separation occurs. This is the point where no distinction can be made between the two situations just described, the critical point. At the critical point the phases are no longer distinguishable. Here the substance will have regions of phases of every possible size, which means that there will also be regions with the size comparable to that of the wavelength of visible light, and all wavelengths of light are refracted, which makes the solution appear milky or silvery. The shape of the free energy of mixing curve is now known as function of composition and the phase behaviour of the mixture. These relations make it possible to construct a phase diagram for the mixture, as illustrated in Fig. 2.4. A plot of the phase diagram indicates stability regions of the mixture as function of the composition and temperature. Summarizing, a binary liquid system, or analogous system showing similar behaviour, can be brought from a stable state to a metastable or unstable state by changing the temperature. This is also called 'quenching' the system into another state. A temperature quench into the

metastable or unstable region of the phase diagram will induce a phase separation as explained. Depending on in which region the system is quenched, it will phase separate via different mechanisms explained in the following section.

Phase separation kinetics, two mechanisms

Depending on the location in the phase diagram there can be systems having a composition that is either stable, unstable or metastable. Associated with this, the mechanism of phase separation will vary. In the part of the phase diagram where the mixture is unstable against any perturbation, phase separation will be spontaneous. Thermal fluctuations are enough to create any concentration fluctuations and phase separation occurs via a diffusive process referred to as *spinodal decomposition*. When the mixture is in the metastable part of the phase diagram, the phase separation process will take place only in presence of sufficiently large fluctuations which required to overcome the energy barrier needed to start this way of phase separating, *nucleation*. The nucleus must first overcome a critical size to be able to grow further in size. This process is termed *homogeneous nucleation*, which happens in a ideally pure system without impurities. The difference in phase separation pattern evolution is illustrated in Fig. 2.5. 'M' is a binary mixture composed of liquids 'a' and 'b', and depending

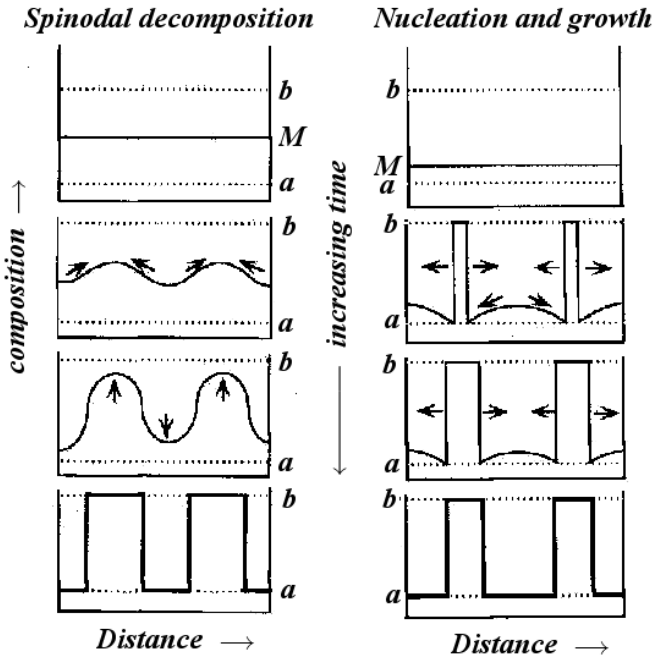

Figure 2.5: The final phases develop in different ways for spinodal decomposition (left) and nucleation and growth (right). Concentration fluctuations are amplified in the spinodal decomposition process, whereas in nucleation and growth large enough nuclei will grow further in size. Adapted from [3].

on the composition it will phase separate via either spinodal decomposition (left) or nucleation and growth (right). When the temperature of the binary-liquid mixture is changed such that unmixing will occur, the new phases will appear showing different pattern evolutions depending on the phase-separation mechanism. In the figure the time after the quench into the unstable region is indicated. Right after the quench the unmixing starts via either a diffusive process (left) or forming nuclei (right). The concentration fluctuation (left) in the spinodal decomposition process becomes stronger and eventually large regions of the new phases will have formed. The nuclei (right) will grow once they have formed.

Spinodal decomposition For a system to remain in an equilibrium state it needs to have a minimized free energy and uniform chemical potential. In the unstable region any concentration fluctuation leads to phase separation. Small fluctuations would lead to large amounts of interfaces and large fluctuations would grow very slowly since diffusion over long distances would be required hence there exists an optimal size of concentration fluctuation that will grow after forming. Phase separation in the unstable region is characterized by a single length scale and the mechanism is termed spinodal decomposition. Patterns created by spinodal decomposition are bicontinuous, and have a characteristic length scale that grows in time. Spinodal decomposition involves 'uphill diffusion', material diffuses against the concentration gradient. The spinodal pattern is termed self-similar, which means that the morphology found at different times only differs in scale which can be found experimentally for example with microscopy, which is true for experiments performed in the project (see Ch. 4). The domains grow to reduce the interfacial area in order to reduce the interfacial energy in the system. Initially the interfaces are not yet sharp but only diffuse, and phase separation mainly consists of diffusion. Later the compositions of the emerging phases approach the equilibrium coexisting compositions, and the interfaces have become sharp rather than diffuse. The system tries to reduce the amount of interface by coarsening, the phase separation is driven by the interfacial tension in this stage. At some stage in the growth the emerged domains will have reached such a size that gravity will become important because the two phases have different densities, and gravity induced convection will appear. Here the bicontinuous morphology no longer persists.

Nucleation In the metastable part of the phase diagram the mixture is stable against small changes in the concentration under influence of thermal fluctuations. Nucleation is an activated process, because upon the creation of new phase there is a positive contribution to the free energy because of the interfacial energy γ, but also there is a negative contribution to the free energy because new volume of the favoured phase is

formed.

$$\Delta F(r) = \frac{4}{3}\pi r^3 \Delta F_v + 4\pi r^2 \gamma \tag{2.2}$$

These contributions balance each other, which means that the fluctuation has to be sufficiently large to create a droplet of a large enough size ('critical size' r^*) for it to grow.

$$\Delta F^* = \frac{16\pi\gamma^3}{3\Delta F_v^2} \tag{2.3}$$

To reduce the interfacial area of the nucleating phase as much as possible the nucleating phase will always have a spherical shape during the formation of the new phase and neighbouring droplets coalesce with each other. The barrier for nucleation can be reduced by the presence of impurities or the walls of the container, these make it easier for the new phase to form droplets.

In this case the process is termed *heterogeneous nucleation*, rather than *homogeneous nucleation*, which is the case in absence of any impurities. When impurities are present in the system, the interfacial tension between the impurity and the newly forming phase might be lower than the interfacial tension between the two liquid phases. Because of this the free energy cost of forming the new phase can be lowered in the case of heterogeneous nucleation. In the microemulsion system the interfacial tension between the two phases is very low; $\gamma \sim 10^{-2}$mN/m [9], which means that the critical nucleus size will be small.

2.1.2 Surfactants and micelle formation

A surfactant (a contraction of the term 'surface-active agent') is a substance that,when present at low concentration in a system, can adsorb onto the surfaces or interfaces of the system and alter significantly the surface (or interfacial) free energies of those surfaces (or interfaces) [10]. The interfacial free energy is the minimum amount of work required to create that interface. This extra free energy that is created per unit area after forming the interface is called the interfacial tension γ. To increase the surface between two phases dA, there is γ amount of free energy required. The work required to form the interface is then $dw_{interface} = \gamma dA$.

Surfactants are an important type of molecule that can adsorb onto the interface and thereby change the amount of work required to create that interface. The characteristic molecular structure of a surfactant is that it consists of a structural group that has little attraction for the solvent, combined with a group that has a strong attraction for the solvent. In the case when water is the solvent the group with little attraction for the solvent is called hydrophobic and the group with strong attraction to the solvent is called hydrophilic (see Fig. 2.6). This amphipathic character of the surfactant

molecules means that already at very low concentration these are able to adsorb onto interfaces positively. Positive adsorption means that the interfacial energy is lowered upon the adsorption.

The hydrophobic group is usually a long hydrocarbon chain of some form, this can be a single or double, straight or branched chain, and in some cases can have a halogenated or oxygenated hydrocarbon or siloxane chain, the hydrophilic group is an ionic or highly polar group. In the microemulsion study the surfactant molecule used is sodium dodecyl sulphate (SDS), in which the single hydrocarbon chain is straight and the hydrophilic group is negatively charged, which means that the surfactant molecule is anionic.

Surfactant in water When dissolved in water the amphiphilic molecule has unfavorable hydrophobic interactions with the water (Ch. 4 in [11]), which means that the surfactant molecules will arrange themselves on the air-water interface to minimize the unfavorable interactions. On increasing surfactant concentration more and more molecules will adsorb onto the air-water surface until fully covered. At this surfactant concentration micellization, some kind of aggregation, occurs. The only way to avoid the hydrophobic tails of the surfactant being in the water is to form aggregates in which the tails are arranged together, see Fig. 2.6.

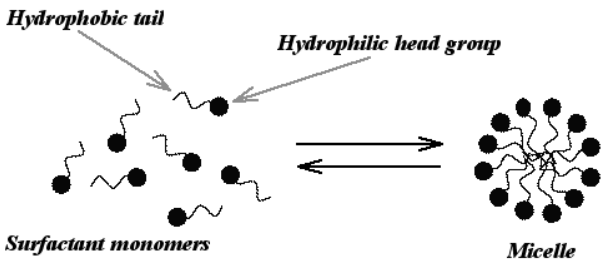

Figure 2.6: Schematic illustration of the micelle formation. The surfactant molecules self-assemble in aqueous solution to form micelles to reduce the free energy. To achieve this the hydrophilic heads are in contact with the water and the hydrophobic tails are in the center of the micelle to avoid contact with the water phase. The double arrow means that this is a reversible thermodynamic equilibrium. From [12].

This micellization occurs at a well-defined surfactant concentration, the 'critical micelle concentration' (CMC). Above this CMC there is the adsorbed monolayer at the surface, as well as free monomers and micelles of surfactant in the water phase. The concentration of monomers in the solution remains more or less constant when more surfactant molecules are added to the system. The shape of the micelle can vary, spherical, vesicles, bilayers or inverted micelles can be formed depending on the geometry of the surfactant molecule.

Surfactant in water and oil When surfactants are dissolved in a mixture of water and oil rather than only in water additional rich behaviour is exhibited. Surfactants can lower the interfacial tension between the oil and water and thereby stabilize droplets of one of the liquids dispersed in the other. This type of dispersion is called an 'emulsion'. There exist macroemulsions and microemulsions. The basic difference between macro- and microemulsions is the typical droplet size, for macroemulsions this is in the region of micrometer, whereas for microemulsions this is much smaller, typically smaller than 100 nm [13]. Because the size of droplets in macroemulsions is in the micrometer range, visible light is scattered and the emulsion appears to be a milky solution. In microemulsions the typical droplet size is smaller than 100 nm which means the system appears transparent. Systems for which the droplet size is in between the micro- and macro regimes are called miniemulsions (or nanoemulsion or submicron emulsion) [10, 13]. Both macroemulsions and miniemulsions are not thermodynamically stable but they are kinetically stable. To form this type of emulsion work has to be put in to create the system, which for example can be done via vigorous shaking. Because the surfactant molecules situated on the interfaces are in a dynamic equilibrium with surfactant molecules freely dispersed in either of the two liquids, the emulsion droplets can rearrange and reform. The stability of the formed emulsion is a function of time. The rate of coalescence can be very slow, but this is certainly not negligible.

In contrast, microemulsions are thermodynamically stable and can form spontaneously without the requirement of putting in energy. Microemulsion formation is dependent on the surfactant type and structure. In some cases the presence of one type of surfactant molecule in an oil and water mixture is not sufficient, in which case the presence of a *cosurfactant* is required to form a stable microemulsion. Schulman first noticed that addition of a medium length alcohol molecule to an emulsion stabilized by an ionic surfactant resulted in a transparent solution [14]. If the surfactant is ionic and contains a single hydrocarbon chain a microemulsion is only formed in the presence of a cosurfactant, see Ch. 5 in [11]. This is true for the microemulsion that is used in the project. The reason that microemulsions can form spontaneously is that the interfacial tension between the oil and water phases is very low. The main role of the surfactant is to reduce $\gamma_{o/w}$ by such an amount that spontaneous formation of droplets occurs and the system is thermodynamically stable.

In general microemulsions exist in equilibrium with either excess oil or excess water or both. Winsor classified four different general types of phase equilibria [15].

- I Surfactant is preferentially soluble in water : oil excess (2 phase).
- II Surfactant is preferentially soluble in oil: water excess (2 phase).

- III Three phase system in which a microemulsion maintains equilibria with both water and oil (3 phase).
- IV Single phase (isotropic) micellar solution that is not in equilibrium with either excess oil and/or water, that can form when a sufficient amount of surfactant and cosurfactant is present.

The microemulsion studied in the project (Chs. 4 and 5) is of type IV, see Fig. 2.7.

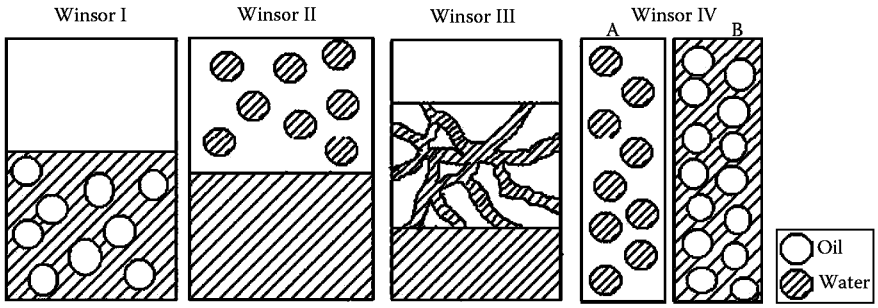

Figure 2.7: Different forms of the Winsor structures schematically. From [13].

Basics of formation of a microemulsion. To understand the spontaneous formation of droplets in the microemulsion, the oil and water system is considered to be a dispersion of one of the two phases in the other. The Gibbs free energy change when an interface is created has the following relation [13]: $\Delta G = \Delta H - T\Delta S + \gamma \Delta A$. When water and oil are mixed the enthalpy change is negligible, because there are hardly molecular interactions between oil and water molecules. In the case when the droplets are smaller, there is a positive change in entropy, which means in this case if the interfacial tension γ is sufficiently small that ΔG is negative and this is thus favorable [16]. The phase transition in the microemulsion arises from a balance between the entropy and interfacial tension (enthalpic contribution) [17]. The phase separation in the oil rich part of the phase diagram that can be interpreted as a liquid-gas transition is due to interactions between the inverse micelles.

Via conductivity measurements it has been found that there exists a percolation phenomenon in the microemulsion, on increasing micelle concentration a steep increase in the conductivity has been found [18]. The micelles form clusters that are dynamic and can rearrange in time [19]. The conductivity sharply rises when the liquid - gas transition is approached [20]. The van der Waals attraction between droplets may lead to a liquid-gas transition where each droplet plays a role similar to that of one argon atom in fluid argon [21]. Measurements of the second virial coefficient in microemulsion systems indicate that the critical point is characterized by large attractive interactions between the micelles [22]. The attractive interactions between micelles are found to be

strongly dependent on alcohol chain length (cosurfactant) [23]. The interactions are strongly attractive in microemulsions containing pentanol and much less in systems containing hexanol and heptanol. When pentanol is used as cosurfactant the aliphatic chains of the SDS can penetrate deeper into the oil phase which accounts for the stronger interactions between micelles. The stronger attractions found when pentanol acts as cosurfactant can explain the critical behaviour found in this system and not with longer chain alcohols [17].

The interactions between micelles involve the interpentration of surfactant chains into continuous oil phase [24]. The surfactant-oil and surfactant-surfactant interactions are almost equal, they both are long aliphatic chains. The oil molecules are not optimally oriented to interact with the surfactant molecules on the interface of the micelles at higher temperatures. The surfactant molecules on the other hand are optimally packed and oriented due to the micellar geometry and they thus can have a net attractive interaction. At low temperatures however the oil molecules are able to orient themselves at the micellar surface and interact with the surfactant molecules and thereby decreasing the surfactant-surfactant interactions. This leads to a lower critical solution temperature (LCST) [24].

The droplets diffuse and undergo collisions with each other which can sometimes lead the the rupture of the surfactant film if the collision is violent enough droplet exchange can occur. For the way this exchange occurs two mechanisms have been postulated [25]. Droplets can either (A) cluster or (B) fuse to form a transient unstable droplet dimer for a short period of time (microsecond timescale). In situation (A) species may diffuse through the surfactant bilayer at the point of contact between the droplets after which the droplets separate without having coalesced. In situation (B) the interface of the unstable transient dimer may have a fluctuating curvature on a fast timescale (sub-microsecond). If the dimer is sufficiently long-lived exchange of material between the two droplets is possible via diffusion. The unfavorable curvature of the surfactant film in this situation leads to the break up of the fused droplets. The droplet exchange process is believed to be activation controlled and not purely by diffusion only. The curvature observed in the microemulsion single phase is strongly determined by the exact microemulsion composition (see Ch. 5 in [11]) and is different from the natural curvature C_o, that is observed when the system contains equal amounts of oil and water. The natural curvature C_o depends on the surfactant type, as well as on the composition of the oil and water phases it separates. When the hydrocarbon tail of the surfactant is short, oily molecules can penetrate more easily in the surfactant film than when the tails would be longer. When more oil can penetrate in the layer, the curvature C_o will decrease, which means the surfactant film curves more towards the water. In case of an ionic surfactant, a decrease in headgroup area leads to a decrease in C_o which

means the film curves more easily towards water (water droplets in oil). Addition of electrolyte here has a strong effect: due to screening the headgroup effectively changes its area, when there is an increased salt concentration this area will be reduced. The addition of electrolyte in a system with non-ionic surfactant has little influence as there are no charges to screen. However the effect of temperature is very important, because the solubility in water of this type of surfactant is strongly dependent on temperature which means the curvature is affected by changing it.

Phase behaviour The phase of a microemulsion typically depends on composition, temperature and pressure. The appearance of phases can be investigated and presented in the form of a phase diagram. When an adequate representation is used, the phase behaviour can be indicated via the existence of single- or multi-phase regions, and via the equilibria between phases, which means that tie-lines and critical points are indicated. A tie-line is an isothermal (constant temperature) line that connects the compositions of phases at their equilibrium state. In general microemulsions contain at least 3 components, oil-water-surfactant, and sometimes a cosurfactant is added to tune the system stability. The system in the presence of a cosurfactant can still be considered as a 3 component system, as usually the ratio between two of the components is kept constant (in the case of the microemulsion system studied in my project the water-to-surfactant ratio is kept constant [26]). In this case, the phase behaviour of the 3-component system as a function of temperature at constant pressure can be represented in a phase prism, see Fig. 2.8.

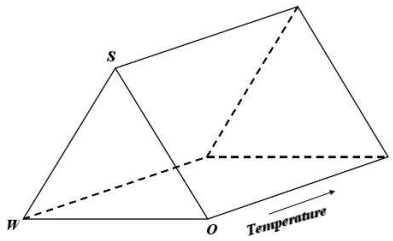

Figure 2.8: Phase prism representation of a microsmulsion system at constant pressure, figure adapted from [11]. The letters indicated in the phase prism indicate the following: s = surfactant, o = oil, and w = water.

This kind of representation is rather complex and it is useful to use simplifications by reducing the number of variables, for example represent the system not at constant pressure only, but at constant temperature as well. My research focuses of a ternary phase diagram of water-dodecane-pentanol-sodium dodecyl sulphate (SDS), shown in Fig. 2.9. In the microemulsion phase L_2, dodecane is the continuous phase, in which spherical [27] micelles (50-90 Å) composed of SDS, pentanol, and water are dispersed. Pentanol is used as a cosurfactant, to further reduce the interfacial tension $\gamma_{w/o}$ between

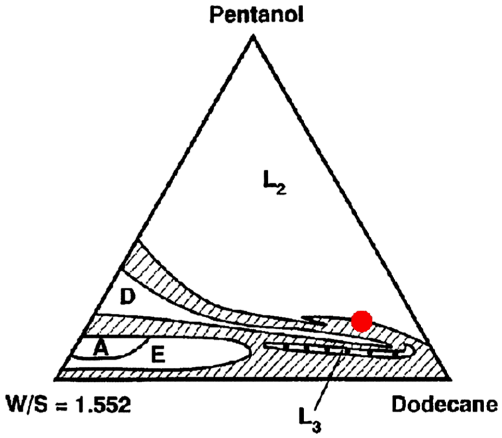

Figure 2.9: Ternary phase diagram of the four component system used in the project [26], T = 25^{o}C and $p = p_{atm}$, A: rectangular, D: lamellar, E: hexagonal, L_2: microemulsion, L_3: sponge, shaded: multiphase region.

the water and dodecane. Pentanol is partly dissolved in dodecane [28, 29]. The system has been intensively studied by Bellocq and Roux [26]. They present a detailed description of the quaternary mixture, which shows a variety of phases (Fig. 2.9). They investigated the effect of the water-to-surfactant ratio (X) on the behavior of the system in the microemulsion region. They found that by increasing the value of X, a phase transition can be induced. The system separates from a single-phase microemulsion to a two-phase microemulsion system, with compositions close to that of the single-phase microemulsion. For several fixed critical compositions varying from $X = 1.034 \rightarrow 5.172$, the authors investigated the effect of temperature. They found that by varying the temperature at constant composition, also a phase separation, as exhibited by binary-liquid mixtures, can be induced. In my project the water-to-surfactant ratio is fixed at $X = 1.552$. In the water-dodecane-pentanol-SDS system, the water to surfactant ratio is found to behave as a field variable, which means that the variable is always identical in the coexisting phases [30]. In the experiments, the oil-rich part of the phase diagram is studied. There exists a critical point on the coexistence line of the microemulsion L_2 region which is indicated with the red dot in Fig. 2.9. Starting from a composition in the homogeneous L_2 part of the diagram, a phase transition is induced by increasing the temperature, after which the sample will phase separate into two microemulsions with compositions close to the original microemulsion. Bellocq and Roux experimentally determined the phase diagram [26], which is presented in Fig. 2.10. The lines in the figure are coexistence lines at the indicated temperatures. For example, when one sits at 36^{o}C at a composition below the coexistence line, the system will phase separate into two phases. As can be seen from the phase diagram shown in Fig. 2.9, the system can have a composition close to critical or away from criticality. Depending on the

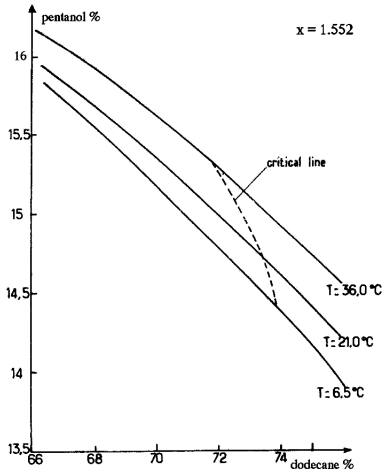

Figure 2.10: Experimentally determined phase diagram for the system with the water to surfactant ratio fixed at 1.552 [26].

composition, the system will have a phase transition via spinodal decomposition or via nucleation and growth.

A light scattering study on this system by Bellocq, Honorat, and Roux [31] provides evidence for a continuous variation of effective critical exponents in the system. They measured the critical phenomenon by its critical exponents ν and γ, which characterize, respectively, the divergences of the correlation length and the osmotic compressibility of the solution. They approached several critical points on a critical line, either by increasing temperature at fixed composition, or by increasing the water surfactant ratio at a constant temperature. The critical end point studied is located in the oil-rich part of the phase diagram. The critical line is located at the boundary between the single-phase microemulsion domain and the two-phase domain. The phase separation via spinodal decomposition in the microemulsion system was observed for the first time by Roux [32]. The spinodal decomposition was observed in a large region around the critical point (until 1^oC from the critical temperature). The peculiarity of the microemulsion critical behavior is the large value of the base correlation length ξ_0, The measured correlation length ξ diverges when one is approaching a critical point. The divergence follows a power law $\xi = \xi_0 \cdot \epsilon^{-\nu}$, where ϵ is the distance in ^oC from the critical point, and ν is a universal critical exponent in the temperature. The prefactor ξ_0 is not universal, the value is known to be related to the basic particle size. The large value of ξ_0 explains that spinodal decomposition in microemulsions occurs more slowly. The slow dynamics are an advantage, since this makes real-time studies possible.

Dorion et al. studied the dynamic behaviour in the microemulsion system by looking at the thermal conductivity and thermal diffusivity for samples with varying

water to surfactant ratio X [28]. Near the critical end point (CEP) the thermal conductivity $\wedge_{th}$ and thermal diffusivity $D_{th} = \wedge_{th}/\rho\bar{C_p}$ exhibit an anomalous increase when the temperature approaches the critical temperature, due to increased long range of interactions. A CEP occurs when a line of second order phase transitions is ended by a first order phase boundary, beyond which new non-critical phase is formed. (ρ denotes the mass density, and $\bar{C_p}$ the specific heat capacity.) Samples with critical points further away from the CEP show no critical behaviour in $\wedge_{th}$ or D_{th}. The microemulsion system studied in my project lies in this composition range located further away from the CEP.

A similar conclusion was drawn by Rebbouh and Lalanne [29], who investigated the behaviour of the refractive index near a CEP. At the critical temperature, the variation of the refractive index decreases sharply. The authors attribute the anomalous behaviour to the formation of transient clusters during the transition; these clusters can form, because the attraction between the micelles is stronger when the temperature is raised up to T_c.

The simultaneous measurement of the refractive index and density by Rebbouh et al. [33] confirmed the anomaly in the refractive index, but a density anomaly (correlated to that of heat capacity) was not observed. The authors conclude that the observed anomaly in the refractive index near the CEP is due to the chemical transfer of $n-$pentanol from the continuous phase (dodecane, $n-$pentanol) to the dispersed phase (SDS, water, $n-$pentanol) during the merging of micelles close to the critical temperature.

2.1.3 Colloidal interactions

A colloidal dispersion is a system in which solid particles or droplets in the size range 10 nm to 1 μm are dispersed in a solvent [2]. Because of the small colloid size the surface-to-volume ratio in colloids is large, which means relatively many molecules are on the surface of the colloid, leading to a significant amount of interfacial energy. The system can be carefully tuned via changing the surface chemistry of the colloids. The stability of a colloidal dispersion is a central issue - it is necessary to stabilize a dispersion both against gravity and against aggregation. Gravitational force can lead to the destabilization of a dispersion if the particles are large and the density difference with the surrounding medium significant; this will result in the sedimentation or creaming of the dispersed phase (the colloid). The Brownian motion of the colloids, random thermal motion, counteracts the influence of gravity when the particles are sufficiently small. Alternatively the density of the surrounding medium can be adjusted to reduce the effect of gravity. The colloids can show affinity for the solvent, in which case the

colloid is described as lyophilic ('solvent-loving') and such a dispersion is intrinsically relatively stable. Here the van der Waals attraction between the colloids is not strong because of the nature of the solvent. In the case when the colloids are lyophobic ('solvent-hating') the van der Waals attractions between the colloids tend to cause aggregation of the colloids. The origin of the van der Waals force is the interaction between fluctuating (induced) dipoles in neighbouring atoms or molecules. When two surfaces (of the colloids) approach each other there is an effective force arising due to the mutual interaction of all the pairs of molecules on the opposite surfaces. The van der Waals attraction F_{vdW} between two identical spheres of radius R that are separated by a distance h is given by [5]:

$$F_{vdW} = -\frac{A_H R}{12h} \tag{2.4}$$

where A_H is the Hamaker constant, which is related to the polarizabilities of the colloids and the solvent (tunable by varying the refractive index of the media).

Tuning the forces acting between the colloids is required to stabilize the dispersion against aggregation. This can be done by *charge stabilizing* the colloids with ionizable groups, so that the colloidal surface is positively or negatively charged. The ionizable group can dissociate if the colloids are dispersed in a polar solvent, which provides an electrostatic charge on the colloids. When then two colloids approach each other repulsion due to the charge arises between the colloids which prevents aggregation. Another way to stabilize the colloids against aggregation is *sterically*, by attaching long-chain polymers onto the surface of the colloids that prevent the colloids from approaching each other close enough for van der Waals attraction to become strong. If the adsorbed polymers do not interpenetrate, the stability of the dispersion will be increased by an 'elastic' effect. The close contact of colloids would lead to compression of one layer of polymer and will restrict the number of conformations available to each polymer chain. This decreases the entropy which means that the free energy will increase, and thus this effect is unfavourable. The effect is different if the polymer chains can interpenetrate into polymer layers from adjacent colloids. Provided that there is no effective attraction between the polymer segments, this interpenetration leads to an increase in the osmotic pressure between the colloids and hence causes a repulsive force.

In addition to van der Waals interactions the presence of a dispersed constituent (e.g. polymer molecules or micelles) can also cause alternative attractions between colloids. This has most often been studied for non-adsorbing polymers. Adding free polymer to a colloidal dispersion can result in a *depletion interaction* under certain conditions [1, 2], which is schematically illustrated in Fig. 2.11. The polymers' centers of mass are excluded from a region away from the surface of the colloid, the depletion

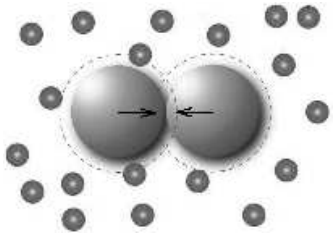

Figure 2.11: Depletion interaction. The polymers (or small particles) are excluded from a depletion zone near the surface of the colloidal particles. When the depletion zones of two large colloids overlap there is a net attractive force between the colloids resulting from unbalanced osmotic pressure.

zone. When the depletion zones of two colloids overlap the polymer molecules are excluded from this volume which means that the polymer concentration in this region is less than in the bulk solution. The resulting difference in osmotic pressure between the bulk solution and the depletion zone leads to a force pushing the colloids together. The depletion interaction can be used to tune the range as well as the depth of the attractive interaction. The range of the attractive interaction depends on the size of the polymer and the depth of the potential is proportional to the number density of polymers (which is responsible for the osmotic pressure). When assuming that the colloids are hard spheres and the polymers penetrable hard spheres, the depletion potential can be written as [1]:

$$W(h) = -\frac{3}{2} k_B T \phi_s \frac{\sigma_l}{\sigma_s} \left(1 - \frac{h}{\sigma_s}\right)^2, \tag{2.5}$$

in which ϕ_s is the volume fraction of the smaller particles (or polymer), σ_s and σ_b are the diameters of the small and large particles, and h is the distance between the two surfaces of the large particles. An attraction between 2 and 3 $k_B T$ will lead to phase separation of the colloids into two phases with different colloid concentrations. For example when the size ratio is $\frac{\sigma_l}{\sigma_s} = 10$, the depletion interaction will cause a phase separation or aggregation if the volume fraction of the small particles (or polymers) is about 20%.

2.1.4 Wetting, adsorption, prewetting

Wetting is a phenomenon in which three phases are coexisting, for example a liquid on a solid surface in equilibrium with its vapour phase (or instead of the solid another liquid) [34]. The liquid can behave in different manners on the solid depending on the intermolecular interactions. The three phases can be in equilibrium with each other in various ways, nonwetting (also called complete drying), partial wetting, complete

wetting or partial drying. The three phase contact line is the line where the three phases, solid, liquid, and vapour, meet. The liquid is in contact with the solid under a certain angle called the contact angle Θ, see Fig. 2.12 for an illustration. From

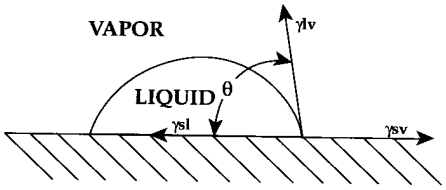

Figure 2.12: Contact angle and interfacial tensions, and thin adsorbed film.

the contact angle, the physical properties of interaction between solid and liquid like wettability, affinity, adhesiveness and repellency can be studied. The wetting behaviour is determined by the nature of both the liquid and the solid. There are four limits: non-wetting: $\Theta = 0^o$; partial drying: $0^o < \Theta < 90^o$; partial wetting: $90^o < \Theta < 180^o$; and complete wetting: $\Theta = 180^o$ [35]. The contact angle is a result of the interface/surface tensions, γ_{sl}, γ_{sv}, and γ_{lv} (surface free energies), between the liquid and solid surrounded by vapor, and is measured according to the Young's equation: $\gamma_{sv} = \gamma_{sl} + \gamma_{lv} cos\Theta$ [34]. γ represents free energy required to form a unit area interface. The Young's equation can be expressed in terms of the spreading coefficient C: $cos\Theta = \frac{\gamma_{sv} - \gamma_{sl}}{\gamma_{lv}} = 1 + \frac{C}{\gamma_{lv}}$, in which $C = \gamma_{sv} - (\gamma_{sl} + \gamma_{lv})$ [35]. In the case when there is partial wetting $0^o < \Theta < 90^o$, which means $0 < cos\Theta < 1$, the spreading coefficient is smaller than zero and thus $\gamma_{sv} > \gamma_{sl}$. Upon increasing temperature the liquid-vapour surface tension γ_{lv} decreases much faster than the other surface tensions $(\gamma_{sl} - \gamma_{lv})$, and at sufficiently high temperature there exists a wetting temperature T_w where C = 0 (unless the liquid reached its boiling temperature first), and thus $cos\Theta = 0$. The liquid phase spreads over the surface after the wetting transition, in which case $C > 0$. This type of wetting transition is first-order, the adsorption layer of a certain thickness jumps discontinuously to a large value at the wetting temperature.

In critical binary liquid mixtures a transition analogous to the first-order wetting transition can be found at the interface between the liquid mixture and a non-critical phase such as the container wall or the vapour phase. In the two-phase region there exists both wetting and adsorption, but this is different from the case when a substrate is in contact with a pure liquid rather than a mixture. In the mixture the liquid composition near the wall varies as a function of distance away from the wall surface, because one of the two liquid is likely to have a stronger affinity for the wall than the other. This is critical adsorption. In the case of a pure liquid in contact with a solid substrate there exists rather an adsorption layer of a certain thickness of the pure liquid

on the substrate.

At the interface with the wall critical adsorption films as well as prewetting films are found in the one-phase region. The prewetting films occur when the prewetting line is crossed, as illustrated in Fig. 2.13. In the two-phase region of a critical liquid

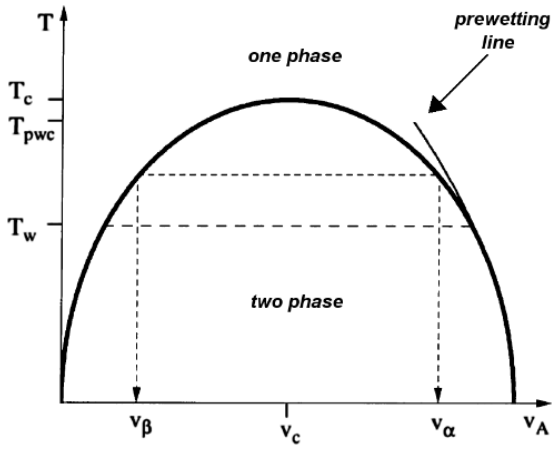

Figure 2.13: Schematic phase diagram (adapted from ref [35]) for a binary AB mixture which phase separates into a lighter α phase (rich in A) and a heavier β phase (poor in A) below the coexistence curve which is indicated with the heavy solid line. v_A represents the volume fraction of component A in the mixture. In the figure the prewetting line is indicated, which extends from the (first-order) wetting temperature T_w to the prewetting critical temperature T_{pwc} in the one phase region of the phase diagram.

mixture (A + B) wetting layers can exist under certain conditions. When the mixture is separated in two phases α (mostly A) and β (mostly B) one of these phases can be situated in the other phase as a droplet stuck the container wall or the liquid-vapour surface. For example a droplet of the heavier β phase can be suspended at the interface with the vapour (for a sufficiently small droplet the effect of gravity can be ignored). Here also a wetting transition can occur, which means a film of the heavier β phase can form on top of the α phase when the temperature is changed such that the spreading coefficient approached zero, like in the pure liquid droplet on the solid substrate - case. Recall that a wetting transition takes place when C = 0 which means that $\gamma_{\alpha v} = \gamma_{\alpha\beta} + \gamma_{\beta v}$ or $\gamma_{\alpha\beta} = \gamma_{\alpha v} - \gamma_{\beta v}$. When the temperature goes towards the critical temperature T_c the difference $\gamma_{\alpha v} - \gamma_{\beta v}$ will vanish eventually and a wetting transition occurs [36]. This difference vanishes as described by $\gamma_{\alpha v} - \gamma_{\beta v} \propto |T - T_c|^{\beta_1}$, where $\beta_1 \approx 0.8$ is a surface critical exponent [35]. There exists a prewetting line in the one-phase region of the phase diagram for binary liquid mixture. The behaviour at a composition where the prewetting line will be crossed as function of temperature will be discussed in terms of the interfacial tensions.

At high temperature (Fig. 2.13) the system is in the one-phase region and there only exists a very thin adsorbed layer. This is the lowest free energy state possible. Upon

lowering T however the prewetting line can be approached. When T = T_{pw} the free energy for a adsorbed film and a thick film is equal. For decreasing temperatures the layer thickness exhibits a jump between the adsorption film thickness and prewetting film thickness at T_{pw}. Between T_{pw} and T_{cx} (i.e. the temperature at which the coexistence line is crossed) the free energy for the adsorbed film thickness is a local minimum (metastable) rather than a global minimum like the free energy for the prewetting film thickness. When the temperature is lowered even further below T_{cx}, the mixture is in the two-phase region (after PS) and the prewetting film no longer is the lowest free energy, thicker films / regions are more favourable. Outside the region in the one-phase region between the coexistence curve and prewetting line there exists a equilibrium adsorbed film. Component A or B (one with lowest surface free energy) will preferentially adsorb at the surface (called critical adsorption near the critical point T_c). Wetting transitions can occur near substrates other than the container wall or the vapour, for example on colloidal particles that can be dispersed in the binary liquid mixture. Also in curved geometries like for example spheres wetting transitions and thin-thick transitions can occur [37]. The behaviour of binary liquid mixtures with colloidal particles dispersed in them is discussed in chapters 4 and 5.

2.2 Liquid Crystals

Liquid crystals (LCs) are materials that are partly ordered and exhibit intermediate phases ('mesophases') between their solid (crystalline) and liquid (isotropic) states. The molecules that show these 'liquid crystalline' (or mesomorphic) phases are called 'mesogens'. Liquid crystalline materials have properties that are in between those of a liquid and of a solid crystal. For example the material can flow like a liquid can, but the molecules are arranged similar to crystal planes. Typically these molecules have a core consisting of two or more aromatic rings, connected by central linking group, see Fig. 2.14(a). The core is generally rigid and planar and can have a dipole moment or

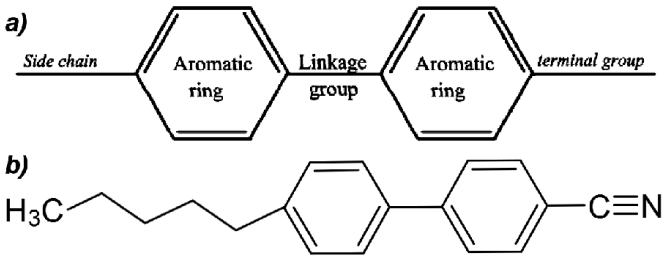

Figure 2.14: (a) Structure of rod-like liquid crystal molecule (mesogen), on both sides of the rigid core terminal groups or an aliphatic chain are connected. (b) Chemical structure of the liquid crystal compound, 5CB, used in the experiments carried out in the project.

is polarizable. The physical anisotropy of the molecules is also reflected in the optical properties of the liquid crystal molecules. The molecules are optically anisotropic, the refractive index measured along and perpendicular to the principal axis of the molecules is different, which results in birefringence which means that the texture can be identified with polarizing microscopy.

The molecules of the LC have an anisotropic shape (rods or plates) which makes that they can align along a certain direction. Well-known examples of these phases are the nematic and smectic phase. The liquid crystal molecules can form these phases under influence of varying temperature (thermotropic LCs) or the phases can form when certain solvents are added to the liquid crystal (lyotropic LCs). The work described here concerns the liquid crystal 5CB (4-cyano-4-n-pentylbiphenyl) which has a rodlike shape, see Fig. 2.14(b). The 5CB liquid crystal is thermotropic which means phase transitions are induced by varying the temperature. At low temperatures the LC exists in a crystalline phase, and upon heating it will form the nematic (N) phase and at sufficiently high temperature (T $> 35.3^{o}$C) the LC will be in the isotropic (I) phase, Fig. 2.15. The isotropic phase is the normal liquid phase in which the molecules are

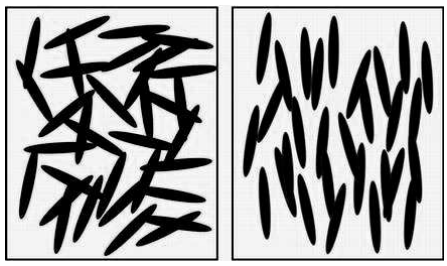

Figure 2.15: Schematic representation of isotropic (left) and nematic (right) phase, the phases occurring in 5CB. The temperature at which the nematic to isotropic transition occurs is 35.3^{o}C.

randomly orientated. In the nematic phase the molecules have a high degree of long-range orientational order, which means that they tend to align parallel to each other, but the positions of the centers of mass of the molecules are random (no long-range positional order). The preferred direction of molecular alignment can be described by a vector, which is called the 'nematic director' $\widehat{\mathbf{n}}$, which represents the average local direction of the long molecular axis and represents the direction of the optical axis. In reality the molecules in the nematic phase are not perfectly pointing all in the same direction, but on average the direction is well represented by the nematic director. The orientation of individual molecules can deviate quite a lot of that of the director, depending on thermal fluctuations. Describing the orientational order is mathematically complicated [38]. A measure of the alignments along the director is represented by the 'order parameter' (R). On a microscopic scale the long axis of each

rodlike molecule makes an angle θ with the nematic director, and the measure of order in the nematic phase can be given by the scalar order parameter $R =< cos^2\theta - \frac{1}{3} >$ [4], where $< .. >$ denotes that averaging takes place over all molecules. R = 1 is defined so that it corresponds to complete orientational ordering, while R = 0 indicates complete randomness. At the low end of the nematic range the order parameter generally has a value of about 0.7-0.8, and as the temperature is raised is falls to a value of about 0.3-0.4 just above the nematic-isotropic transition. This is illustrated in Fig. 2.16. The

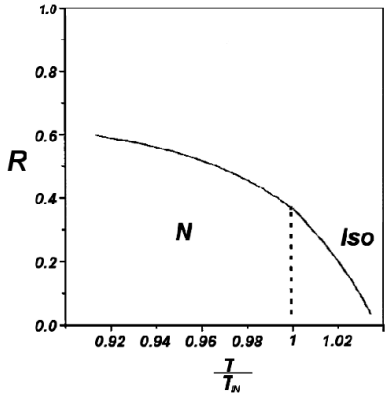

Figure 2.16: Illustration of how the order parameter R varies with temperature T (figure adapted from [39]). In experiment the order parameter does not drop as sharply as indicated in this figure with the dotted line (which is the result for Onsager theory), but decreases more continuously with increasing temperature as shown in the graph.

molecules on average point in the same direction, but still the system is liquidlike in terms of positions. The director is not the same throughout the bulk, there tend to be nematic domains with different orientation. Each domain will have a certain director and the transition from one domain to the other is smooth and continuous, which means that there are no real boundaries (unless there are defects). Possible defects are point and line defects can occur in pure nematic liquid crystal. The molecules can be radially aligned and point towards the point defect as shown in Fig. 2.17(a). The molecular alignment in Fig. 2.17(b) also leads to a point defect. Line defects are caused by molecular alignments as illustrated in Fig. 2.17(c) and (d).

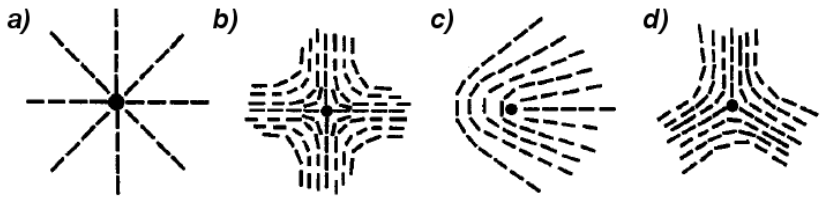

Figure 2.17: Orientation of the LC molecules leading to defects in the nematic order. From [40].

2.2.1 Colloids in liquid crystals

The order found in liquid crystals is distorted when colloidal particles are dispersed in it, and due to this distortion new interactions between the particles can arise. The distorted liquid crystal will induce additional interactions between inserted particles [41, 42]. The interactions between particles are modified because of the presence of the liquid crystal, the elastic distortions of the nematic director cause strong anisotropic elastic interactions between inserted particles [43]. The elastic forces arise due to deformation of the nematic director in the bulk nematic phase, and due to the anchoring of the molecules at the particle surface. Long range attractive interaction between particles are predicted and observed [44].

The addition of particles will disturb the nematic ordering which is energetically unfavourable. The long range orientational order, an elastic contribution (Frank free energy) to the total free energy, and also the anchoring energy of the molecules to the colloids, contributes to the total free energy [45]. The Frank free energy is a bulk contribution here and the anchoring energy represents a surface contribution. The free energy can be expressed as [46]:

$$F = F_b + F_s = \int \frac{1}{2} K[(\nabla \cdot \widehat{\mathbf{n}})^2 + (\nabla \times \widehat{\mathbf{n}})^2] d^3r - \oint \frac{1}{2} W(\widehat{\mathbf{n}} \cdot \widehat{v})^2 dS \qquad (2.6)$$

where W is the anchoring energy, $\widehat{v}$ is the unit vector normal to the surface of the particle, K is the average Frank elastic constant of the liquid crystal and $\widehat{\mathbf{n}}$ is the nematic director. The defects that are found in the nematic liquid crystal due to the presence of colloids depends on how strong the anchoring energy is. From equation 2.6 it is estimated that the surface contribution has a characteristic energy of the order WR^2 and the elastic cost of distortion around a single particle is $\sim KR$, and R represents the particle radius. Typical thermotropic liquid crystals tend to have an elastic constant of $K \sim 10^{-11} Jm^{-1}$ [47], which means that for a particle which has $R \sim 100$nm that the elastic energy cost $KR \sim 240 k_B T$. This means that the elastic energies will be large enough for the molecular configurations to remain stable against thermal fluctuations. Often, to classify the behaviour observed from the particles in the liquid crystal the dimensionless anchoring parameter $\frac{WR}{K}$ is considered. Here the surface anchoring energy and the elastic distortion energy are compared. There can be weak anchoring: $\frac{WR}{K} \ll 1$, here anchoring energy is weak compared to the bulk deformation energy and only small distortions of the director field are expected. In the case of strong anchoring $\frac{WR}{K} \gg 1$, which means that the energy cost for the nematic director to deviate from the anchoring alignment at the surface is high. The coupling to the particle is thus important and can determine how strongly the field is distorted.

How the nematic director is distorted close to a particle is determined by the orientation of the LC molecules at the particle surface. The LC molecules can orient themselves in various ways. They can have their molecular axis oriented parallel to the particle surface which is known as planar or tangential anchoring. Alignment of the molecules' principal axis perpendicular to the particle surface is referred to as homeotropic or normal anchoring, see Fig. 2.18.

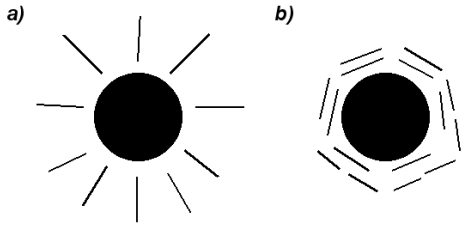

Figure 2.18: Schematic illustration of the anchoring of molecules at particle's surface. (a) Homeotropic anchoring and (b) planar anchoring.

This anchoring behaviour can be tuned by controlling the surface chemistry of the particles [48]. Because of the presence of particles the director field alignment is different at the surface of the particle compared to that found at large distances from the particle in the bulk LC. The presence of the particles creates a topological mismatch of the director field $\widehat{\mathbf{n}}$ between the director on the particle surface and the uniform director at large distances [49].

In the system studied in this thesis fumed silica particles (wacker) are dispersed in the liquid crystal 5CB. The particle's surface contains both hydroxyl and methyl groups. Because of the presence of the hydroxyl groups homeotropic anchoring of the LC molecules to the particle's surface is exhibited [50, 51]. The hydroxyl groups give the silica particles the ability to form hydrogen bonds, which enables them to form a gel. The homeotropic anchoring of the LC molecules at the particle's surface is strong, which causes a local distortion of the nematic director that results in an elastic strain in the LC. For the silica particles to form a gel in the LC the density must be larger than 0.1 g silica per cm^3 liquid crystal (represented as $\rho_s = 0.1$ g/cm^3) [51]. When the density is smaller than $\rho_s = 0.1$ g/cm^3 the gel is 'soft', which means that the bonds between the particles can break more easily which allows rearrangements of the particles. The particles rearrange to form a network of a configuration such that the elastic energy (and thus elastic strain) is minimal. When the gel is 'rigid', for densities above $\rho_s = 0.1$ g/cm^3, the bonds between the particles are strong because they are closer to each other. The stronger bonding between the particles has the effect that the rearrangement of the particle network is prohibited and the elastic strain can not be minimized (it is quenched).

Chapter 3

Experimental Background

In this chapter experimental techniques used in this thesis are discussed. The systems in this project are studied using a variety of techniques, depending on the data required. For observing the behaviour of samples real-time microscopy techniques were used, such as optical, confocal, and electron microscopy (EM). The different microscopy techniques were used depending on the nature of the sample studied. Other samples, with not much transparency for visible light, required the use of x-ray photon correlation spectroscopy (XPCS) to study the behaviour of the sample.

3.1 Microscopy

For observing small structures and detail a microscope system is needed. To resolve smaller features than the eye can make out, a magnifying system is needed. By using a single lens magnification up to ten times can be achieved. For obtaining larger magnifications, as required in this project, a compound system of lenses is used; a microscope. In the experiments performed in the project an Olympus BX50 optical microscope and Nikon E800 Eclipse are used.

3.1.1 Principles

Commonly used is the infinite tube compound microscope, in which the objective, the tube lens and the eyepiece are used for image formation, see Fig. 3.1. The objective lens collects the light coming from the specimen and forms a magnified image at an infinite distance. This light, basically a parallel beam of infinite focus, is collected by the tube lens which then produces a magnified (intermediate) image at the eyepiece. The eyepiece magnifies the image that is then observed by the user (directly or via a digital camera (charged coupled device or CCD)). The tube lens ensures that only the adjustment of the objective lens is needed when focusing a specimen. In absence of the tube lens both the objective and eyepiece positions would have to be adjusted.

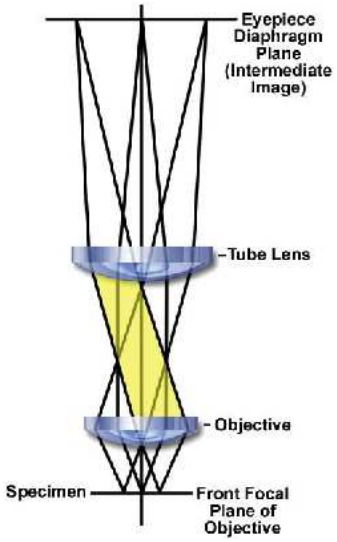

Figure 3.1: Schematic diagram of an infinite tube length compound microscope, image adapted from [52].

The magnification observed is the product of the magnifications of the various lenses in the microscope (objective, tube lens and eyepiece). The resolving power r of the microscope is given by the minimum distance between two objects which are seen as separate. The light from the cover glass of the specimen to the objective travels through air, which means that the light is deflected because the light experiences a difference in refractive index n; $n_{air} < n_{glass}$ (Snell's law). Because of this refractive index difference the exit angle will be larger than when the light would travel through material with a constant refractive index, which means that only a fraction of the light will be collected by the objective, see Fig. 3.2. When immersion oil is inserted between the cover glass and the objective, refraction of the light is eliminated, because the refractive index of the oil matches that of the glass ($n_{glass} \simeq 1.515$), and a larger cone of light can be collected by the objective. Lenses that can collect light over a wider angle give better resolution (capture of diffracted rays). This depends on the objective angular aperture, which is described in terms of the *numerical aperture* (NA) as $NA = n \cdot sin\theta$, where n is the *refractive index* of the medium between the lens and the sample, θ is the angle of the cone of light with the optical axis. Larger numerical apertures can be achieved using immersion oil.

The occurrence of diffraction also limits the resolution of the microscope. When a point-like object is imaged through a circular aperture a diffraction pattern known as the *point spread function* is produced [53]; and the image owill produce an *Airy pattern*,a circular symmetric intensity pattern, see Fig. 3.3. When there are two objects close to each other, they will produce an intensity pattern given by the superposition of their

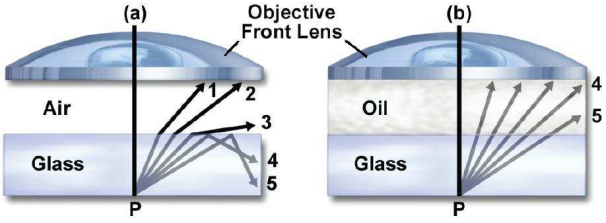

Figure 3.2: Illustration of the effect of immersion oil on the numerical aperture (NA) of the objective. When immersion oil is used a larger range of angles can be collected by the objective. Schematic adapted from [52].

point spread functions, and they are resolvable on the image plane if their diffraction patterns are sufficiently far apart. This is known as the *Rayleigh criterion*; two points will be resolved if the maximum of the Airy pattern of one point falls at a distance equal or larger to the position of the first minimum in the Airy pattern of the other point. For the resolution it follows, [53]: $r = \frac{0.616\lambda}{NA}$, where λ is the wavelength of the illuminating light. The resolution is determined by the NA rather than the magnification of the used objective. Using objectives with larger numerical apertures and using light of shorter wavelength improve the resolving power.

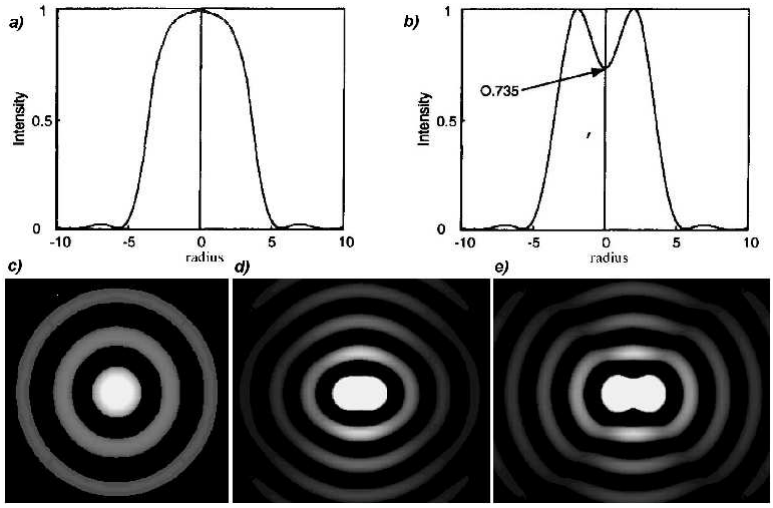

Figure 3.3: In the top two graphs the normalized intensities for one and two Airy patterns. The two points producing the airy patterns can only be separated if they are far enough apart so that a minimum of 26.5% less intensity exists between their maxima, as is indicated in the graph on the right [54]. In image c) an Airy pattern for a single point is shown. The diffraction pattern of two points does not fulfill the Rayleigh criterion d), a the patterns of two points which do e). The birightness of the secondary rings has been artificially increased to make them more clearly visible. Figures adapted from [55].

Optimum image quality is obtained when all components are aligned optimally, a configuration called Köhler illumination. In this method bright and even illumination in the specimen plane and in the observation plane is obtained. The light coming

from the sample is focused on the front focal plane of the objective, which in turn produces an intermediate image onto the eyepiece plane. The eyepiece lens together with the camera (eye) lens produce a focused image of the sample onto the observation plane (camera or retina). In the following schematic both the illuminating rays and the imaging rays are illustrated [52]. The image quality is influenced by aberrations

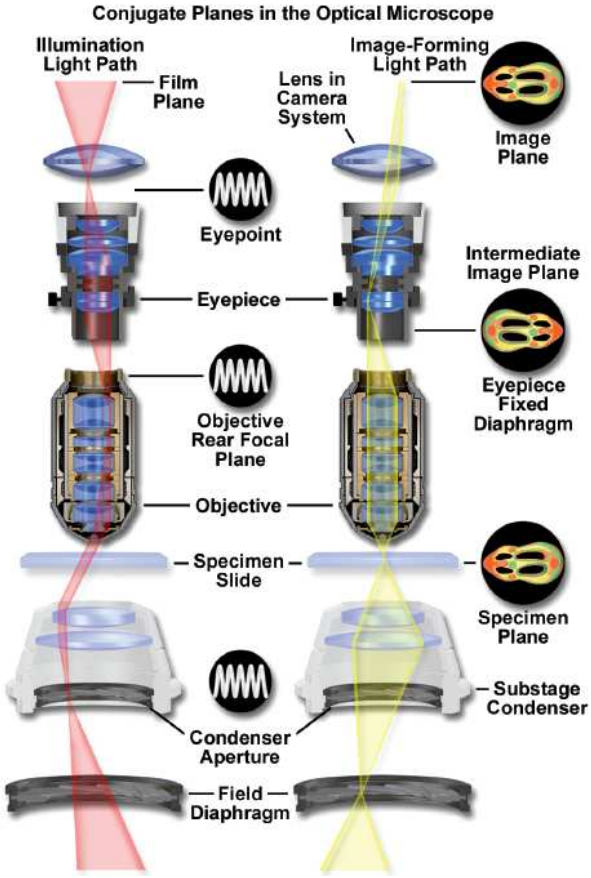

Figure 3.4: Light path in Köhler illumination, a given point in the light source illuminates every point in the specimen. Schematic adapted from [52].

present in the microscope. The major aberrations are chromatic aberration, spherical aberration, coma, astigmatism, curvature of field, and distortion [53]. Chromatic and spherical aberration are important factors that are taken into account in the experiments performed in the project. When light travels between media with different refractive indices it is deflected, for example between glass and air. The larger the angle of incidence, the stronger the deflection. The presence of the coverslip will lead to different optical path lengths being created depending on the angle of incidence. Light that passes over a larger angle will be in focus at a different depth compared to light that passes under a small angle (close to the optical axis), which leads to

blurring. Lenses can be corrected for spherical aberration, and are intended for use under a specific set of working conditions. These include the coverslip thickness, the assumption that the focal plane is at or near the coverslip surface, the refractive index of the medium between the lens and coverslip, the wavelength of illumination, and other conditions [53]. Thus, microscopists using well-corrected lenses can unknowingly induce spherical aberration by using coverslips having the wrong thickness or refractive index [56]. There exist objective lenses that are equipped with collars that allow the movement of the lenses within the objective to adjust for different coverslip thicknesses. In Fig. 3.5 it is schematically shown how a coverslip induces spherical aberration.

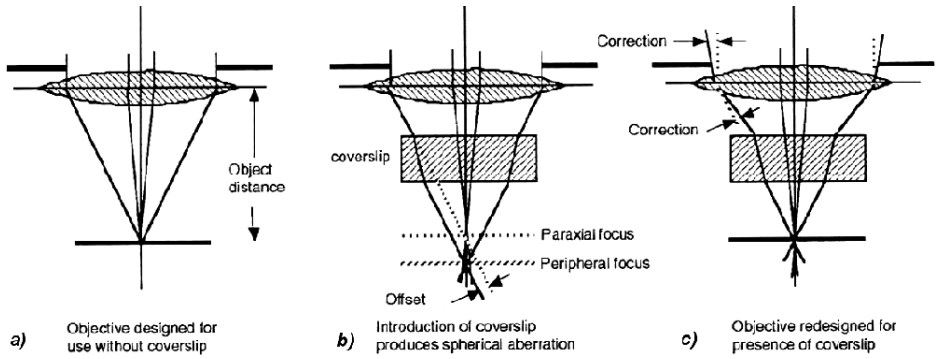

Figure 3.5: Light rays that have a larger angle of incidence (peripheral) are deflected more strongly when traveling through a medium with a different refractive index (a). This makes that spherical aberration occurs (b) when a coverslip is present. In (c) this is corrected for. Figure adapted from [57].

The image quality depends not only on the microscope set up, but also on the manner in which the images are captured. Image capturing is achieved via the use of a CCD charge-coupled device) camera. The camera used in the project is a Q-Imaging 3.3 RTV camera. The CCD is a photon detector consisting of many pixels (picture elements) that each store information (intensity) from incident photons that make up the microscope image. The dividing of the optical image formed by the microscope into pixels on a rectangular grid is a process referred to as 'sampling'. The digital image is described by coordinate positions and the light intensity at each coordinate position is represented by a positive integer. Incident light generates photoelectrons in each pixel, with their number being proportional to the number of absorbed photons [58]. Silicon is used as a photon-sensitive material in the CCD camera; incident photons interact with the silicon which leads to the generation of photoelectrons. At each pixel the incident intensity is averaged over the area of the pixel, after which this intensity is quantized at each sample point to produce an integer representing gray scale value. The resolution obtained depends not only on the size of the pixels, obviously the smaller the pixel size the better resolution. Also, photons with different wavelengths have

different energies, which means that they produce different numbers of photoelectrons in the silicon substrate in the pixel. Thermal energy can generate electrons in the pixel, which contributes to the signal thereby reducing the resolution (thermal noise).

3.1.2 Specimen characteristics

Optical microscopy can be used to produce images in which sub-micron features are resolved. For obtaining good results, the specimen can not be too thick, due to the presence of stray and background light. The specimen is uniformly illuminated which induces a large background illumination. Light coming from different focal planes all contribute to the formed image. When working with more dense samples, for example at a higher colloid concentration, the light scattered by the sample components also contributes to noise in the image, and the amount of light transmitted through the sample is reduced.

Using *fluorescence microscopy* can resolve the problem of background illumination. In this technique the specimen is tagged with a fluorophore, a molecule that can absorb radiation at a specific wavelength, then becomes excited and emits light at a longer wavelength (after losing some energy non-radiatively). Unwanted excitation light can be filtered out, so that only the emitted fluorescent radiation is collected. In this technique unwanted background illumination is eliminated, but still the fluorescent light coming from all the illuminated volume in the specimen is collected in the objective's numerical aperture. This means that also stray light from out of focus planes is collected, which increases the noise. For eliminating out-of-focus light a confocal set up is needed, as described in the next section.

3.1.3 Confocal microscopy

Experiments were performed in the project using the Biorad T800 Nikon. In a confocal microscope, light is only shone on a small spot of the sample and the signal is collected by a detector that sits behind a screen with a pinhole [59]. By moving the sample under the point illumination it is possible to construct a full image of the sample. It is the screen with a pinhole that enables to collect the light coming from in focus planes, whilst light coming from out-of-focus planes is not collected, see the illustration in Fig. 3.6.

Only light coming from the focus of the objective is transmitted through the pinhole and therefore detected, whilst the light coming from other depths are hardly transmitted through the aperture. This ability to discard background light is known as *optical sectioning*, which makes it very convenient for using to image dense systems and obtain sharp images. This is the principle used in modern laser-scanning confocal microscope

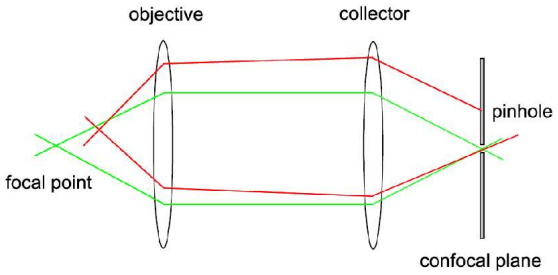

Figure 3.6: Schematic of the capturing of light from in-focus planes, whilst light from out-of focus planes is eliminated via the use of a pinhole. In this illustration only the light coming from the objective focus (green) is passed through the pinhole aperture in front of the detector, whilst light coming from other, out-of-focus, planes are screened (red). Figure adapted from [55].

(LCSM). Here a laser beam (with a chosen wavelength) is scanned across the sample by a pair of mirrors, which is then passed through the microscope objective and the fluorescent sample is excited. The emitted fluorescent light returns along the same optical path, but passes through the dichroic mirror, and before it reaches the detector (photomultiplier tube (PMT)) it is filtered by a pinhole. The pinhole aperture in front of the detector sits on the conjugate focal plane of the illuminated spot in the sample (hence the name confocal). The design of a LSCM is schematically illustrated in Fig. 3.7.

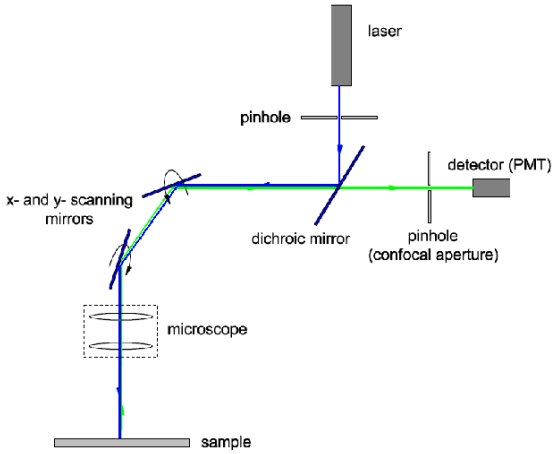

Figure 3.7: Schematic diagram of a laser scanning confocal microscope highlighting the main components. The illuminating beam is displayed as blue, and the emitted beam as green. Figure adapted from [55].

The dichroic mirror in the design has the property that it transmits light above a certain wavelength and reflects it below. In the set up the dichroic mirror is selected to transmit the fluorescent light emitted by the sample but to reflect the illuminating light. The light source can be monochromatic, or if not, the light can be filtered by

an excitation filter which selects only the light of the wavelength needed to excite the fluorophore in the sample. The emitted light is focused by the objective and transmitted through the dichroic mirror and finally imaged onto the image plane (detector).

3.2 Electron Microscopy

For studying the arrangement of the particles in the liquid crystal electron microscopy is an important tool. The scattering in the sample is so strong that optical microscopy is made impossible as hardly any light is transmitted. Using electron microscopy, features down to the size of the individual particles can be resolved and also their arrangement. The experiments were performed in Cologne with dr. Lhoussaine Belkoura using an EM 912 Omega instrument.

Transmission Electron Microscopy

The major driving force for developing the electron microscope (EM) was the desire to overcome some of the limitations of the light microscope. Using electrons with wavelengths much less than 1Å the resolution of the EM is higher than that of the light microscope. In the TEM, the electrons are emitted by a thermionic electron gun when heated [60]. The filament cathode is heated up to the point that it gives off many thermionic electrons, that are then accelerated towards an anode (typically ∼100 keV) and pass through a hole in its center to the condenser system of the microscope. The beam of electrons are focused using electromagnetic lenses and transmitted through the specimen. For creating contrast in the image the scattered and unscattered electrons need to be separated using the objective lens aperture. The image is recorded by exposing a photographic film (or plate) directly to the electron beam, or nowadays, by exposing a high-resolution phosphor that is coupled to the sensor of a CCD camera (via a lens optical system or fibre optic light guide).

Conventionally transmission electron microscopy (TEM) of dispersions of particles in liquid matter does not reveal the actual sample arrangement, only the solid components are used for imaging. Samples studied with conventional EM cannot contain liquid components, as these will evaporate within the microscope when the grid is inserted inside in the vacuum controlled sample-chamber (and can damage the microscope) [60]. Solvent evaporation inside the microscope would cause the vacuum to drop and also reduce the imaging quality significantly, as the electrons are strongly scattered by gas molecules. After depositing a drop of the dispersion onto the grid (with or without using blotting) particles present in the sample will self-assemble on the grid surface due to evaporation of solvent and induced capillary forces [61]. This method is good if one is interested in determining the particle size, but if one would want to study the sample structure as it is in bulk solution, the method of freeze-fracture needs to be

used [62]. Here the sample of interest is studied in the frozen state, which is achieved by inserting the sample as fast as possible in liquid ethane ('plunging'). The plunging must be done as fast as possible so that the structure of the sample will not change.

In the project two methods of using freeze-fracture election microscopy have been used to investigate the structure of the liquid-crystal composites, freeze-fracture electron microscopy (FFEM) and freeze-fracture direct imaging (FFDI) [61]. In these two techniques the preparation of the grids is different. In FFEM the sample is rapidly frozen, fractured, shadowed with metal, and replicated with a thin carbon film, whilst in FFDI the sample is directly viewed after fracturing using a cryogenic holder (in which the grid is placed). The metal replica of the fractured surface, the morphology of which is controlled by the sample's micro structure, is then viewed with TEM. Initially the 'sandwich' is prepared see Fig. 3.8 for a schematic illustration. The two copperplates of 0.1mm thickness (BU 012056-T, Bal-Tec, Lichtenstein)) are first coated with a carbon layer as described in ref. [61]. Because of the nature of the sample, the surfaces of the copper plates and the grids used were made hydrophobic [63]. The copperplates and the grids (one bare grid and one holey carbon film grid) are assembled to form a sandwich, which is held with tweezers. After assembly the sandwich is placed in the sample, with the tweezers still holding it. Using the tweezers the sandwich can be opened and closed inside the sample.

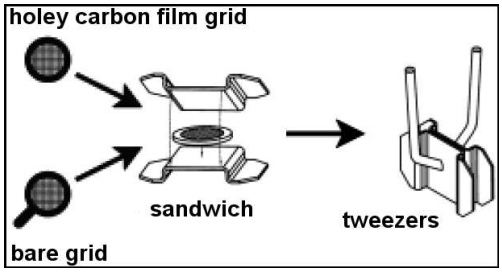

Figure 3.8: Schematic illustration of the 'sandwich', an assembly of two copper plates and two grids; one bare grid and one holey carbon film grid [61].

The transfer must be as fast as possible to avoid the formation of structures due to the freezing process. Liquid ethane is used rather than liquid nitrogen because it has the highest cooling rate of all cryogens [64]. After the freezing in liquid ethane the sandwich is transferred into liquid nitrogen. The sample is fractured under liquid nitrogen by pulling the grids away from each other using tweezers. After this step the holey carbon film grid can be used for FFDI, whilst the bare copper grid is treated further for before imaging for FFEM. The holey carbon film grid is mounted in a (precooled) cryo-holder and viewed in the TEM. The other (bare copper) grid, the complementary counterpart of the carbon grid, is 'shadowed'; with Pt/C and coated with a carbon layer. This grid

was placed inside a transfer box under liquid nitrogen, see Fig. 3.9.

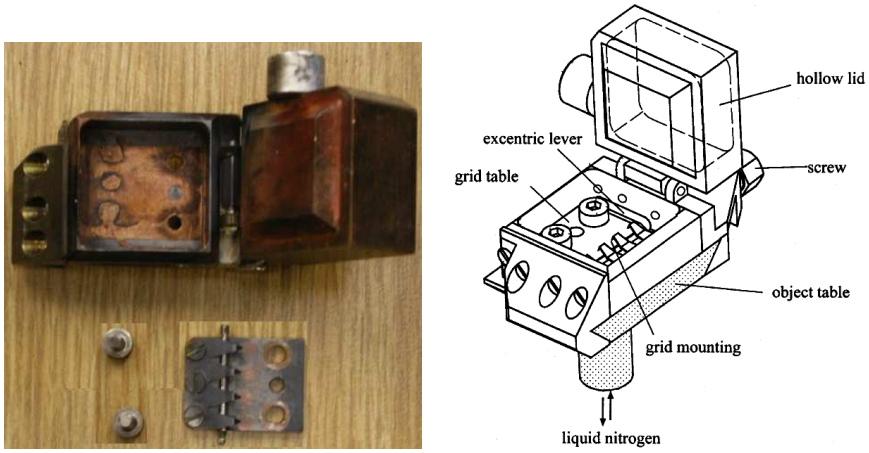

(a) (b)

Figure 3.9: Illustration of the liquid nitrogen filled transfer box. The lid of the box is hollow and filled with liquid nitrogen. This box is used to transfer the grid(s) to the freeze-fracture apparatus, with which the replication by shadowing with Pt/C is performed [65]. (a) Photograph of the transfer box used in the experimental procedure and (b) a schematic illustration indicating the various components in the box [65].

The transfer box is needed to transfer the grids under liquid nitrogen without temperature increase. The replication of the fracture surface by shadowing with Pt/C is done in the Balzers BAF 360 M freeze-fracture apparatus (Balzers, Lichtenstein). The box is placed in the apparatus which is then evacuated to a pressure of 4 x 10^{-5}Pa. During the evacuation the nitrogen solidifies and then evaporates very slowly (hours) whilst the temperature is kept at ∼-150^{o}C. After all nitrogen has evaporated the shadowing is performed, platinum is evaporated onto the surface under an angle of 45^o, as illustrated in Fig. 3.10(b). To stabilize the replica a thin carbon layer (ca. 200Å) is deposited by electron beam evaporation under a 90^o angle [66].

Freeze Fracture Direct Imaging: FFDI

For the preparation of FFDI experiments two different grids are used. One is a bare copper grid, the second one is a copper grid with a holey carbon film deposited on it (carbon is needed for conduction). The samples were brought to their desired temperature (20^{o}C or 50^{o}C), and the grids were held in the solution long enough to allow the solution to fully penetrate into the mesh of the copper grids. The grids are then frozen by dipping the grids into liquid ethane by plunging. For the plunging the 'plunging device' was used, with which an optimal transfer of the sample into the liquid ethane could be achieved [67]. Due to experimental constraints, the device could not be used for sample prepared at 50^{o}C.

Imaging was performed using a LEO 912 TEM operating at 120 kV, equipped

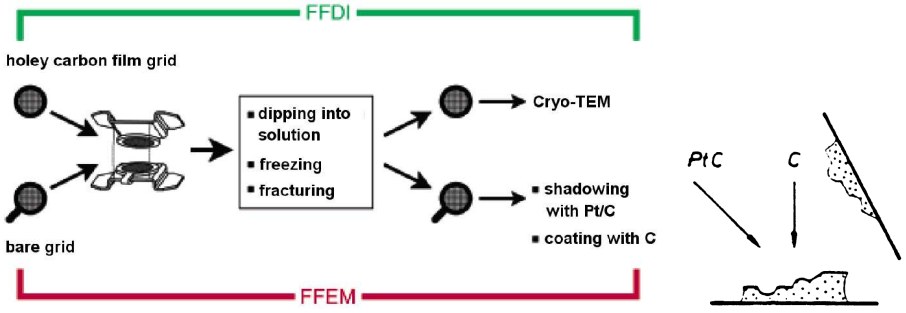

Figure 3.10: (a) In this schematic the different techniques are illustrated including their different steps in the process. Illustration is adapted from [61]. (b) Schematic illustration of shadowing, the platinum is deposited under a 45^o angle to create a shadow effect. After the shadowing a carbon film is deposited under a 90^o angle to stabilize the replica. Illustration is adapted from [66].

with a high-speed scanning camera (1024×1024 pixels, Procan Model TH 7896 M) under remote control from an imaging acquisition system (EsiVision^{TM} AnalySIS 2.11, Münster, Germany).

Freeze Fracture Electron Microscopy: FFEM

For FFEM the sample was initially prepared in the same way as for FFDI. The grids were plunged into liquid ethane. When frozen, the two copper grids are separated under liquid nitrogen using tweezers. The grids used for FFEM are mounted on a holder which will be inserted into the device in which the shadowing procedure will be carried out (∼-150^{o}C). In this procedure a platinum and carbon film are deposited on the sample (Fig. 3.10(b)). The platinum is deposited under an angle of 45^{o}C and the carbon from the top at an angle of 90^{o}C. Because the platinum is deposited under an angle of 45^{o}C there is the shadowing effect, which highlights the features of the samples when investigated. After the shadowing the grids are taken out of the device and the sample is washed away (using ethyl acetate), so only the platinum/carbon (Pt/C) film remains on the grid. Several pictures were taken from different positions on each grid. In the preparation of the samples the freezing is a critical step. The aim is to freeze the sample in its exact arrangement it is in whilst at room temperature (or other experimental temperature). For this the freezing must be instant to prevent molecular rearrangements whilst freezing. A specimen which is not frozen optimally can show different structures when imaged, which may be misleading.

3.3 Photon Correlation Spectroscopy

The scattering of light by a specimen reveals information about its structure, and when studied as a function of time its dynamics [68]. Dynamic light scattering is used in the

project to determine the sizes of the reverse micelles dispersed in dodecane.

Most composite materials are made up of constituents with very different refractive indices, which means that they are opaque. The liquid crystal 5CB - aerosil composite material fits this picture. It is not possible to use scattering techniques to study opaque systems using visible light, due to multiple scattering in it. Using x-rays to probe the system rather than visible light solves the problem of multiple scattering, because the sample is transparent to x-rays. For studying the behaviour of particles arranged in a nematic liquid small length scales need to be probed, which means light with a very short wavelength is needed: x-rays (∼1nm wavelength).

3.3.1 Light-scattering principles

In a scattering experiment, light (or x-rays) incident on a small volume of the sample is scattered from the direction of the incoming beam. The scattering can then be observed at a large distance from the sample, for example as a function of the scattering angle. Light used for these experiments needs to be coherent (i.e. monochromatic and in phase), which makes that the emerging wavefronts will interfere and create a 'speckle' pattern. The amplitude of the scattered wave (for coherent scattering) at a given time depends on the interference between the waves scattered by the different scattering objects in the scattering medium (sample). The scattered waves are coherent, which means that the amplitudes are added, and the light intensity is given by the absolute square of the resulting amplitude [69]. Before incidence the light travels in direction $\vec{k}_i$, and after scattering in direction $\vec{k}_s$. The scattering vector q is defined as the difference between the incident and scattered waves [70]

$$\vec{q} = \vec{k}_s - \vec{k}_i \quad \text{with} \quad q \equiv |\vec{q}| = \frac{4\pi}{\lambda} sin\theta. \tag{3.1}$$

Via Bragg's Law of diffraction $\lambda/n = 2dsin\theta$ the following relation relating the scattering vector and the length scale probed is expressed as

$$d = \frac{2\pi}{q}, \tag{3.2}$$

where d can be viewed as the length scale probed by the scattering vector q. In the schematic in Fig. 3.11 is illustrated how the incident radiation is scattered.

The scattered waves have the same amplitude, but differ in phase φ. The phase φ is $2\pi/\lambda$ (wavenumber) times the path length difference. In this example the path difference between a point P, specified by the vector l, and the origin O is then $-\vec{l}(\vec{k}_s - \vec{k}_i)$, which means that the phase difference is $\varphi = -(2\pi/\lambda)l(\vec{k}_s - \vec{k}_i)$. The speckle pattern, resulting from the interference of the scattered waves, is produced,

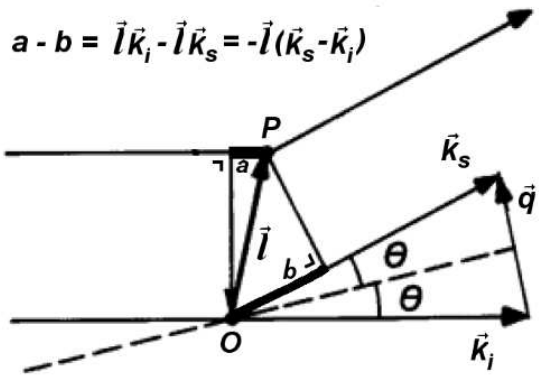

Figure 3.11: Schematic scattering process. The incident radiation $\vec{k}_i$ is scattered, after which the light propagates in the direction characterized by the vector $\vec{k}_s$. An important quantity in scattering experiments is the scattering vector $\vec{q} = \vec{k}_s - \vec{k}_i$, and $q \equiv |\vec{q}| = \frac{4\pi}{\lambda} sin\theta$ [70]. The path-length difference is given by the length difference between the two paths a and b: $a - b = \vec{l}\vec{k_i} - \vec{l}\vec{k_s} = -\vec{l}(\vec{k}_s - \vec{k}_i)$. Schematic adapted from [69].

and depends on the shape of the individual scatterers (aerosil particles or micelles) and their arrangement in the sample (e.g. network or clusters). The intensity of the speckles varies with the scattering vector $\vec{q}$, which in turn is determined by the scattering of the incident beam by the scattering object [71]

$$I(q) \propto F(q)S(q). \tag{3.3}$$

Here $F(q)$ is the form factor, describing the individual particles' shape, and $S(q)$ is the structure factor, which describes the particles' arrangement in the sample. When there is a low concentration of particles in the solvent, there are no interparticle correlations and $S(q) = 1$, but there is still diffusion. For concentrated systems, when the correlations between particles play a role, the structure factor is no longer 1 and shows pronounced features, including a peak $S(q_{max})$ which is related to the mean interparticle spacing via $2\pi/q_{max}$ [71]. In Fig. 3.12 the contributions of the structure factor $S(q)$ and the form factor $F(q)$ to the wavevector dependent intensity $I(q)$ is illustrated. For large q the strongest contribution to the measured intensity as function of q is the form factor $F(q)$.

3.3.2 Dynamic light scattering

In a scattering experiment the scattered light coming from the particles in the sample will interfere and create a 'speckle' pattern, that can be visualized on a detector. Because the particles move, the speckles will move as well so that the intensity fluctuates at a single point on the detector. Via analyzing the intensity fluctuations at each point

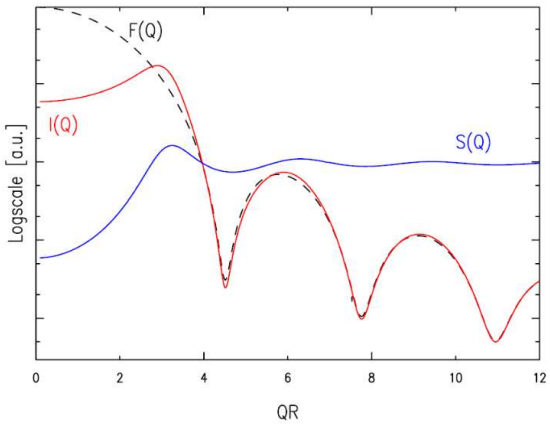

Figure 3.12: The red line indicates the scattered intensity of a dispersion of interacting spheres. It results from the product of the form factor $F(q)$ (dashed line) describing the scatterers' shape with the structure factor $S(q)$ (blue line) describing the interparticle interaction. The intensity is plotted against the product of the wavevector q and particle radius r. Schematic adapted from [71].

in the speckle pattern, it is possible to study the motion of the particles. This technique is called photon correlation spectroscopy or dynamic light scattering. When x-rays are used, the technique is called **x-ray photon correlation spectroscopy** (XPCS) [72].

The speckle pattern can be recorded with a CCD camera, so that each pixel can be analyzed over time. The intensity at a single pixel fluctuates over time as illustrated in Fig. 3.13(a). The fluctuations at a single pixels can be correlated to itself to find

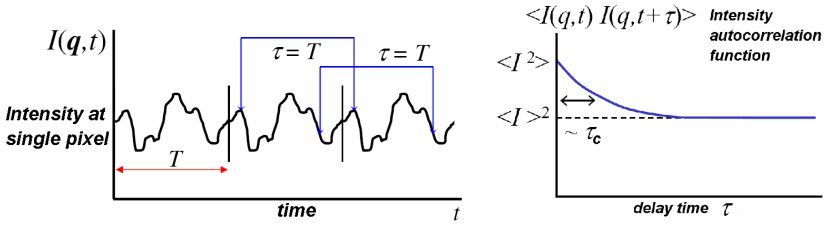

(a) (b)

Figure 3.13: (a) The intensity fluctuates over time at a single pixel. (b) The intensity correlation. For long delay times the system is no longer correlated, which means that any correlations are due to random fluctuations. τ_c indicates the characteristic time after which fluctuations become uncorrelated.

information about the motion of the sample; how much does the signal at the pixel change after a certain chosen delay time τ? The correlation indicates if there is a dependency as a function of time, and it can be found when the values of the fluctuations become uncorrelated, see Fig. 3.13(b). In Fig. 3.13(a) it is illustrated how this is done, at each point in time it is considered how much the signal resembles itself after the chosen delay time τ. The way the intensity decorrelates with itself over time gives information about the sample dynamics (fast or slow). This analysis can be done by

calculating the normalized intensity correlation function from the observed intensity at the pixel [73]:

$$g_2(q,\tau) = \frac{\langle I(q,0)I(q,\tau)\rangle}{\langle I(q)\rangle^2} \tag{3.4}$$

Here $\langle ...\rangle$ indicates a time average, $I(q)$ is the measured intensity at time t. In photon correlation spectroscopy the intensity correlation function is an important concept. In Fig. 3.14 an example of a measured intensity correlation function is shown. The initial

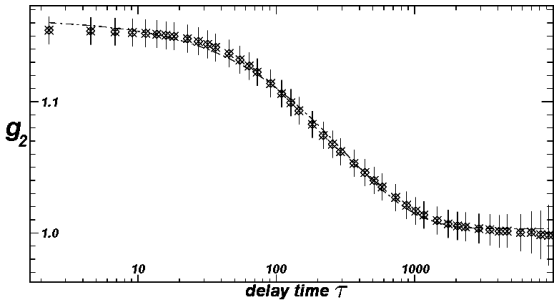

Figure 3.14: Example from the data obtained in the project. From the data the characteristic relaxation time τ_s of the sample can be found. In the graph this is the location after the plateau where the curve falls off.

plateau is followed by a decay at a certain delay time τ after which the curve levels off at a value $g_2 = 1$. Via fitting the measured curves the characteristic relaxation time τ_s of the sample can be found, which determines where the curve falls off indicating how long it takes before the intensity fluctuations decorrelate. The relaxation of g_2 can be described by a power law ($(t/\tau)^{\mu}$) [74], which is shown in the figure using the dash-dotted line. The characteristic time τ_s increases with sample age as t^{μ}, where μ describes the slope of the curve. The intensity correlation function can be fitted with a function $f(q,t)$ that describes exponential decay:

$$f(q,t) = BL + b \cdot e^{-2(\frac{t}{\tau_c})^{\mu}}, \tag{3.5}$$

where BL indicates the value to which the curve decays, and b determines the contrast between the initial and final level of the curve. τ_c indicates the characteristic decay time which determines where the curve falls of indicating how long it takes before the intensity fluctuations decorrelate. μ adjusts the slope of the exponential curve, which gives an indication of *how* the system relaxes. Values of μ than 1.0 implies a faster decay than a normal exponential (compressed exponential), and a value smaller than 1.0 indicates decay that is slower than exponential decay (stretched exponential).

When studying an equilibrium system, the correlation function is only dependent on the time difference between measurements, and not on the history of the sample. The

correlation functions measured can be referred to as one-time correlation functions [75]. However, when one studies a non-equilibrium system, the intensity correlations are dependent on the history of the sample, the correlation function is dependent both on the time difference between measurements as well as on when the first measurement is done. The fluctuations measured can be quantified by means of the two-time correlation function.

Two-time correlation function The two-time correlation functions is represented as [75]

$$G_2(\vec{q}, t_1, t_2) = \frac{\langle I(\vec{q}, t_1) I(\vec{q}, t_2) \rangle}{\langle I(\vec{q}, t_1) \rangle \langle I(\vec{q}, t_2) \rangle} \tag{3.6}$$

for one value of q. The variables used to describe the two-time correlation function are the average time or age $t_a (= (t_1 + t_2)/2)$ and the time difference $\Delta t = |t_1 - t_2|$ [76]. Here t_a is the distance measured along the $t_1 = t_2$ diagonal. and $|t_1 - t_2|$ is the distance from the $t_1 = t_2$ diagonal in the perpendicular direction. In Fig. 3.15 an example from literature (left [75]) and the results obtained in the project (right) are presented. When

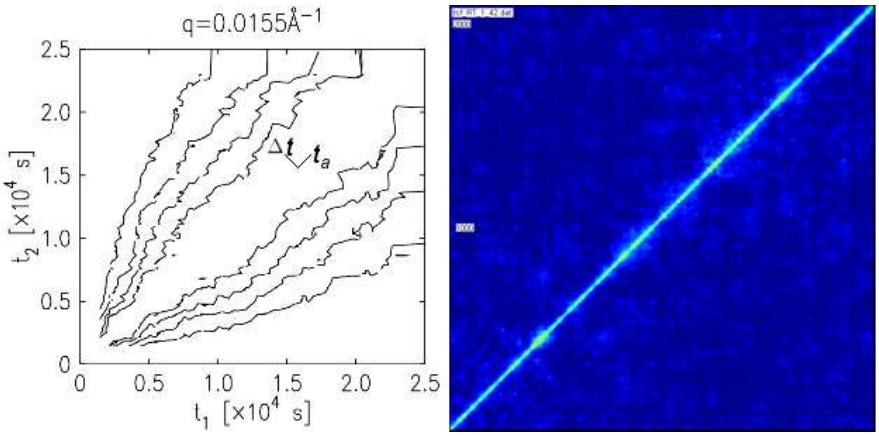

Figure 3.15: Contour plot examples of 2t cf. The age of the sample is $t_a (= (t_1 + t_2)/2)$, which is the diagonal of the plot, and $\Delta t = |t_1 - t_2|$ is the correlation time, which is the distance from the diagonal in the perpendicular direction. Both variables are indicated in the plot on the left [75].

the system is in equilibrium, then the two-time correlation function only depends on $|t_1 - t_2|$ and not on age, which is true for the plot on the right shown in Fig. 3.15. Here the color contours are parallel to the diagonal ($t_1 = t_2$) of the plot, which means the signal is not dependent on when the measurement is started (thus the age of the sample). In the plot on the left (adapted from ref. [75]) it can be seen that the signal varies with age, it is important when the first measurement was made. g_2 can be obtained from G_2 by averaging G_2 over time.

Time resolved correlation In the project we are interested in studying the dynamics of soft matter over time (aging), in this case of 5CB-aerosil composite.

Information about the dynamics over time can be studied by examining the evolution of the correlation function (eq. (3.4)) over time. For this, the degree of correlation, $c_I(t_w, \tau)$, between speckle images recorded at a lag time τ is then measured as a function of the time t_w at which the first image was taken. $c_I(t_w, \tau)$ is calculated for a set of fixed delay times τ at a fixed wavevector q.

$$c_I(t_w, \tau) = \frac{< I_p(t_w) I_p(t_w + \tau) >_p}{< I_p(t_w) >_p < I_p(t_w + \tau) >_p} \tag{3.7}$$

I_p denotes the intensity at pixel p, τ is the delay time between the two images, and $\langle ... \rangle_p$ denotes averaging over all pixels of the selected area of the CCD image.

$c_I(t_w, \tau)$ is different from the normalized intensity correlation function $g_2 - 1$, since the averaging is over pixels rather than over time. In Fig. 3.16 it is illustrated what information can be obtained from $c_I(t_w, \tau)$. In Fig. 3.16(a) $c_I(t_w, \tau)$ shows a

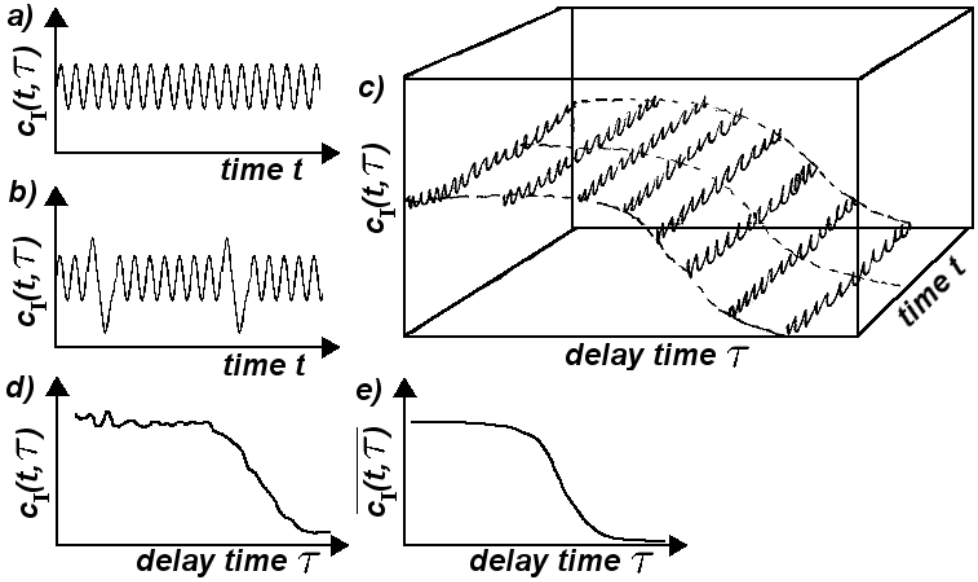

Figure 3.16: Time resolved correlation function. (a) Example of $c_I(t_w, \tau)$ that shows a homogeneous signal at a fixed τ, and (b) a heterogeneous signal at fixed τ. (c) Illustration of how $c_I(t_w, \tau)$ behaves with time (age) and delay time τ. (d) The calculated $c_I(t_w, \tau)$ for a single frame (thus a fixed t), and (e) $c_I(t, \tau)$ averaged over time, which is equivalent to $g_2 - 1$.

homogeneous signal at fixed τ. This is the behaviour that will be observed when studying a system with homogeneous dynamics like for example a colloidal suspension where the particles move with Brownian motion and slowly diffuse through the system. When the system has heterogeneous dynamics (Fig. 3.16(b)) the $c_I(t_w, \tau)$ signal obtained is heterogeneous, spikes in the signal indicate that there is a slowing down in the system's dynamics, whilst dips indicate a speeding up. When $c_I(t_w, \tau)$ is calculated for a series of delay times τ the graph in Fig. 3.16(c) is obtained, the dynamics at

various delay times τ can be studied as a function of time. In Fig. 3.16(d) the spatial correlation at a chosen time t (single frame) is shown as function of delay time τ, so that it can be learned after which characteristic time τ_c the system loses its correlation. When $c_I(t_w, \tau)$ is averaged over a range of chosen times a graph as illustrated in Fig. 3.16(e) is obtained, which is equivalent to $g_2 - 1$ (eq. (3.4)).

$$g_2(t, \tau) - 1 = \langle c_I(t, \tau) \rangle \tag{3.8}$$

Where $\langle ... \rangle$ indicates averaging over time. When one examines $c_I(t_w, \tau)$ it is possible to see changes with time easily and the dynamics exhibited by the system can be distinguished between homogeneous and heterogeneous.

3.4 XPCS Instrumentation

For obtaining optimum quality in the speckle pattern a coherent light source is needed. In DLS coherent coherence is achieved via using a laser. Upon excitation by the pump source the laser medium, which is located in the optical cavity, exhibits spontaneous and stimulated emission of photons of a specified wavelength determined by the size of the optical cavity. It is difficult to achieve coherence with x-rays, because filtering in wavelength and phase to make the beam coherent reduces its intensity. In experiments, partial coherence combined with 'high enough' radiation x-ray beams can be sufficient to obtain good speckle patterns. This can be achieved in third generation synchrotrons, such as the ESRF in Grenoble, France.

The underlying principle in creating x-rays is that any accelerating charge must radiate electromagnetic energy; when electrons are accelerated to high velocities they will radiate high energy radiation, the x-rays. The electrons are first accelerated at a few points in the ring using magnets, and to keep the electrons accelerating the strengths of the magnets are increased as the electrons gain energy. When the electrons have reached 'high enough' velocities they are ejected out of the ring into an undulator, Fig. 3.17. An undulator consists of a periodic magnetic structure producing a sinusoidal magnetic field along the electron path. The undulator produces x-rays with a wavelength that is set by the undulator gap. The emitted x-rays needs to be both spatially and longitudinally coherent. Coherence describes how close the superposition of two (or more) waves resembles a single wave. If all x-rays have the same wavelength and phase they are longitudinally coherent (temporally), and if they are in phase across the beam they are spatially coherent (transversely), see Fig. 3.18. To achieve optimal coherence the x-rays coming out the undulator require further filtering, because there is still spread in wavelength. The more filtering is applied, the smaller the fraction

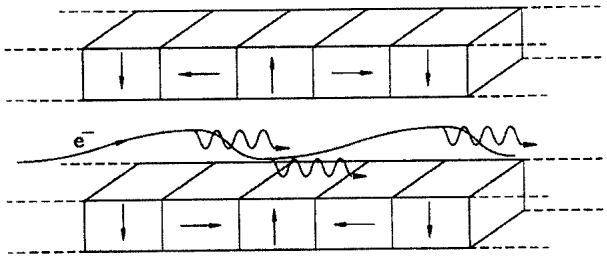

Figure 3.17: The electrons enter the undulator, in which the magnetic field alternates from downwards to upwards. When the electrons travel through they oscillate (sideways) which causes them to radiate x-rays in the direction of the undulator's axis (towards the right in this image). From [77].

of the remaining x-rays (thus a decrease in the brilliance). The produced x-rays or of a quality resulting from a compromise between achieving optimal coherence versus optimal brilliance. Partial coherent x-rays with high enough brilliance are sufficient to obtain speckle patterns of samples.

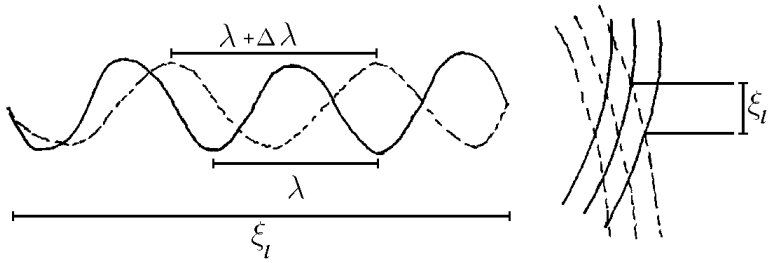

Figure 3.18: Coherence. Left: The longitudinal coherence length is the length over which the light is not more than π out of phase. Right: The transverse coherence length is the distance over which the phases of the different light waves do not differ by more than π.

The temporal coherence of the x-ray beam is described by the longitudinal coherence length ς_l, which is the distance over which the beam can be assumed to be monochromatic: $\varsigma_l = \frac{\lambda}{2}\frac{\lambda}{\Delta\lambda}$, where $\frac{\lambda}{\Delta\lambda}$ is the monochromaticity of the beam. For the Troïka beamline at the ESRF this is 10^{-4} for the Si(111) monochromator used [78].

The spatial coherence length ς_s depends on the wavelength λ and the angular source size $\Delta\Theta = \frac{r_p}{x}$, (where r_p is the pinhole size and x the distance between the pinhole and the sample) and is given by: $\varsigma_s = \frac{1}{2}\frac{\lambda}{\Delta\Theta} = \frac{\lambda}{2}\frac{x}{r_p}$. At the Troïka III beamline (ID10A) at the ESRF in Grenoble we used $\lambda = 1.5$ Å , x = 46m, and a pinhole size of 20x20μm, which means that ς_s is 0.37μm.

For optimal results in the XPCS experiments the sample needs to be illuminated coherently, which means that the maximum path length difference (PLD) for the x-rays passing through the sample must be smaller than or equal to ς_l, and that the lateral illumination width (LIW) must be smaller than or equal to ς_s. The PLD can be approximated by PLD $= 2Tsin^2(\theta) + LIWsin(2\theta)$, where θ is the scattering angle, and

T the sample thickness [79]. The diameter of the capillaries used in the experiments is 1.5mm, and the pinhole is chosen such that LIW = 10μm. The PLD for the largest q wavevectors used in the experiments is only about 30nm. In the set-up used here the ς_l and ς_s are 345μm and 0.37μm respectively. This means that the PLD lies well below the required ς_l = 0.37μm indicating that the sample is coherently illuminated under the experimental conditions. The LIW however is wider than ς_s which means that the speckle contract is not optimal in the experiments. The angular speckle size can be determined via [79]

$$D_s = [(\frac{\lambda}{LIW})^2 + \Delta\Theta^2]^{\frac{1}{2}} \tag{3.9}$$

where $\Delta\Theta$ is the angular source size. With a sample-detector distance of 233cm this leads to an actual speckle size on the detector of 35μm which is larger than the detector pixel size of 20μx20μm. This means that there is maximal one speckle per pixel.

3.4.1 Experimental procedure

The experimental XPCS set-up used in the experiments is located at the ESRF, Grenoble in France on the Troïka I beamline (ID10A). At the beamline we worked with Yuriy Chushkin who aligned the set up to yield optimal speckle contrast for studying the aerosil composite samples. The selected x-ray energy used was 7.979 keV using a pinhole size of 20μx20μm, and the photon count was 10^{10} photons per second (wavelength of $\lambda = 1.555\mathring{A}$). The distance between the source and detector R = 46m. After mounting the sample, both the beam and sample position need to be optimized, as well as the position of various shields (for reducing light intensity in case of over-exposure). After adjusting the various components the exposure time needs to be determined and the XPCS experiment can begin. A series of dark images needs to be recorded to establish the background activity of the camera. To be able to analyze the data afterwards the location of the beam center is recorded. See Fig. 3.19 for a schematic layout of the beamline.

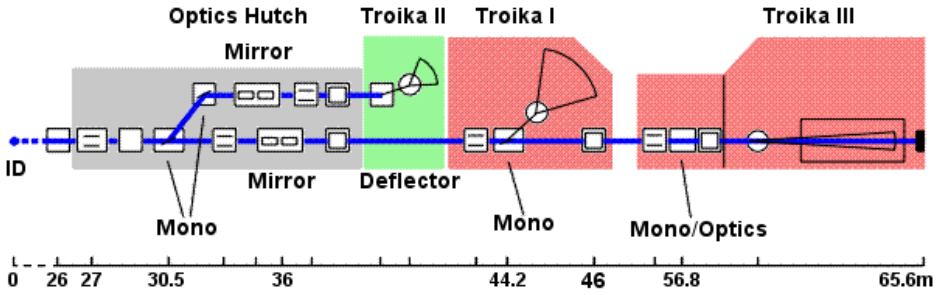

Figure 3.19: Schematic layout of the beamline. The data taken in the experiments is collected at Troïka I [78].

3.4.2 Noise in XPCS data

The intensity measured at the pixels of the CCD camera is proportional to the number of photons arriving at the pixel. The fluctuations in intensity are not only due to the motion of the scatterers but there are also sources of noise contributing to the measured signal. XPCS measurements have signal-to-noise ratios that can be characterized experimentally [80]. Errorbars can be calculated from the statistical variation of the results for $g_2(q,t)$. The beam intensity varies because of the focus, the focus point has a Gaussian shape [81]. This has to do with the transverse and longitudinal coherence length, and the distance from the source to the sample, which have an effect on the optical contrast [80, 81]. In calculating the errorbars for the data in our experiments Jakemans' expression has been used:

$$varg_2 = \frac{g_2}{M\overline{n}^2}. \tag{3.10}$$

Here M is the number of correlated pairs (time steps) averaged to yield g_2 and $\overline{n}$ is the mean number of counts detected per accumulation time (exposure time of CCD camera). This can be rewritten in terms of count rate ($\overline{I}$) per CCD pixel, the accumulation time τ, the number of pixels ($n_x n_y$) and the total experimental duration (T) as

$$varg_2 = g_2/(n_x n_y \cdot T \cdot \tau \cdot \overline{I}^2). \tag{3.11}$$

Experimental sources of noise are fluctuations in the beam intensity, beam coherence and variation in the number of scatterers. The intensity of the incoming beam varies in time, it can drop by up to 30 % over a time interval of 5 hours, and there are beam fluctuations on a short time scale varying from frame to frame. Prior to analyzing the data the intensity needs to be normalized. Fluctuations in the beam coherence will give rise to the overlap of speckles, which leads to variations in the scattered intensity. This is due to the fact that an increasing number of coherence volumes (scattering centers in the probed volume) will lead to a decrease in the correlation function [82]. The partial coherence of the beam and the motion of the instrument and the beam eventually lead to decorrelation even for a perfect stationary sample. The fluctuations in beam coherence can be observed via measuring a static sample, for which in the experiments Vycor glass was used, a porous material made from a quaternary glass mixture. This material scatters relatively uniformly at a broad range of wavevectors. It was checked that the decorrelation occurs on a much longer time scale (∼2000 sec.) than the sample dynamics, see Ch. 7.

Due to rearrangements in the sample there can be a variation in the number of scatterers. This is probably not much the case in the system studied here, the liquid

crystal 5CB is rather viscous even in the isotropic state, which means that on the timescale of the experiments the silica particles or clusters of them remained roughly where they were at the start of the experiment, i.e. in the scattering volume. Large clusters occasionally were seen to perform sedimentation, which resulted in occasional strong scattering. This data was discarded before calculating correlation functions.

Background noise of the CCD camera is taken into account as well. A series of dark images is taken to establish the background activity of the camera.

In the fitting of the data errors need to be taken into account. Errors arise from the instrumentation and in the fitting itself. Also for smaller q the measured errors will be lager than those for larger q, as there are less pixels for smaller q. When calculating the correlation function errors at smaller delay times are smaller than for larger delay times. This is because, when we are calculating the CFs, the intensity at some time t_1 is compared with the intensity at a chosen time t_2. The larger $t_1 - t_2 = \delta t$ the less data points there are to be compared and thus the error will become larger.

The mean value μ of an observed quantity is defined as [83]:

$$\mu = \lim_{N\to\infty}(\frac{1}{N}\sum x_i) \tag{3.12}$$

in which N denotes the number of measurements and x_i the determined quantity of x. An important measure of the spread of the measurements about the mean is the standard deviation (σ), which tells you how much one measurements deviates from the mean μ. In the case of the XPCS measurements the average intensity is measured. Because the speckles are moving due to movement in the 5CB-aerosil sample the intensity per pixel fluctuates in time. The variance (which is the square of the standard deviation) is defined as [83]:

$$\sigma^2 = \lim_{N\to\infty}(\frac{1}{N}\sum(x_i-\mu)^2) = \lim_{N\to\infty}(\frac{1}{N}\sum x_i^2) - \mu^2 \tag{3.13}$$

Repeated measurements of the same quantity are expected to yield results which are clustered around a particular value. The different error contributions to the intensity are not known separately, even though the sources are known. Here we only measure the end result.

For determining how well the fitting of the data is performed the χ^2 parameter is calculated, which indicates how well the data is fitted. For one data point on the fitted graphs, thus for one delay time value, there are many different intensities measured. (For short delay times there are more data points). The intensity for a certain delay time value is normally distributed around its average for that point. The χ^2 describes

how the observed data deviate from the expected values for the data.

$$\chi^2 = \sum_{i=1}^{n} \frac{[O_i - E_i]^2}{\sigma^2} \tag{3.14}$$

The numerator in equation 3.14 is a measure of the observed spread in the measurements, and the denominator is the measure of the expected spread: the variance. The variance is determined from the data like given in equation (3.13). For a good agreement and thus a good fit, we expect that the expected spread and the measured spread correspond nicely to each other, which means that for each observation data point (here a certain delay time), a value of about one is expected for χ^2. For each data point this is true, so for all the data the value of χ^2 should correspond to the number of data points n: $\chi^2 \simeq n$.

3.5 Rheology

For characterizing the mechanical properties of materials rheology can be used. In rheology the response of a body matter to applied stress, force per unit area, is studied. The way a body is deformed under applied stress depends on the nature of the body, liquids and solid respond to shear very differently. Strain (dimensionless quantity) is the measure of deformation representing the relative displacement between particles in the body to which stress is applied. Strain defines the amount of stretch, compression (normal) or distortion (shear) upon applied stress $\gamma = \frac{\Delta x}{d}$, where Δx is the displacement of the top layer of the sample along the direction of shear and d the sample thickness, see Fig. 3.20. It can be seen that the shear is not homogeneous, parts of the sample at the

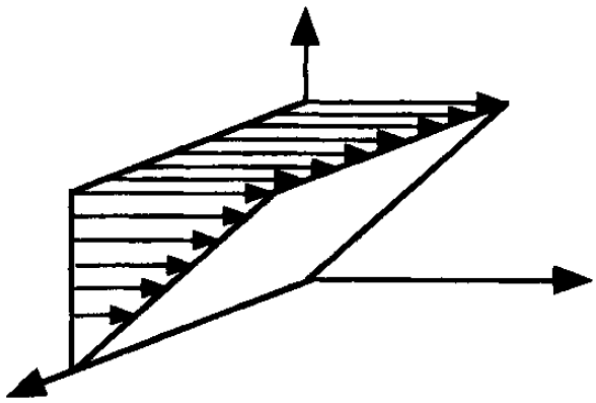

Figure 3.20: Velocity profile in steady shear flow. Figure adapted from [84].

top is sheared more than material at the bottom. The strain is proportional to the stress

applied as $\sigma = G\gamma$, where G is the shear modulus of the material. When the deformation of a system is proportional to the applied stress the material is called a linear elastic solids. When a fluid is deformed the behaviour is different, flow will be induced. When a Newtonian fluid (such as water) is studied the material flows in response to the shear as shown in Fig. 3.20. The top moves with a constant velocity while the bottom plate remains stationary. In the case of a Newtonian fluid it is assumed that the top layer of the sample moves with the same velocity v as the upper plate. Because only the upper plate moves and the bottom plate is stationary there exists a velocity gradient across the sample. The strain rate (or shear rate) is defined as $\frac{d\gamma}{dt} = \dot{\gamma} = \frac{d}{dt}(\frac{\Delta x}{d}) = \frac{v}{d}$. The stress is proportional to the shear rate $\frac{d}{dt}(\frac{\Delta x}{d})\eta = \dot{\gamma}\eta = \sigma$, where η is the viscosity of the liquid under stress. The viscosity is a measure of the resistance of a fluid to flow (shear forces). The strain rate behaves linearly the applied stress for Newtonian fluids, the fluid shows viscous behaviour. When this is not the case the fluid is called non-Newtonian. Fluids for which the apparent viscosity decreases with increasing shear rate are called shear-thinning fluids, and systems for which the viscosity increases with applied rate are called shear thickening fluids. For shear-thinning fluids shearing becomes easier when they are sheared faster, while for shear-thickening fluids more and more effort is needed to achieve larger shear rates. Many systems show characteristics found both in solids and liquids, they don't show purely elastic responses or viscous behaviour, but they respond in a manner as a combination of the two and are therefore called viscoelastic.

When constant stress is applied to for example a gel, rupture of structure can be induced, which will influence the measurement outcome. To eliminate the possibility of rupturing the material under study, an oscillatory technique can be used. In this method oscillatory stress is applied, from which the amplitude must be small enough to prevent the deformation of the sample in which rupture could easily occur. By applying oscillatory stress to the system and measuring the mechanical response can be measured. The mechanical response G^* can be decomposed into an elastic and a viscous contribution which generally depend on the used frequency ω at which the stress is applied

$$G^*(\omega) = G'(\omega) + iG''(\omega), \tag{3.15}$$

where G'(ω) is the elastic or storage modulus, representing the storage of elastic energy, and G"(ω) the viscous or loss modulus, representing the viscous dissipation of energy. In a measurement of G' and G" performed on a viscoelastic material often a crossover in the behaviour is observed, see fig. 3.21(a). For low frequencies G" is dominant indicating the behaviour is mostly solidlike rather than liquidlike. At a certain frequency the viscoelastic material makes a transition from solidlike

(elastic) to liquidlike (viscous) behaviour. The relevant time scale can be defined as a relaxation time of the material [85]. The frequency at which the crossover takes place is approximately equal to the inverse of the fluid's characteristic relaxation time τ. This characteristic relaxation time is roughly the longest time needed for the elastic structures in the fluid to relax. For frequencies higher than this frequency at which the transition takes place the behaviour is mostly liquidlike.

In the experiments the cone-plate geometry is used, see Fig. 3.21(b). In this geometry uniform shear flows can be applied, the shear rate $\dot{\gamma}$ is constant throughout the gap and thus also the shear stress [86]. In the measurements first the response of

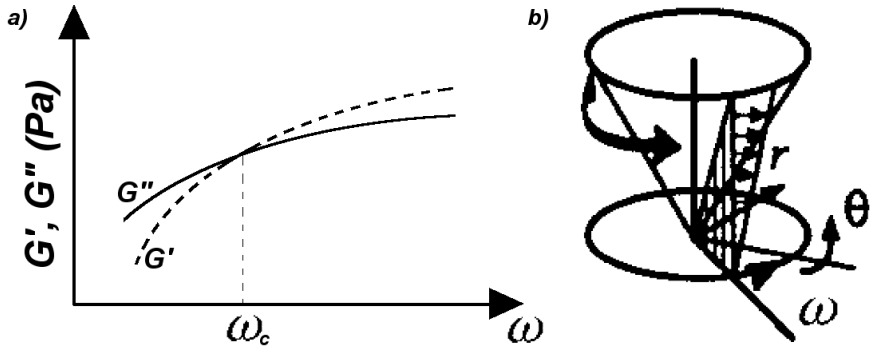

Figure 3.21: (a) Schematic of the storage and loss moduli as a function of frequency of a typical viscoelastic material. At the characteristic frequency ω_c the behaviour changes from 'liquidlike' to 'solidlike'. (b)Schematic illustration of the cone-plate geometry. r is the radius of the cone, θ is the cone angle, and ω denotes the angular velocity (rad.s^{-1}). Figure adapted from [84].

the samples were studied as a function of oscillatory stress to investigate the regime over which the material responds elastically to the applied stress via $\sigma = G^*\gamma$. The frequency measurements were then performed at a chosen constant stress at which the material shows elastic response. Finally steady state flow measurements were carried out. In the steady state flow measurement the material is subjected to continuous shearing at different shear rates. The stress is measured as function of shear rate. For every shear rate applied, time is needed for the material to equilibrate. The equilibrium conditions in the experiments were set so that equilibrium is attained when 4 subsequent measurement values are within 2% from each other (the maximum time per measurement point is set to 5 minutes).

Newtonian fluids give a straight line with a zero intercept, $\sigma = \dot{\gamma}\eta$. Fluids that do not exhibit this behaviour are called non-Newtonian [86]. The Herschel-Bulkley model is a general relationship to describe the behaviour of non-Newtonian fluids: $\sigma = K(\dot{\gamma})^n + \sigma_0$, where K is the consistency, n is the flow behaviour index, and σ_0 is the yield stress. The yield stress is the applied stress that must be exceeded to make the material flow, so that it will not relax to its original configuration. When $n = 1$ the

behaviour is referred to as Bingham plastic behaviour, the fluid gives a straight line in σ vs $\dot{\gamma}$ but exhibits a yield stress. For $n \neq 1$ the system shows power law behaviour, for $0<n<1$ the fluid is shear-thinning and for $1<n<\infty$ the fluid is shear-thickening. In the following graph the flow curves for fluids with different characteristics are summarized, Fig. 3.22.

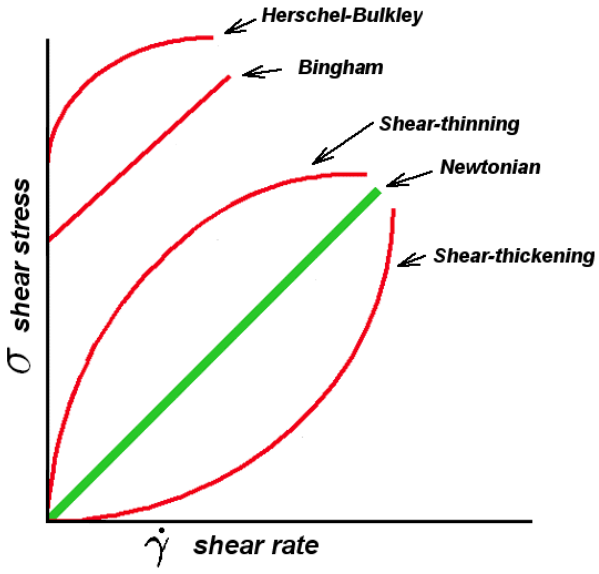

Figure 3.22: Flow curves for fluids with different characteristics.

The measurements were carried out on the Advanced Rheometer AR2000 apparatus from TA Instruments. For the measurements were carried out with a 4cm 2^o cone with a gap (or truncation) of 49μm. At the start of the measurement the zero-point needs to be set, so that the cone can be placed at the correct truncation gap. For this the cone was lowered very slowly by the apparatus whilst measuring the normal force. When the cone comes into contact with the Peltier plate the normal force increases and the cone is stopped from lowering when the normal force reaches 2mN. This point is set as the zero-point and the cone was raised so that the sample could be loaded after which the cone was slowly lowered so that the truncation gap was 49μm.

Chapter 4

Particles in a phase-separating microemulsion: early stage

The behaviour of sterically-stabilized poly(methyl methacrylate) (PMMA) colloids dispersed in a phase-separating microemulsion is studied as a function of solvent composition and colloid volume fraction using microscopy techniques. This is the first time that pre-transitional aggregation has been studied for particles that are not charge stabilized.

4.1 Introduction

Insertion of colloids into binary-liquid mixtures is the subject of intensive study, experimentally as well as theoretically and computationally [17,18,28,29,32,33,87–110]. Here we employ a microemulsion containing reverse micelles [26] for which many characteristics have been investigated, e.g. thermal conductivity and diffusivity near the critical end point [28], electrical conductivity near the critical point [108], dielectric relaxation [18], refractive index and density near the critical end point [29, 33]. In a certain composition range the microemulsion is found to behave in a manner analogous to binary-liquid mixtures [32], which is the range used for the work described in this thesis. The microemulsion system (lower consolute point) exhibits phase separation upon increasing temperature into two microemulsions with different micelle concentrations, in this thesis referred to as the micellar 'gas' phase and micellar 'liquid' phase, which respectively contain a low and high concentration of micelles [17]. Due to the presence of micelles and the composition used, the system is intrinsically slow which means that phase separation can be imaged in real time using microscopy techniques. During phase separation the colloids partition into the preferred microemulsion via a mechanism that depends on the exact composition of the microemulsion.

The effect of the presence of surfactant molecules in a solution proves to be important for the stability of the PMMA colloids [111, 112]. The behaviour of PMMA colloids (PHSA grafted) in dodecane with reverse AOT micelles was investigated by Hsu et al. [111]. When the AOT concentration exceeds the critical micelle concentration

(cmc) it was found that the PMMA colloids become charge stabilized, because the reverse micelles lower the energetic cost of ionization by being able to accept charges. This makes the electrostatic interactions between the PMMA colloids surprisingly strong. In a more recent study performed by Roberts et al. a more broad investigation was performed [112]. PHSA-grafted PMMA colloids with various radii were studied in decane and dodecane in the presence of reverse micelles consisting of different types of amphiphiles (neutral, and positively or negatively charged). The sign of the charge obtained by the particle was found to depend on the chemical nature of the reverse micellar system. The magnitude of the colloid's surface potential was found to be independent of both the micelle concentration and the colloidal radius, which suggests that a common charging mechanism is responsible in this type of system containing reverse micelles.

The phase behaviour of charged polystyrene particles dispersed in a solution of wormlike micelles formed in brine is investigated [113]. The wormlike micelles are able to break and reform, which makes it an interesting depletant. The depletion mechanism plays an important role in phase separation in the system.

When colloids are dispersed in a partially-miscible binary-liquid mixture they are likely to have a stronger affinity for one of the liquids than for the other. As a result, prior to and during phase separation the liquid for which the colloids have stronger affinity might adsorb onto or 'wet' the colloidal surface. The wetting effect is likely to be more pronounced when the mixture is poorer in the liquid component for which the colloids have stronger affinity, i.e. the case in which the host solvent has an off-critical composition. The critical regime, where fluctuations can be important, will be introduced first, followed by introduction to the off-critical regime.

Critical Colloids dispersed in critical binary mixtures are being studied intensively because of the possible effective interactions between inserted colloids. Critical liquid mixtures phase separate via spinodal decomposition, during which process components diffuse throughout the mixture into different regions. When a solvent is undergoing a critical phase transition, enhanced solvent fluctuations are present in the mixture. If there are for example colloids present in the system, these critical fluctuations can induce an effective attraction between colloids, which is termed the critical Casimir force [91]. In recent experiments performed by Hertlein et al. critical Casimir forces between a surface and a colloid were measured in real-time for the first time [89]. More recently in the same group researchers have been able to use critical Casimir forces as an approach for colloidal assembly on chemically patterned surfaces [114]. The system consists of charge-stabilized polystyrene colloids in a binary-liquid mixture of water and 2,6-lutidine. The forces measured at criticality were larger than those found off-critical. At criticality there was a gradual increase of the force as the temperature

approached to the critical temperature where the fluctuations are largest. In an off-critical composition there was hardly a change in the potential measured, up until some point when there is an abrupt change: a narrow and steep potential well developed close to the surface. Here the colloid moves closer to the surface, which is interpreted as the formation of a liquid bridge that spans the gap between the colloid and the surface.

By contrast, in calculations performed by Schlesener et al., it was found that the critical Casimir force are strongest in the region of the phase diagram where the binary-liquid mixture is poor in the component preferred by the colloids [90]. Measurements of the second virial coefficient, using the same system as Hertlein et al. (charge-stabilized polystyrene colloids in water and 2,6-lutidine) [89], done by Kurnaz and Maher [88] confirm Schlesener's results. The second virial coefficient B_2 is a measure of the interaction potential between colloids. They find that B_2 shows similar behaviour in the critical regime and the off-critical regime in which the binary mixture is poor in the preferred component (aggregation regime), although B_2 has a smaller magnitude in the critical regime than in the aggregation regime. In measurements on the non-aggregation side of the phase diagram it was found that B_2 indicates hardly any interaction or a slightly attractive interaction. Aggregation was never observed in their critical samples [88]. Gallagher and Maher made a systematic survey of the behaviour of polystyrene colloids of differing size and surface-charge density in critical mixtures of water and 2,6-lutidine [109]. Upon approaching the demixing line the colloids partition into the preferred phase without noticeably altering the rate of phase separation. No aggregation at critical composition is observed here, partially due to the very low volume fraction of particles used. The absence of aggregation is reported in other studies too [87, 88, 110].

Off-critical Experiments on off-critical systems have received wide attention because of their possible connections to the broader body of wetting phenomena [93, 101, 105, 107]. The most remarkable result is the observation of a reversible aggregation of the colloidal particles in the liquid mixture's one-phase region but near the two-phase boundary, see Fig. 4.1. The reversible aggregation phenomenon is thought to be universal, as this is observed in many off-critical binary-liquid mixtures and different charge-stabilized colloids [87, 93, 105, 106], and certain characteristics are observed in this type of system, for example that the rate of colloidal aggregation is diffusion limited [104], that the aggregation is reversible with temperature [103, 115] and that the preferred liquid phase can be varied by changing the particles' surface [87] or by addition of salt to the solvent [102]. Experiments performed with a high colloid concentration revealed the existence of a glass transition both on cooling and heating [116].

Observations of colloids in binary-liquids were made by Beysens and Estéve and

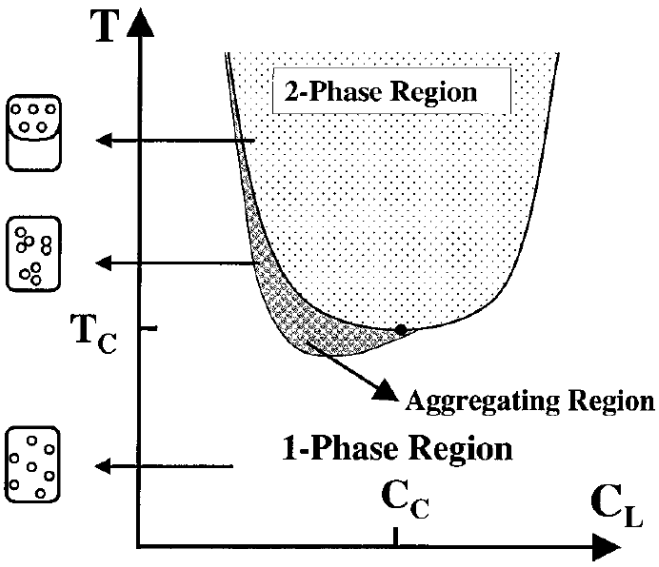

Figure 4.1: Schematic phase diagram of water and 2,6-lutidine containing silica colloids, where C_L denotes the 2,6-lutidine weight fraction. The aggregation region lies on the water rich branch, the liquid component least preferred by the colloids. The schematic is adapted from Ref. [105].

it was found that the colloids preferentially seem to adsorb one of the two liquids [101]. Later Beysens et al. explained the matter in terms of the adsorption of the preferred component (prewetting) modifying the colloids' stability which causes them to aggregate reversibly [93, 99, 100]. The existence of a thin prewetting layer on the colloidal clusters prior to phase separation is not agreed on experimentally, with some authors showing some evidence on the existence of such a layer using interferometry methods for determining refractive index variations of liquids (silica particles in water-lutidine) [98] whereas others claim they could not find evidence of the existence of a prewetting layer using dynamic light scattering techniques (polystyrene particles in water-lutidine) [87]. According to Beysens et al. the phase-coexistence curve is not altered significantly due to addition of colloids to the binary-liquid mixture and the findings are interpreted as being a 'pseudo binary' phase transition.

Kaler et al. interpret their results from a different perspective and explain that the system should be viewed as ternary, as they find that the addition of colloids does profoundly modify the binary-liquid system [94]. In one study the authors conclude that the intercolloid interactions can be tuned by changing the solvent composition, and a colloidal gas-liquid phase transition can be induced [97]. Additionally, they find that the colloids form aggregates with a crystalline structure with an interparticle distance $d \sim 2.5-4R$ in which R stands for the colloid radius [94]. A similar result had also been obtained by Gurfein et al. ($d/R = 3$) [93]. Deeper quenches lead to an increased volume

of minority (crystalline) phase, with the total colloid concentration kept constant, which is expected for a true phase separation. Here the ternary phase behaviour results from immiscibility between the colloids and one of the liquid components [94]. Via determining phase boundaries, tie lines, and the critical line, the authors constructed the ternary phase prism of their system [96] and it was observed the ternary mixture phase separates at temperatures below the binary phase boundary, which leads to the conclusion that the phase-coexistence curve is altered upon addition of colloids. According to the authors, the phase separation is no longer like binary, but should be viewed as ternary.

The observation that phase separation occurs at a lower temperature when colloids are inserted is found theoretically by Sluckin [95], he elucidates that prior to actual phase separation the adsorbed liquid can exist already between colloids due to the lower partial pressure of the adsorbate. Sluckin explains that the colloids, when aggregated, are kept in place by the preferred phase that has a lower partial pressure that provides the force needed to keep the particles together [95]. Moreover, if the colloids are sufficiently monodisperse, they are expected to aggregate into a colloidal crystal with a well-defined crystal structure, which, as previously mentioned, is observed experimentally for charge-stabilized particles [93, 94].

Löwen studied colloidal fluids near a solvent transition by theoretical analysis and simulation, taking into account the energy cost of liquid-liquid interfaces when the metastable phase is forming during phase separation [92]; he finds that the formation of a percolating structure of colloids is likely, starting off from either a homogeneous mixture or from a situation in which the colloids are initially already coated by a layer of metastable phase. Löwen states that it would be interesting to verify this predicted percolation character of the phase transition directly in real space studies.

In summary, observations in various off-critical binary-liquid systems containing different kinds of colloids show interesting phenomena like clustering prior to phase separation and wetting, in which preferential adsorption occurs that is more important on the side of the coexistence curve which is poor in the adsorbed component. Phenomena like pretransitional clustering and wetting are effects on which is generally agreed, but other aspects, like the existence of a prewetting layer and whether this should be interpreted as a pseudobinary or ternary phase separation, are still debated.

4.2 Experimental Methods

Materials Poly(methyl methacrylate) (PMMA) colloids were synthesized via a dispersion polymerization method by A. B. Schofield, after which they were washed 6-8 times with hexane and subsequently dried under vacuum at 45^{o}C. The PMMA colloids, ∼530nm radius,

are sterically-stabilized by polyhydroxystearic acid (PHS). Dodecane (Acros Organics, 99%), pentanol (Fisher Scientific, >98%), sodium dodecyl sulphate (abbr. SDS, Acros Organics, 99% for biochemistry), and water (Fisher Scientific, HPLC grade) were used as received. Microemulsion samples were carefully prepared by weight [26] with compositions clarified in table 4.1. The concentration regimes used are illustrated in the experimentally-determined phase diagram [26] in Fig. 4.2. Note that the water to surfactant ratio is held constant in all experiments; $w/s = 1.552$. The microemulsion is not density matched with the colloidal particles.

location in phase diagram	*dodecane*	*pentanol*	*w/s*
high micelle concentration	68.0%	15.8%	16.2%
critical	71.87%	15.39%	12.74%
low micelle concentration	75.25%	14.55%	10.2%

Table 4.1: Compositions of the microemulsions used in the experiments. The percentages represent weight %. The water to surfactant ratio is held constant in all experiments; $w/s = 1.552$.

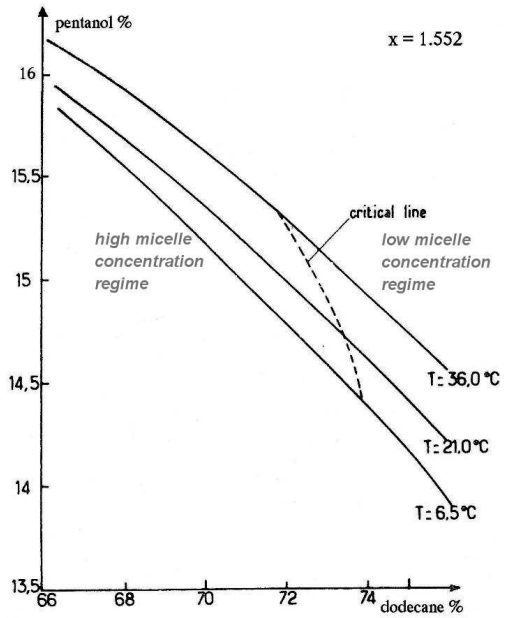

Figure 4.2: Phase diagram of the microemulsion system used [26] in which the concentration regimes studied are indicated (weight %). X represents the water to surfactant ratio (1.552). The solid lines represent the coexistence lines for specified temperatures. The critical points for different temperatures form the critical line, which is indicated by the dashed line.

Micelles Knowledge of the sizes of the micelles is important because of possible depletion interactions between the colloids due to the micelles. The sizes and number densities of various microemulsion samples of different compositions (in the absence of colloids) were measured

using dynamic light scattering (DLS) with 540 nm light from an Ar-ion laser, and scattered light was measured at an angle of 20^o.

Phase behaviour Phase behaviour was studied using bright-field optical microscopy (Olympus BX50) under controlled temperature. A temperature stage (Linkam Instruments) was used with which the temperature was varied at a 0.1^oC/minute rate or faster. The samples are studied in glass cuvettes (Starna) which were cleaned thoroughly (Decon) and dried (at 60^o for at least 5 hours) carefully prior to use. Samples were transferred into the cuvettes using a Pasteur pipette. Immediately before studying the sample it was mixed vigorously because the colloids sediment in time (30-40min.).

Fluorescence studies To study the microemulsion behaviour in greater detail, fluorescence confocal microscopy was used, on the Biorad system E800. The PMMA particles and the water in the micelles are fluorescently labeled, with NBD (7-nitrobenz-2-oxa-1,3-diazol-4-yl (CAS 10199-89-0)) and oxazine 170 perchlorate (CAS 62669-60-7), respectively. NBD can be exited using the 488 nm Ar laser with the emitted light collected using the HQ515/30 emission filter, and oxazine 170 perchlorate is excited using the 637 nm laser with the emitted light collected using the HQ660LP filter, which means that the signals from the two different dyes can be well separated. This allows us to study the movement of the PMMA colloids and micelles independently.

Digital Image Analysis / Processing The optical image, which is formed by the microscope, is divided into pixels on a rectangular grid ('sampled'), such that the image is described by coordinate positions and the light intensity at each coordinate position is represented by a positive integer. After acquisition, the image appearance is enhanced, for better contrast, visualization of features, and to facilitate more accurate image analysis. Image subtraction is a good tool to use when changes between subsequent images are of interest, as this technique highlight whatever has changed between the two images. In samples where no colloids are present, the subtraction of a background image is used to enhance images. When there are colloids in the sample this tool can not be applied, because the colloids are not stationary. For the processing of images, contrast enhancement and sharpening of features in images are the employed techniques. The optical microscopy images taken in experiments in the project consist of a range of gray scale values, where the intensity lies between the intensities I_1 (e.g. 35) and I_2 (e.g. 180), instead of between 0 (I_{min}) and 255 (I_{max}). The contrast can be increased via a technique called 'contrast stretching'. For example when I_1 to I_2 gives the intensity range of interest, then a scaling transformation can be used to map the image intensity with the range of 0 to 255 [117]. Sharpening the image improves the visualization of features. Spatial filtering can be used, here the gray level of each pixel is replaced with the weighted average of neighbouring pixels that fall within the window of the (chosen) group of pixels. Here a high-pass filter needs to be used (low-pass smooths out image), and this operation can be achieved via adding gradient information to the image (some form of the derivative of image is added

to the image) [117]. In the kernel the minimum and maximum wavelength cutoffs need to be specified, in which the lower cutoff is usually one pixel and the maximum cutoff the size (in pixels) of the object(s) of interest (such as colloids) [117].

4.3 Results and discussion

In this section results obtained via direct observation of the phase-separating microemulsion with sterically-stabilized particles inserted are presented. This is the first study by direct imaging of pre-transistional clustering in a phase-separating microemulsion system. In addition, previous studies on this type of system have been performed with colloids that are charge-stabilized [93, 94] rather than sterically-stabilized as in the present study.

4.3.1 No colloids

The pure microemulsion system behaviour was studied as a function of composition using bright-field microscopy. Early studies demonstrated that the system behaves like a binary-liquid mixture and shows analogous phase behaviour [32]. At a given composition a phase transition can be induced by raising the temperature and depending on this exact composition the microemulsion will phase separate either via nucleation and growth or spinodal decomposition. The system is very sensitive, in the sense that when there is a slight composition change, that the phase-transition temperature changes already noticeable. However, the phase-transition mechanism remains unchanged. As mentioned, this system is intrinsically slow, which facilitates experimental study by direct imaging [32]. In Fig. 4.3 the phase-separation processes are illustrated in images taken using bright-field microscopy. The different phase-separation mechanisms can be distinguished well using optical microscopy; both nucleation and growth and spinodal decomposition can be clearly followed over time, see Fig. 4.3. It is known that attractions between the micelles can be expected at the phase separation, which may lead to clustering or coalescence [18, 19, 23, 29]. The sizes of the micelles or clusters of micelles of various microemulsion compositions were investigated using dynamic light scattering (DLS). It was found that the micelle or micellar cluster sizes vary significantly depending on the exact microemulsion composition. Depending on temperature the interaction between the micelles varies, such that it gets stronger as the temperature is raised, as is expected with a lower critical-solution temperature (LCST) [3]. A very dilute microemulsion solution, with the composition chosen such that no phase separation would occur close to room temperature, was prepared so that the size of individual micelles could be measured. The dodecane concentration was

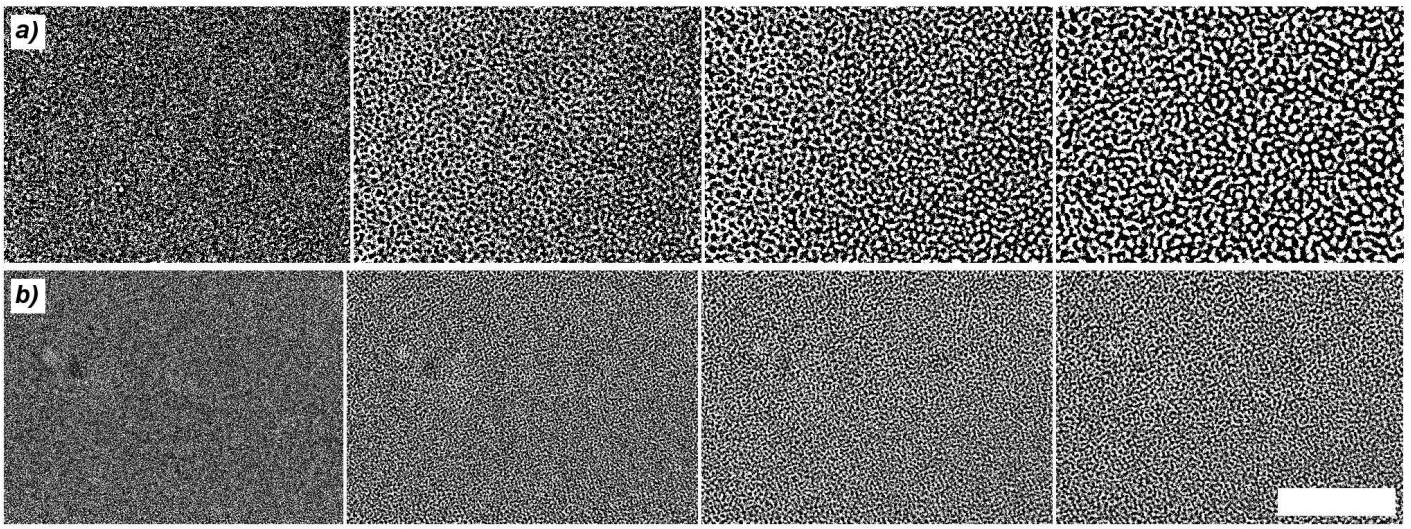

Figure 4.3: (a) Optical images of the nucleation and growth process (10 seconds between images), $T_{start} = 34^oC$. (Starting composition: dodecane: 68%, pentanol: 15.8%, w/s: 16.2%). Contrast enhancement has been used to ease visualization. (b) Spinodal decomposition (30 seconds between images), $T_{start} = 33^oC$. The warming rate is 0.1°C/min. (Starting composition: dodecane: 71.8%, pentanol: 15.4%, w/s: 12.8%). Background subtraction has been used to enhance visualization. (scale bar indicates 100 μm).

$80\%_{wt}$ rather than $68\%_{wt}$ as was used in the experiments in the off-critical regime. The microemulsion for the DLS investigation was prepared with a slightly higher pentanol concentration to prevent that phase separation would occur at room temperature (from Fig. 4.2 can be seen that the transition temperature increases when the pentanol concentration is higher). The micelle (cluster) size will not be affected in a major way, as it is only a small change in concentration ($15.85\%_{wt}$ instead of $15.8\%_{wt}$). The sample was prepared by weight, and a portion was taken away for the investigation of the microemulsion before phase separation. After this the sample was warmed up to induce phase separation and after equilibration the top phase (micellar gas) and bottom phase (micellar liquid) were separated from each other using Pasteur pipettes. The to be measured solutions were all put into cuvettes used for DLS experiments immediately after preparation. Prior to measuring (at room temperature), the cuvette was placed in the measurement chamber and left to equilibrate for 10 minutes. The light scattering results obtained for the micelle sizes are presented in table 4.2. In the dilute microemulsion (first column) the aim was to measure the size of individual micelles (6.5 nm); by keeping the micelle concentration as low as possible clustering of the micelles should mostly be prevented. The sizes of the micellar clusters in a microemulsion typically used in the experiments (second column) are 74.7 nm, which means that the micelles are in clusters as the micelle concentration is higher. After phase separation

micro-emulsion	*dilute*	*before phase separation*	*bottom phase (micellar liquid)*	*top phase (micellar gas)*
diameter	6.5±0.18 nm	74.7±9.6 nm	54.1±1.5 nm	21.4±0.3 nm
density	0.759 g/ml	0.792 g/ml	0.796 g/ml	0.785 g/ml

Table 4.2: Sizes (diameter) of (clusters of) micelles determined via dynamic light scattering at room temperature in the microemulsion. The second column is a very *dilute system* (dodecane is 80%), so that the size of individual micelles rather than cluster could be measured. The third column contains the information of a microemulsion used typically in the experiments, where the dodecane concentration is 68% (table 4.1). For this composition the transition temperature is approximately 31-33°C (see Fig. 4.2). The last two columns contain the size information from micelles that are in the bottom and top phase after phase separation. The measured density of dodecane is 0.745 g/ml. In all samples the water to surfactant ratio used is 1.552 [30].

the microemulsion with this composition the sizes of the micellar clusters are found to be 54.1 nm and 21.4 nm for the liquid and gas phase respectively. During phase separation the micelles are interacting with each other and can rearrange [19]. After phase separation the micellar clusters are distributed over the liquid and gas phase, the micelles have rearranged such that in each phase differently sized clusters exist, in different concentrations. In the liquid phase there is a higher concentration of micelles (micellar clusters) than in the gas phase (hence the naming of 'liquid' and 'gas' phase).

From the microscopy images shown in Fig. 4.3 it can be seen that the microemulsion system shows behaviour analogous to that of a binary-liquid mixture in the sense that it has corresponding phase-separation mechanisms; nucleation and growth as well as spinodal decomposition is observed. Previous researchers have assumed that the (clusters of) micelles remain unchanged during phase separation [28], but this is not the case as has been found in the dynamic light scattering experiments performed in this study (table 4.2). The micelle or micelle cluster sizes before and after phase separation vary (as found using DLS table 4.2), and there are different micelle sizes and concentrations in the micellar gas and liquid phase, which confirms that the micelles are interacting with each other during phase separation. Studies of micellar interaction have revealed that there is an increased attraction strength between micelle droplets as the temperature is raised up to T_c, and that as a result transient aggregates can form [18, 29]. A light scattering study of several microemulsions with differently sized alcohol molecules revealed that in the case of pentanol (used in current study) the micellar interactions are most strongly attractive compared to other alcohols [23]. It is evident in our experiments that these increased attractions between the micelles lead to their clustering when phase separation is induced, because after phase separation larger (clusters of) micelles are still present (table 4.2). In the situation present in our system these findings might explain the observed micelle sizes or clusters. The occurrence of a micellar transition, the clustering (rearranging), during phase separation would explain

the observation of the appearance of different micelle sizes or clusters after the phase separation has completed.

4.3.2 Insertion of colloids

Different composition regimes were studied with varying colloid concentration, and rich behaviour was observed. The colloids used are sterically-stabilized. The behaviour of the system was studied as a function of colloid weight fraction, ϕ, and changes in behaviour were induced by raising the temperature at a fixed warming rate in all composition regimes. Results obtained in the critical regime and pretransitional off-critical (at high micelle concentration) regime are presented below. The results obtained in the late-stage low and high micelle concentration regime are described in chapter 5. In the composition regimes studied, it was verified that after phase separation the colloids prefer to partition into the micellar gas phase, even though the mechanism depends greatly on the initial composition of the microemulsion. As stated before, the microemulsion system is very sensitive, in the sense that when there is a slight composition change, that the phase-transition temperature changes already noticeable. However, the phase-transition mechanism remains unchanged, which is important. This is true also in the case when colloids are added to the microemulsion.

Critical regime

The microemulsions with a critical composition were prepared before dispersing colloids in them. Microscopy studies were performed immediately after the preparation of the sample. The effect of different colloid concentrations on the phase separation was studied, whilst other parameters were kept constant (microemulsion composition and warming rate). For low colloid concentrations bright-field microscopy was used, but when higher colloid concentrations were studied, fluorescence confocal microscopy was required. In Fig. 4.4 observations made using bright-field microscopy and confocal microscopy (used for higher ϕ) are shown, from which it is clear that spinodal decomposition continues to occur in the presence of particles (at least above the resolution limit). All samples were quenched at a rate of 2^oC/min into the unstable region. No clustering prior to the phase separation was observed for low colloid concentration (ϕ=0.0-0.5%), but for ϕ=2% the colloids begin to show some clustering when the phase separation starts. For ϕ=2% this effect is not strong, there is only slight clustering and the clusters are not so large as for higher colloid concentrations. When the colloidal concentration became high (ϕ=5%), stronger clustering was observed and phase separation would occur, regardless of the microemulsion phase-separation temperature, see Fig. 4.5. This is most likely due to depletion interaction, but this also

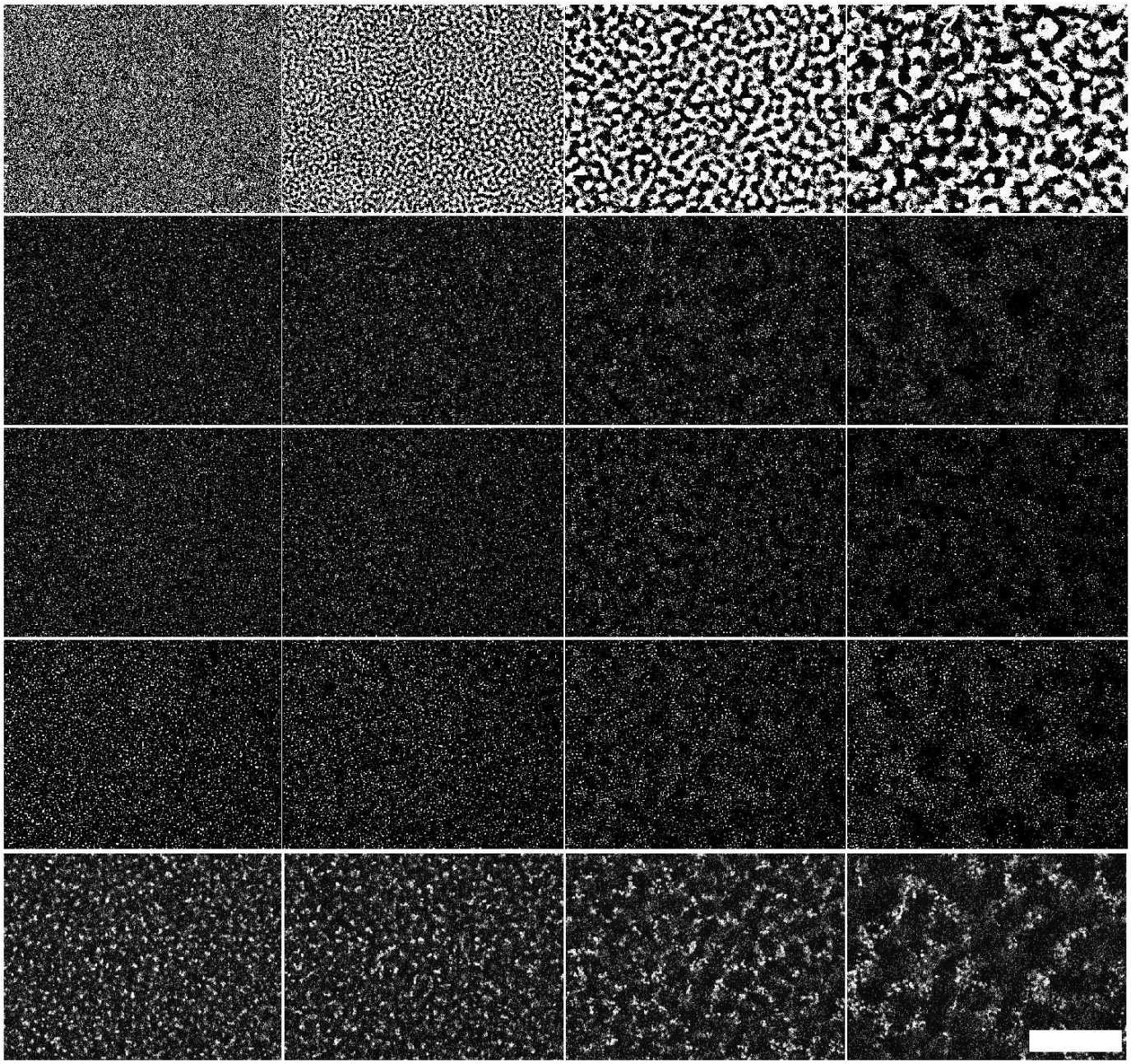

Figure 4.4: Microscopy images show the different stages observed in the phase-separation process observed in the critical regime for different colloid concentrations: $0.0\%_{wt}$, $0.15\%_{wt}$, $0.25\%_{wt}$, $0.50\%_{wt}$, and $2\%_{wt}$ from top to bottom. The times after the onset of phase separation (using a 2^{o}C/min rate) in seconds is from left to right: 0, 6, 12, and 18 seconds (scalebar indicates 100 μm). At later times than shown in this figure gravity start to have a profound effect on the phase separation. Background subtraction has been used to enhance visualization for the $0.0\%_{wt}$ colloid concentration (optical microscopy). The images made for microemulsions with the fluorescently labeled colloids inserted were made using confocal microscopy. (Composition of the pure microemulsion: dodecane: 71.8%, pentanol: 15.4%, w/s: 12.8%).

could be a three component effect (Kaler et al. [94,96], see p. 60), because the presence of the PMMA colloids profoundly modify the microemulsion system. If there would be three-phase coexistence, different behaviour for temperatures much lower than the transition temperature is expected, for example the absence of clustering and phase separation. To make sure absolutely no phase separation, due to a three component effect, occurred in the system at *high* colloid concentration, it was studied more than 25^{o}C below the transition temperature of the pure microemulsion system, Fig. 4.5. The depletion range (the ratio of colloid radius (530nm) over micelle radius (37nm))

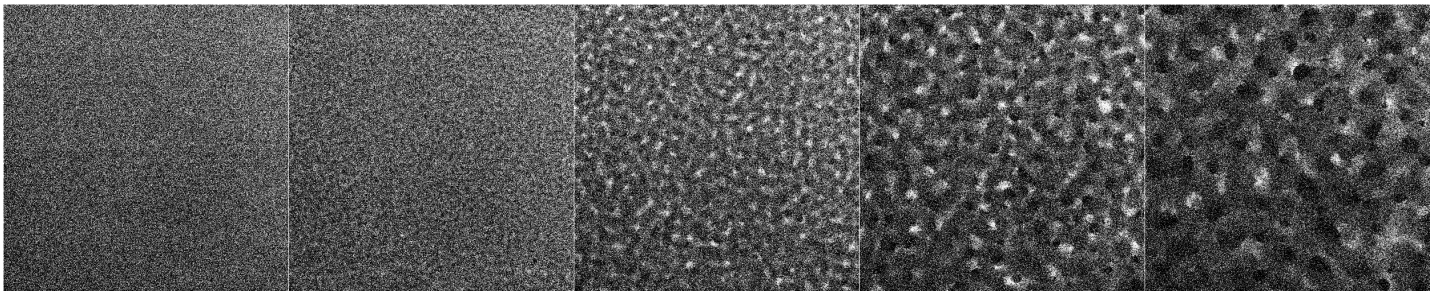

Figure 4.5: High colloidal concentration: ϕ=5%. Phase separation will always occur, regardless of the microemulsion phase-separation temperature. Sides of the confocal images are 1.2mm. $T_{measurement}$ = 0^{o}C. The phase-separation temperature of the pure microemulsion (with critical composition (table 4.1)) with no colloids is $\sim 33^oC$, Fig. 4.2.

is 14. The behaviour at 25^{o}C below the transition temperature was not found to be different from the behaviour of only several degrees below the transition temperature, which means that the clustering effect is not a result from a three component effect, and that depletion interaction at this composition is the most probable cause of the phase separation at high colloid concentration.

The characteristic spinodal pattern was observed for the concentration range studied (0.0-2.0%); however, the spinodal domain size at a chosen time after the quench increases when colloids are present in the microemulsion. The characteristic spinodal pattern was still observed when colloids were added to the pure microemulsion, which indicates the system is not altered significantly upon addition of colloids. The colloids have stronger affinity for the micellar gas phase and during phase separation the colloids partition into this phase by moving into micellar gas regions only after which interfaces become visible. Before interfaces are formed, the phases are diffusing to demix, and the particles go into their preferred phase. It is striking that the spinodal domain size grows faster compared to when no colloids are present. On one hand we would expect the dynamics to slow down when a component with larger size (colloids, micelles) is added to the system [1], because these structures diffuse much more slowly than molecules. However, in this picture new interactions are not taken into account.

Micellar interactions are found to become stronger as the temperature is raised up to T_c, and transient aggregates of the micelles can form [18,29]. When the phase boundary is approached the micelles start to attract each other more and can form aggregates. As a result of this the depletion interaction (p. 23) between the micelles and the colloids changes, as the depletant basically increases in size whilst the volume fraction remains the same. Now the strength of depletion interaction between the colloids remains the same as the volume fraction does not change, but the range of interaction (set by the depletant size) increases, which means that depletion becomes more likely to occur. Because of this the faster growth of domain sizes can be explained, because the colloids and micelles are segregating into different regions because of the phase separation driven by the interactions between the micelles as well as of the enhanced depletion attraction. The phase separation happens faster when colloids are inserted compared to when no colloids are present.

The sizes of the micelles in the micellar gas phase were measured using DLS to determine if the micelles cluster upon addition of PMMA colloids. The composition of

pure microemulsion	*0.5% PMMA*	*1% PMMA*
21nm	200nm	320nm

Table 4.3: Sizes of micelles determined using DLS in the micellar gas phase after phase separation has taken place without and with PMMA colloids inserted. (Pure microemulsion composition: dodecane: 68%, pentanol: 15.8%, w/s: 16.2%).

the microemulsions in the three solutions is the same (68% dodecane, 15.8% pentanol, 16.2% w/s). The data suggests that upon increased PMMA concentration the micelles show more clustering, which leads to an increased depletion interaction.

From the results here it can be seen that depending on the colloid concentration the phase separation is driven by different effects. At low colloid concentration the phase separation is primarily driven by interaction between the micelles, whilst at high colloid concentration it is primarily driven by depletion interaction (without particles the solution does not phase separate). Upon increasing colloid concentration the depletion interaction becomes more and more pronounced during phase separation driven by the micellar interaction, up to a point where it becomes dominant and drives the phase separation.

No strong clustering prior to the phase separation is observed (for ϕ up to 0.5%), which indicates that the clustering in the critical regime is a much weaker effect than for off-critical (high micelle concentration side) quenches. It appears unlikely that the critical Casimir effect [89] is dominant in this system, because of the absence of strong clustering between the colloids.

The result that pronounced particle clustering is not observed in the critical regime

contrasts with work on some binary-liquid mixtures reported in literature [89], in which the observed clustering is explained as being due to the critical Casimir interaction. Here an effective attractive interaction between colloids is induced by the critical fluctuations of the solvent. In the case of a binary-liquid mixture these fluctuations range from very small (size of the molecules) to very large (wavelength of visible light), but this is different in the case of the microemulsion because the subunits here are the micelles, which are much larger than single molecules. The continuous phase in the microemulsion is dodecane rather than a binary-liquid mixture, which means that the critical fluctuations are connected with the micelles. Critical fluctuations that are comparable to the size of a micelle can be suppressed [118, 119]. Critical concentration fluctuations are induced when the critical point is approached, requiring motion of the micelles. In certain regions the concentration increases as a result of the fluctuations, which causes the stress in these regions to increase because the micelles are forced to move towards the same region. The micelles are pushed away from the region again because of the increased stress. In the regions where the concentration fluctuations decrease the micelle concentration, the stress is lowered. Because of the lowered stress in these regions the micelles are drawn to these regions. The stress that is induced in this manner works in the opposite direction of the concentration fluctuation [119]. Because of this the critical concentration fluctuation is suppressed, which means that in turn also the critical Casimir force is suppressed as this is induced by critical fluctuations of the solvent.

4.4 Off-critical high micelle concentration

Immediately after dispersing PMMA colloids in the microemulsion the behaviour is studied in real time with bright-field microscopy. The system is brought from the one-phase microemulsion region to the binodal via warming at a rate of 0.1^{o}C/min. When studying this regime, different stages in the phase separation process can be distinguished, as can be seen in Fig. 4.6, in which microscopy results obtained in this regime are presented. For very low ϕ, for example for $\phi = 0.05\%$, on warming to the binodal the gas phase nucleates around single colloids, because this is the phase preferred by the colloids. Initially, when the binodal is approached via increasing the temperature slowly, individual colloids cluster together into irregularly shaped clusters, and these cluster together with other clusters (Fig. 4.7). Dodecane is likely to adsorb onto the surface of the colloids, because these are hydrophobic. The interaction between the micelles and colloids is weakly repulsive due to the steric hindrance originating from the long-chain molecules present on both the colloidal and micellar surfaces. When the binodal is approached, there are already fluctuations in the solvent occurring, the

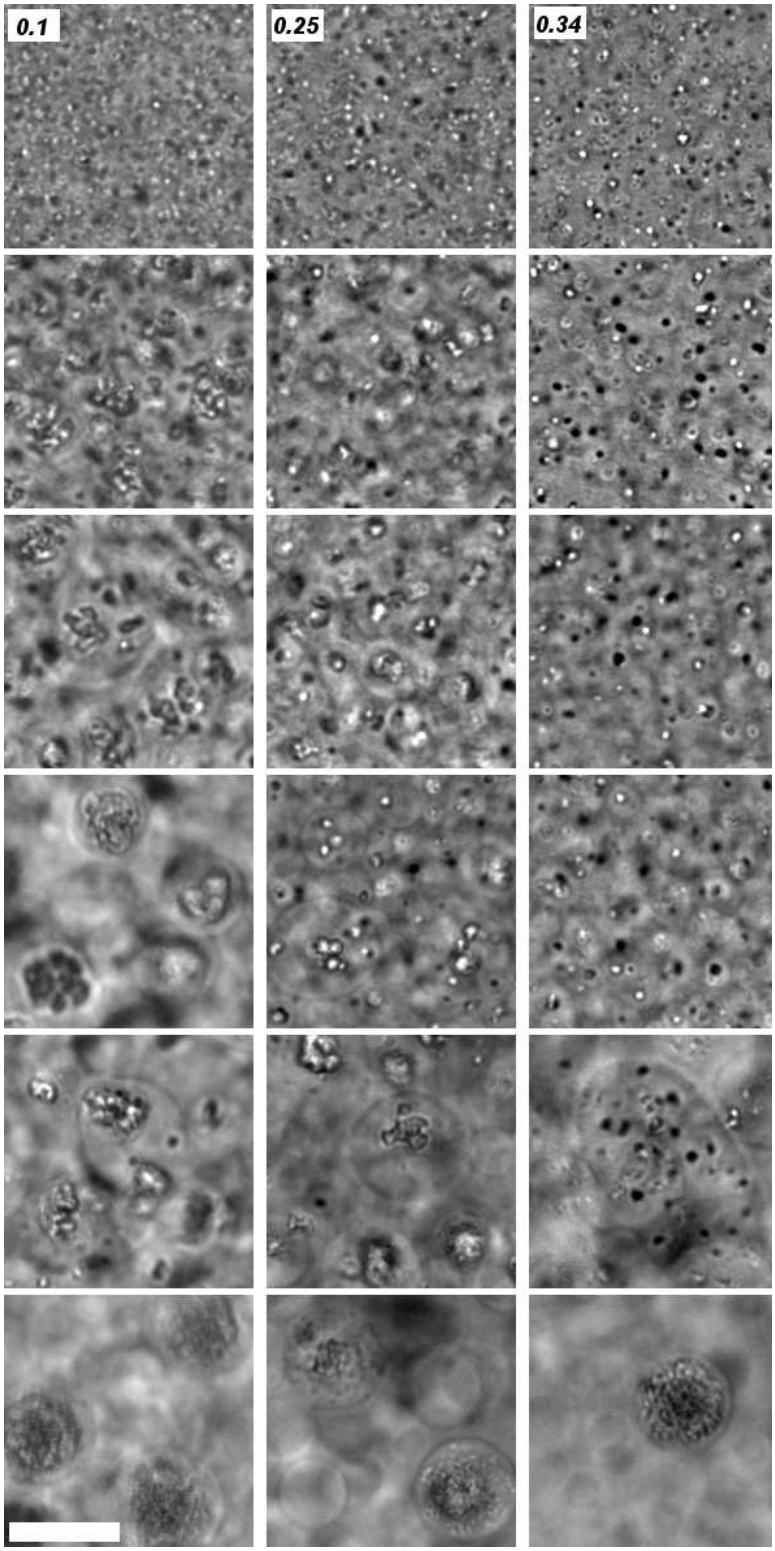

Figure 4.6: Microscopy images show the different stages observed in the phase separation process observed off-critical (high micelle concentration) for different colloid concentrations: $0.1\%_{wt}$, $0.25\%_{wt}$ and $0.34\%_{wt}$ from left to right (scalebar indicates 50 μm). From top to bottom the temperature is increased, which induces changes in the behaviour. Initially the colloids are freely dispersed, but when the binodal is approached, via increasing the temperature, clustering starts. When the binodal is crossed (between first and second image in each sequence) the micellar gas phase nucleates around the clusters of colloids. Droplets are coalescing so that they grow in size, as well as the clusters contained in them. When the temperature is sufficiently high, the clustered colloids redisperse inside the micellar gas droplets, as can be seen in the last image of every series. (Pure microemulsion composition: dodecane: 68%, pentanol: 15.8%, w/s: 16.2%).

attractions between the micelles increase [22], which makes that the micelles are moving towards each other. The movement is away from the hydrophobic colloids which has the result that the colloids end up being surrounded mainly by dodecane. Because the micelles are moving towards each other they can cluster, which increases the depletion interaction (p. 23) range which can cause the colloids to cluster. On increasing colloid concentration ϕ the clustering becomes more and more pronounced. Only when the colloidal weight fraction is high enough, clustering prior to phase separation becomes visible. When the temperature is raised to the point that the binodal is crossed a droplet around the colloidal clusters becomes visible and grows larger, and eventually the colloids are entrained inside this nucleated droplet.

To investigate the behaviour of the microemulsion when the binodal is approached confocal fluorescence microscopy studies were performed. Both the micelles and the PMMA colloids are fluorescently labeled, which enables to image these components simultaneously in different channels. The aim is to investigate if the micelles are moving away from the colloids prior to the nucleation of the micellar gas phase around the PMMA colloids. In Fig. 4.8 confocal images are shown, in the top row the colloids are imaged and in the bottom row the micelles are imaged. There is one minute between the subsequent images.

Making measurements of cluster growth in time is hard to achieve because the system is very mobile; after phase separation starts components start moving due to density differences between them. Because of this movement in the sample objects move in and out of focus of the microscope which inhibits taking appropriate data that would be required for accurate analysis of the sizes of objects as a function of time.

When the temperature is increased, after the micellar gas phase has started to nucleate, the clusters within the micellar gas droplets undergo a colloidal phase transition. The uncharged colloids go from the colloidal solid state (clustered) to the colloidal liquid state (dispersed within droplet), which also is visible in the images presented in Fig. 4.6. As the temperature continues to rise after the microemulsion phase separation has occurred there is still material exchange between the gas and liquid phase, and at some stage when the gas phase composition is optimal the colloids can disperse within the micellar gas phase droplets. This can be understood when depletion interaction is considered (p. 23). When the colloids are dispersed in the microemulsion, dodecane is likely to adsorb onto the colloids' surface as this is hydrophobic. The interaction between the colloids and micelles is weakly repulsive due to the steric hindrance between them. The more colloids are present, the more micelles are excluded from colloidal regions and thus forced to be closer to other micelles. This could lead to micellar aggregation when the colloid concentration is sufficiently high. Micellar aggregation leads to an increased depletion interaction between the colloids and the

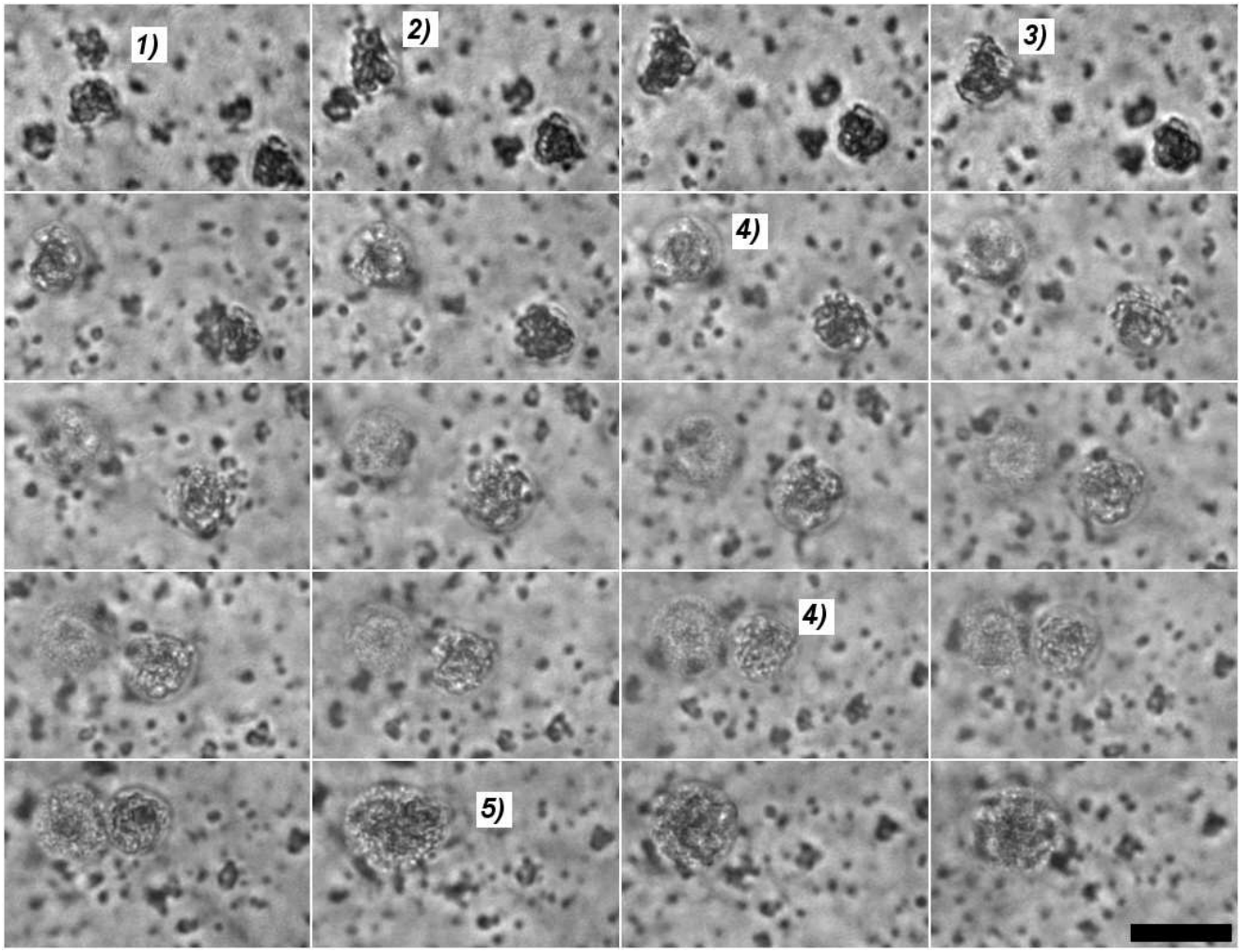

Figure 4.7: In this sequence the binodal line is being crossed. Prior to crossing it can be seen that the colloids initially cluster together to form irregularly shaped clusters (1). These clusters then cluster together (2) after which a wetting layer of the micellar gas phase forms around these clusters (3), which means that the binodal line has been crossed. The binodal line is crossed between the third and and fourth image of the sequence. When the temperature is sufficiently high the colloids redisperse within the droplet they are entrained in (4), the clusters lose their irregular shape and become more and more spherical. The colloids are not strongly clustered anymore, and colloids are leaving the cluster, they redisperse inside the micellar gas droplet. Droplets with colloids redispersed in them coalesce (5). (Pure microemulsion composition: dodecane: 68%, pentanol: 15.8%, w/s: 16.2%). The time between the images is 6 seconds (scale bar indicates 50 μm).

micelles (depletant), the micellar clustering has the result that the depletant increases in size whilst the volume fraction remains constant (when dodecane adsorption by the colloids is ignored). The increased depletant size makes that the range of depletion interaction increases, which means that depletion is more likely to occur.

After crossing the binodal the colloidal clusters are entrained within a micellar gas droplet. It is striking that the colloids do not immediately redisperse once they are

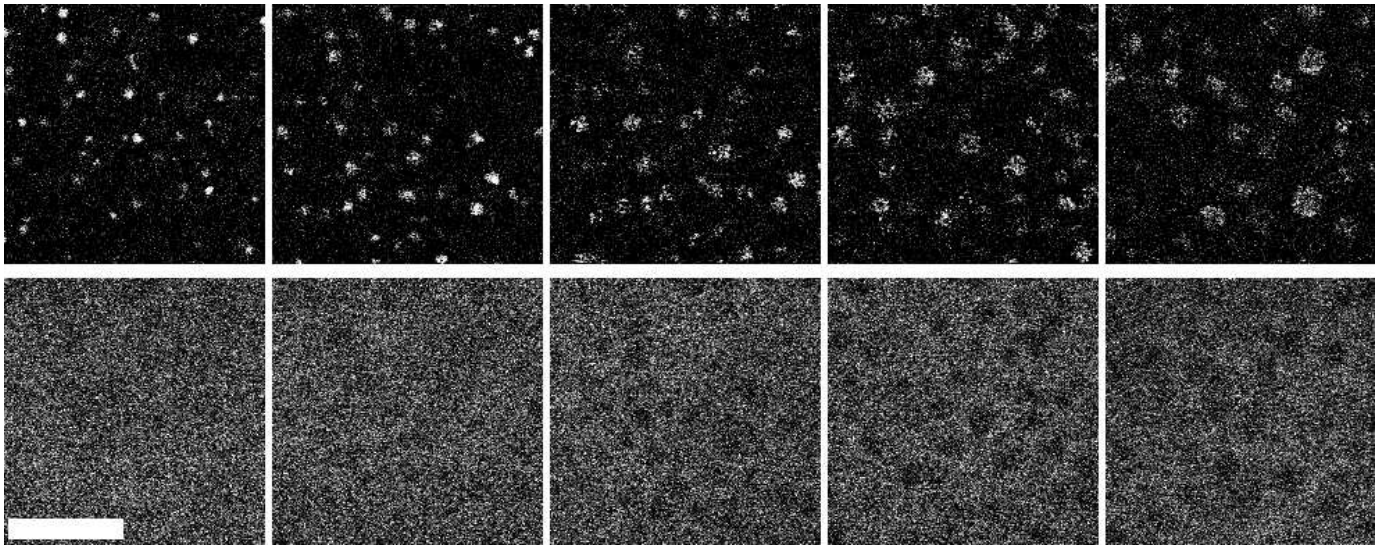

Figure 4.8: In this image sequence the movement of colloids (top row) and the micelles (bottom row) are imaged using fluorescence confocal microscopy. It can be seen that upon approaching the binodal the colloids are clustering, and that the micelles are expelled from the colloid region. Later, after crossing the binodal (between second and third image), the clusters entrained in micellar gas phase droplets disperse again. In the bottom row only the micelles are imaged, dark regions in this row indicate that micelles are absent. There $2\%_{wt}$ PMMA colloids in the microemulsion. The time between subsequent images is one minute (scale bar indicates 50 μm). (Pure microemulsion composition: dodecane: 68%, pentanol: 15.8%, w/s: 16.2%).

inside the micellar gas phase. It is likely that the colloids in the cluster are held together because of the depletion interaction. This is possible because dodecane adsorbs onto the colloids because they are hydrophobic. The micelles present in the micellar gas phase act as depletant. When the temperature increases more, there is still material exchange between the micellar gas and liquid phase. More micelles migrate from the micellar gas phase to the micellar liquid phase, which means that the volume fraction of depletant in the micellar gas phase decreases. Because of this the range of depletion interaction decreases and the colloids are no longer held together by depletion interaction when the concentration of micelles (depletant) in the micellar gas phase is sufficiently low, and the colloids disperse freely in the micellar gas droplets. In Fig. 4.9 the process happening when the binodal line is approached and crossed, is illustrated.

The observations made in this off-critical high-micelle concentration regime indicate that the phase separation mechanism, nucleation, continues to occur. Nucleation of the micellar gas phase is still observed, although because of the presence of colloids also other effects, e.g. pretransitional clustering, are present in the system. After the pretransitional clustering, when the temperature is sufficiently high, the microemulsion phase separates (further) and a droplet surrounding the clusters that are large enough (to form a stable droplet on), becomes visible. Heterogeneous nucleation is the process

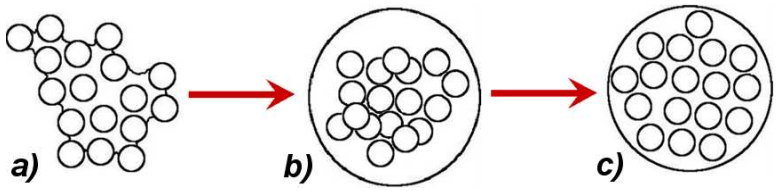

Figure 4.9: In this cartoon the colloids and the liquid phases are illustrated. (a) When the binodal line is approached via warming the system up clustering occurs. Because of fluctuations that occur in the microemulsion upon approaching the binodal dodecane can adsorb onto the colloids. Micelles are expelled from the region between the colloids. (b) The binodal has been crossed and a droplet of micellar gas phase has formed around the cluster, in which the colloids are held together via depletion interaction. (c) After material exchange between the micellar liquid and gas phase the colloids disperse within the micellar gas phase droplet.

responsible for the observed droplets in this microemulsion composition regime. From the data it is hard to tell at which cluster size exactly the droplet around colloidal clusters appears, because not only the rise in temperature is responsible for inducing the phase transition and thus also the appearance of this droplet, but also the size of the clusters plays an important role in the nucleation. It is well known from classical nucleation theory [3] that for forming a stable droplet, the droplet needs to grow a certain size to be stable, resulting from the competition between forming an interface (unfavourable) versus creating the new phase (favourable). The appearance of the droplet around colloidal clusters is an interplay between these two effects, the cluster size as well as the quench depth [120]. Droplets containing colloidal clusters coalesce with each other as well as with empty droplets, so both droplet sizes and cluster sizes within these droplets increase. Although the various stages appear at different times, these can exist simultaneously, which indicates that the binodal line has been crossed; with the various stages being unfilled droplets, droplets containing clusters, and still few single colloids remain in the micellar liquid phase.

The effect of modifying the microemulsion system with insertion of colloids on the phase-separation temperature is an important aspect of this study. The phase-separation temperature (T_{PS}) changes dramatically when colloids are present in the microemulsion, and more interestingly, the transition temperature change depends on the amount of colloids that are added. To understand this properly, it helps to look at the experimental phase diagram in Fig. 4.2 on p. 62. In this diagram one can see that when the dodecane concentration is higher, that the temperature at which the microemulsion system phase separates, increases. Also, the T_{PS} increases upon an increased concentration of pentanol in the microemulsion. When colloids are added to the system the temperature at which the microemulsion phase separates increases with several degrees. This means that effectively there is a higher concentration of

dodecane or pentanol in the system. The pentanol acts as cosurfactant in the micelles, which means that most of the pentanol is entrained in the micelles, rather than freely in the solution. Because of this, the addition of colloids is unlikely to have an effect on the actual amount of pentanol within the micelles. This means that the addition of PMMA colloids to the microemulsion (which increases T_{PS}) has an effect on the dodecane in the microemulsion. Dodecane is likely to adsorb onto the colloids' surface as this is hydrophobic. If this would be the case then there would be less dodecane in the bulk microemulsion which means there is effectively more pentanol. This implies that the more colloids are added to the system, the more dodecane would be adsorbing onto the colloids' surfaces leading to an effectively higher pentanol concentration in the bulk microemulsion. A higher pentanol concentration would lead to a higher T_{PS}, and if it is true that the (effective) pentanol concentration increases one would expect the amount of final phase to change (Lever rule). This leads to the question, does the final amount of phase change upon addition of colloids? For thinking about this it helps to look at the following schematic (Fig. 4.10) to see what happens to the relative amounts of the formed phases when T_{PS} changes.

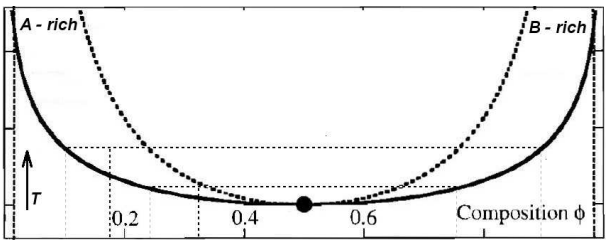

Figure 4.10: In this schematic phase diagram for a binary mixture (liquid A and liquid B) it can be visualized what happens to the amount of final phases formed when T_{PS} changes. When the mixture initially has an A-fraction of 0.18, the amounts of final phases contain a fraction of A of 0.13 and 0.88, but when the intial composition is such that the fraction of A is 0.33, the amounts of final phases contain A-fractions of 0.24 and 0.75.

In the following picture (Fig. 4.11) taken of a series of cuvettes you can see there are different amounts of final phase for different concentrations of colloids. In all cuvettes the microemulsion composition is the same, but the fraction of PMMA colloids increases from left to right in the picture. It can be seen that at low colloid concentration the colloid-rich phase decreases in volume. Upon increasing colloid fraction this trend continues, up to a certain colloid fraction ($\phi = 0.3\%_{wt}$) after which the colloid rich phase increases its volume again. Temperature measurements were made for colloid fractions up to $\phi = 0.3\%_{wt}$, Fig. 4.11 (a). From these can be seen that initially after adding colloids T_{PS} goes up, and after adding more colloids T_{PS} goes up more. This behaviour in varying T_{PS} is also reflected in the relative volumes of the phases formed after phase separation. From the schematic (Fig. 4.10) can be seen that if

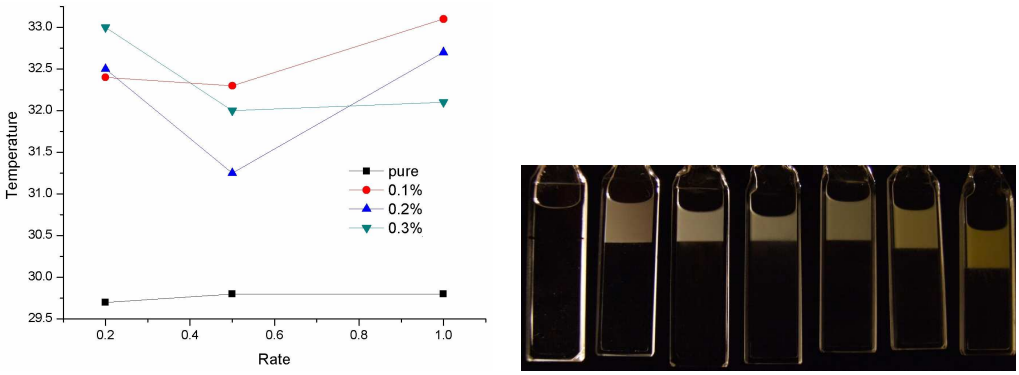

(a) (b)

Figure 4.11: (a) In this graph the transition temperatures as a function of warming rate and for different colloid weight fractions are plotted. It can be seen that upon addition of colloid in the microemulsion the transition temperature increases up to a certain point. After that point when there are more colloids present the transition temperature decreases again. (b) Cuvettes with varying colloid concentration (and top phase fraction) from left to right: $\phi = 0\%_{wt}$ (20.7%), $\phi = 0.1\%_{wt}$ (26.6%), $\phi = 0.2\%_{wt}$ (20.0%), $\phi = 0.3\%_{wt}$ (16.8%), $\phi = 0.5\%_{wt}$ (26.4%), $\phi = 1\%_{wt}$ (28.5%), $\phi = 2\%_{wt}$ (31.7%). It is clear that the relative amounts of final phases formed after phase separation varies with varying colloid concentration. (Pure microemulsion composition: dodecane: 68%, pentanol: 15.8%, w/s: 16.2%).

T_{PS} is higher, that the relative volumes of the phases changes. The higher T_{PS}, the smaller the top phase fraction (which contains the micellar gas phase with colloids). Both the temperature measurements as the relative amounts of the phases after phase separation confirm that when colloids are added that the effective composition of the bulk microemulsion changes, in the sense that the effective concentration of pentanol is increased, due to the adsorption of dodecane onto the colloids' surfaces.

At some colloid concentration (ϕ>0.3%$_{wt}$) the top phase fraction starts to increase in relative volume again. This means that a lower T_{PS} is expected here, but for systems with ϕ greater than 0.3%$_{wt}$ T_{PS} has not been measured. For low colloid concentrations T_{PS} can be obtained via studies with bright-field optical microscopy. For higher colloid concentrations this technique can not be used anymore as the system is then too highly concentrated for enough light to be transmitted. Fluorescence confocal microscopy could not be used either, as the interfaces can not be imaged.

The observation that upon addition of colloids to the microemulsion system initially T_{PS} increases, which suggests that at low ϕ there is effectively a higher concentration of pentanol. The more colloids are present, the more dodecane is adsorbed, and the higher the effective pentanol concentration in the bulk microemulsion is, leading to a higher transition temperature (Fig. 4.11(a)) and smaller top phase fraction (Fig. 4.11(b)). Upon further increase of ϕ however, above a colloid concentration of ϕ = 0.3% T_{PS} is expected to decrease again, which effectively means that there is less pentanol (or dodecane) in the microemulsion (see Fig. 4.2 on p. 62). It cannot be true

that effectively less pentanol is present in the bulk since dodecane is adsorbed onto the colloids. This means that at a higher colloid concentration (ϕ>0.3%$_{wt}$) another mechanism becomes responsible for the changed phase-separation temperature.

Due to the steric hindrance originating from the long-chain molecules present on both the colloidal and micellar surfaces the interaction between them is weakly repulsive. The more colloids are present, the more the micelles get repelled from colloid regions and thus are forced to be closer to other micelles raising the effective micellar concentration, which could lead to micellar aggregation when the colloid concentration is sufficiently high. When the micelles aggregate effectively the number of micelles in the system decreases which can account for the lower observed transition temperature. This can be understood when depletion interaction between the micelles and the colloids is considered (p. 23). The clustering of the micelles means that the depletant (the micelles) increases in size whilst the volume fraction of it remains the same (when dodecane adsorption is ignored). The increased size of the depletant makes that the range of depletion interaction increases, which means that depletion is more likely to occur. Because dodecane is adsorbed, effectively the concentration of depletant is higher, which increases the strength of the depletion interaction. The more colloids are present the stronger the micellar aggregation, and the stronger the depletion interaction between colloids. When there is a low concentration of colloids present, the phase separation induced via raising the temperature is mainly driven by micelle-micelle interactions. As the colloid concentration increases the depletion interaction between colloids becomes increasingly important, and eventually drives the phase separation, see Fig. 4.12 for a schematic illustration.

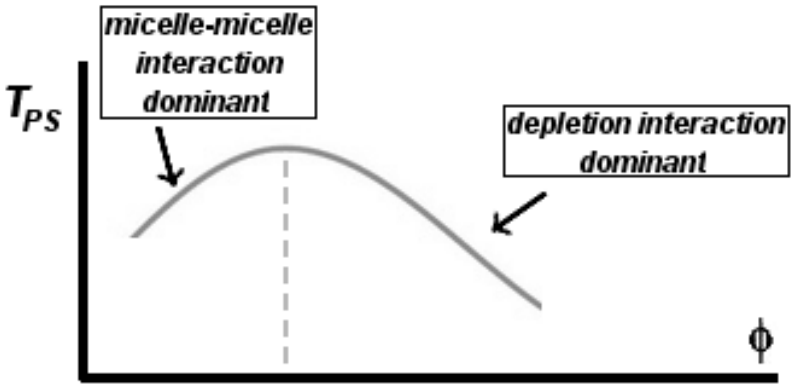

Figure 4.12: Schematic illustration of the non-monotonic trend in T_{PS} versus colloid concentration ϕ. At low ϕ the phase separation is mainly driven by micelle-micelle interactions. For this regime T_{PS} increases as ϕ increases up to a certain point where the depletion interaction between the colloids become important. For higher ϕ the phase separation is more and more driven by the depletion interaction, leading to a lower T_{PS}.

This can be seen in the effect of colloid concentration on T_{PS}. Initially (up to $\phi = 0.3\%_{wt}$) the colloids' presence does not significantly alter the depletion interaction. Here the adsorption of dodecane by the colloids is responsible for the observed increase in T_{PS}, as this leads to an effective higher concentration of pentanol in the bulk microemulsion. For higher colloid concentrations the pentanol effect appears to be less strong than the depletion interaction. For higher colloid concentrations the phase separation is more and more driven by the depletion interaction, which leads to a lower T_{PS}.

4.5 Conclusions

The experiments performed on the pure microemulsion show that this system can be studied in real time by bright-field microscopy because it is intrinsically slow. The light scattering study reveals that the micelles rearrange themselves under influence of rising temperature during phase separation, and distribute over two phases. In the one-phase regions the micelles exist in clusters of a certain size. During phase separation the micelles interact such that they form differently sized clusters that distribute over the two phases formed after phase separation. These phases are named 'micellar gas phase' (top phase, contains small amount of micelles) and 'micellar liquid phase' (bottom phase, contains large amount of micelles). The smaller clusters end up in the micellar gas phase whilst the larger clusters end up in the micellar liquid phase.

Experiments performed with PMMA colloids in the critical regime show that the phase-separation mechanism (spinodal decomposition) remains the same, but because of enhanced interactions during phase separation the growth of domains is faster. When the binodal is approached the micelles have stronger attraction [22] which leads to micellar aggregation, which in turn leads to enhanced depletion interaction between the micelles and colloids. The enhanced depletion interaction is responsible for the faster evolution during phase separation.

Experiments with added colloids in the off-critical regime show that nucleation is still the phase-separation mechanism. Initially clustering of PMMA colloids occurs, followed by the heterogeneous nucleation of the micellar gas phase on the clusters. In studies performed on this type of system with colloids in binary-liquid mixtures the clustering and wetting were identified as separate events [101]. The observations in the experiments performed agree with these results, the clustering is followed by the heterogeneous nucleation of the micellar gas phase. After the heterogeneous nucleation the clusters are entrained inside the micellar gas phase droplets. The colloids that are entrained in micellar gas droplets undergo a solid to liquid transition, which indicated that after crossing the binodal there is still material exchange between the two micellar

phases. The colloidal cluster inside the nucleated droplet is held together by depletion interaction due to the presence of the micelles. Upon temperature increase there is material exchange between the micellar gas phase (droplets) and micellar liquid phase. Micelles move out of the micellar gas phase into the micellar liquid phase, which leads to a smaller volume fraction of depletant in the micellar gas droplet containing the colloidal cluster. This decreases the strength of the depletion interaction such that the colloids redisperse within the micellar gas phase droplets.

The importance of the depletion interaction between the colloids and the micelles in the phase separation is also evidenced by the change of phase-separation temperature (T_{PS}) as function of colloid concentration. When the colloids are dispersed in the microemulsion, dodecane is likely to adsorb onto the colloids' surface as this is hydrophobic and this is consistent with our observations. The more colloids are present the stronger the micellar aggregation, and the stronger the depletion interaction between colloids. When the colloid concentration is sufficiently high, the system will always phase-separate because of the depletion interaction, also at low temperatures (as was observed in the experiments, see p. 67).
The behaviour can be interpreted as pseudobinary phase behaviour, as the phase-separation mechanism is not altered profoundly, but on the other hand the colloidal phase transition at later stage supports the view of ternary phase separation, in which the observed behaviour is an interplay of the phase behaviour of the binary pairs present in the system.

Chapter 5

Particles in a phase-separating microemulsion: late stage

In this chapter a microemulsion with colloids inserted showing phase separation upon warming is studied using optical microscopy. The focus is on the late stage behaviour during phase separation. Comets, hindered coalescence and viscoelastic effects are observed. Both creaming and sedimentation and the effects of the particles on flow behaviour play key roles.

5.1 Introduction

Here we employ a microemulsion containing reverse micelles [26] which, in a certain composition range, is found to behave in a manner analogous to binary-liquid mixtures [32], the range used for the work described in this thesis. The microemulsion system (lower consolute point) exhibits phase separation upon increasing temperature into two microemulsions with different micelle concentrations, in this thesis referred to as the micellar 'gas' phase and micellar 'liquid' phase, which respectively contain a low and high concentration of micelles [17]. Due to the presence of micelles and the composition used, the system is intrinsically slow which means that phase separation can be imaged in real time using microscopy techniques. During phase separation the colloids partition into the preferred microemulsion via a mechanism that depends on the exact initial composition of the microemulsion. This partitioning modifies both the density and flow behaviour of this phase.

Phase separation (PS) can lead to various kinds of behaviour depending on the characteristics of the components. It leads to certain types of pattern evolution, and thus plays a key role in the systems' subsequent morphology. The PS of binary liquids, where the phases occupy about the same volume, is a well known phenomenon, in which material is transported via diffusion and flow (hydrodynamic transport). This type of PS produces two types of morphologies depending on the composition; droplet and bicontinuous structures (p. 11). The PS behaviour in, for example, polymer solutions is different; in addition to the initial diffusive regime and the final hydrodynamic regime

in the evolution, there is an intermediate regime [121]. In this intermediate regime the elastic-force balance rather than the interfacial tension determines the domain morphology. This is because in this type of system there exists a fast and a slow component, the slower component cannot keep up with the deformation rate of the PS, which results in the stress being asymmetrically divided between the components. In the intermediate regime the PS is not characterized by the deformation rate induced by the PS itself, but by the rheological relaxation rate of the phase rich in the slow component. Because in the intermediate regime the viscoelastic property of the slow component determines the pattern evolution, this PS is named 'viscoelastic phase separation' (VPS). The morphologies observed in VPS are significantly different from those observed in normal fluid PS [121]. In a dynamically asymmetric mixture VPS can lead to the formation of a long-lived 'interaction network' (transient gel) of the slow components, if the attractive interactions between them are strong enough [122].

The networks that are formed in viscoelastic phase separation have the same morphology as foam structures. A foam is a dispersion of gas in a second, continuous phase, most often liquid-like in which surfactant type molecules adsorb at the interface [123]. The thin liquid film between the bubbles have such an elasticity, that applied stresses that lead to local thinning or stretching are opposed [10]. The elasticity arises due to a local increase in the surface tension when the film is stretched [10], see Fig. 5.1. The film opposes the increase of the surface tension which is due to stretching by flowing

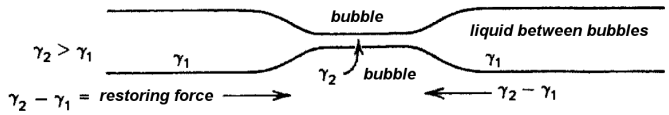

Figure 5.1: In this schematic local thinning of a liquid film is shown. In the thinned area the film is stretched leading to an increase in the area, which causes the surface tension to increase in that area. A gradient in the surface tension arises in the region between the thinned and thicker areas, which causes liquid to flow from the thicker regions to the thinner region. This prevents further thinning of the thinned area. Figure adapted from [10].

back material to the thinned region, an effect known as the Gibbs-Marangoni effect [124]. The foams' evolution depends on the drainage of the thin liquid film between the bubbles, which leads to the close approach of the bubble surfaces and coalescence can occur. Bubble coalescence leads to the collapse of the foam, and diffusion of gas between bubbles leads to coarsening of the foam (Ostwald ripening [125]). Foams can also be stabilized using other agents, for example nanoparticles [126].

When two bubbles approach each other closely enough, their interfaces interact and begin to deform [127]. When bubbles are close enough a plane-parallel thin-film between them is formed. The rate of coalescence is an important factor in foam and emulsion stability. Coalescence reduces the total interfacial area and is driven by

the interfacial tension. The effects of surface tension and surface viscosity have been modeled to predict the coalescence time for bubbles [128]. In an experimental study it is demonstrated that the coalescence dynamics of droplets is driven by surface tension, and is slowed down by viscosity for low and by inertia for high Reynolds numbers in colloid polymer mixtures [129,130]. In the experiments the slow retraction of interfaces (∼4 seconds) after a connection between the droplets was made was observed using the system with ultralow surface tension.

Polymer mixtures with colloids inserted are studied intensively due to the potential importance in material engineering [131]. Colloids in phase-separating binary polymer mixtures have been studied experimentally only in a thin film geometry so far. The focus in these studies have been on the effect of colloids on the phase-separation dynamics of the polymer blend. Tanaka et al. explored experimentally the effect of the presence of mobile and immobile particles on the pattern evolution of binary polymer mixture [132, 133], and found that the pattern evolution is strongly affected by the dynamic coupling between the phase separation and wetting. The particles prefer one of the two polymers, which means that they are preferentially included in that polymer. Karim et al. studied the effect of immobile filler particles on phase separation experimentally and computationally [134]. They find that the presence of filler particles leads to the formation of composition waves ('target patterns') around the particles, due to the preference of one of the polymers for the particles, during the intermediate stage of phase separation, which break up again as the background spinodal phase-separation pattern becomes much larger than the filler particles, see Fig. 5.2. Experiments by Chung et al. on mobile nanoparticles in phase-separating

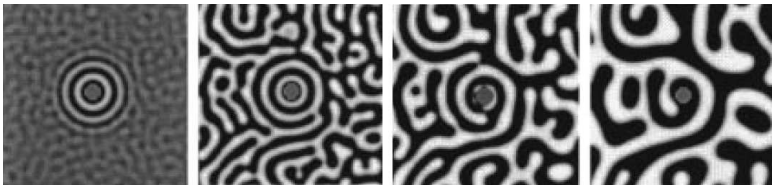

Figure 5.2: Illustration of the formation of 'target patterns' around filler particles in a polymer blend. It is crucial that there is preference of one of the polymers for the filler particles. The 'target patterns' break up as the spinodal phase-separation pattern coarsens to a scale much larger than the filler particle. This illustration is the computational result obtained by Karim et al. [134].

thin-film polymer blend show that the nanoparticles partition into their preferred phase which enhances the viscosity of that phase [135]. The domain growth is found to be slowing down upon addition of nanoparticles, which is in agreement with the findings of Laradji et al. obtained via computer simulation [120]. They find that the addition of nanospheres that preferentially interact with one of the two fluids leads to slower domain growth as the volume fraction is increased. Tang et al. found in their simulations

that depending on the particle concentration the phase favoured by the particles can organize into cluster, interconnected or network structures [136]. The formation of 'target patterns' around particles in the early stage of phase separation of a near critical polymer blend [134] is found in simulations [137]. The existence of a preference of one of the polymers for the particles is key. These 'target patterns' diminish when the spinodal phase-separation patterns become larger than the particles.

Numerical simulations performed by Tanaka and Araki of a phase-separating binary liquid near a solid wall preferred by one of the two liquids show that composition waves develop near the wall in early stage of spinodal decomposition [138]. Soon after, a wetting layer of the preferred phase forms on the solid surface which thickens in later stage via fluid tubes in which flow is directed from the bulk towards the wetting layer. These simulations were extended to study the effect of particles in a binary mixture numerically; Tanaka et al. found in simulations that in the early stage of phase separation, spinodal decomposition induces 'target patterns' around the particles due to wetting effects, the particles prefer one of the two polymers [139]. In their study of the effect of mobile and immobile particles on the pattern evolution of a phase-separating polymer blend film, they found that the formation of 'target patterns' is crucial for what the final domain morphology will be like. When one of the phases has covered the particle surface a depleted region around it is induced as a result of diffusion. The particles approach each other after the formation of the depleted region, which indicates that it gives an attractive interaction between the particles. The authors call this unconventional attractive interaction 'wetting-induced depletion attraction', which has been studied in more detail by the authors more recently [140].

Not only phase separation but also other external fields can induce effects that influence the arrangement of colloids in a system. Löwen et al. have studied the formation of lanes in colloidal mixtures driven by an external field computationally [141–145] and experimentally [141]. The system consists of a binary colloidal mixture of oppositely charged colloids, exposed to an external electric field. One half of the colloids is pushed into the direction of the applied electrical field, whilst the other half is pushed into the opposite direction, which causes the colloids to form lanes. When the applied field is stronger the formation of colloidal lanes, in which the colloids have the same charge, becomes more pronounced. In ref. [146] the formation of lanes of small (uncharged) particles injected into a stationary cloud of big (uncharged) particles is studied experimentally and computationally. Here the driving force is the velocity of the smaller particles, which means that the big and small particles have different velocities. After injection of small particles into the cloud of big particles, initially the big particles are pushed by the small particles collectively, after which the small particles form lanes when penetrating the cloud of big particles. The small particles

are more likely to move through regions with the least resistance, which results in the formation of lanes by the particles. The larger particles will arrange in lanes such that the small particles can penetrate in that region. Phase separation in the PMMA-microemulsion composite leads to a series of regimes of different dynamic character. Creaming and sedimentation always play an important role. Here we will explore the different regimes in turn.

5.2 Experimental methods

Materials The poly(methyl methacrylate) (PMMA) colloids used in the experiments presented in this chapter were from the same batch that was used for experiments in chapter 4. The details are described on p. 61 in chapter 4.

Phase behaviour Phase behaviour was studied using bright-field optical microscopy (Olympus BX50) and confocal fluorescence microscopy (Nikon E800 Eclipse) under controlled temperature. A temperature stage (Linkam) was used with which the temperature could be varied at a 0.1^oC/minute rate or faster. The samples are studied in glass cuvettes (Starna) which were cleaned (Decon) and dried (at 60^o for at least 5 hours) carefully prior to use. Samples were transferred into the cuvettes with a pasteur pipette. Immediately before studying the sample it was mixed vigorously because the colloids sediment in time. The experiments in this chapter concern the late stages in the phase-separation process. To minimize the disturbance to the measurements due to sedimentation of the colloids, the system was brought to the phase-separation temperature at a rate of 1^oC/minute, and from that point the temperature was raised at a rate of 0.1^oC/minute.

Fluorescence studies To study the microemulsion behaviour in greater detail, confocal fluorescence microscopy was used, using the Biorad system E800. The experimental system used is exactly the same as that used in chapter 4, described on p. 61.

Digital Image Analysis / Processing Techniques used for enhancing image quality for better visualization are the same that were used for the data described in chapter 4). For images presented in this chapter contrast enhancement was used, which is described on p. 63.

5.3 Off-critical high-micelle concentration regime: Late stage

The microemulsion system in the off-critical high-micelle regime consists of $68\%_w$ dodecane. After dispersion of the colloids in the prepared microemulsion, microscopy studies were performed. The system is warmed up to induce phase separation, which occurs when the binodal is crossed. When the binodal is being crossed the micellar

gas phase nucleates around the colloids as has been described in the previous chapter. The colloids end up in the micellar gas droplets that are dispersed inside the micellar liquid phase, see Fig. 5.3 for an example. After crossing the binodal the nucleated

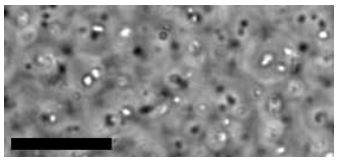

Figure 5.3: Here micellar gas phase has nucleated around the PMMA colloids after crossing the binodal, so that the colloids are entrained in micellar gas phase droplets. (Pure microemulsion composition: dodecane: 68%, pentanol: 15.8%, w/s: 16.2%). The scalebar represents 50 μm.

droplets containing colloids coalesce further up till a late stage point that large droplets are formed. Only those droplets containing many particles remain at an accessible depth in the sample. Those with few particles quickly cream to the top of the sample cell. Coalescence then occurs between these particle-rich droplets. Curiously, at this

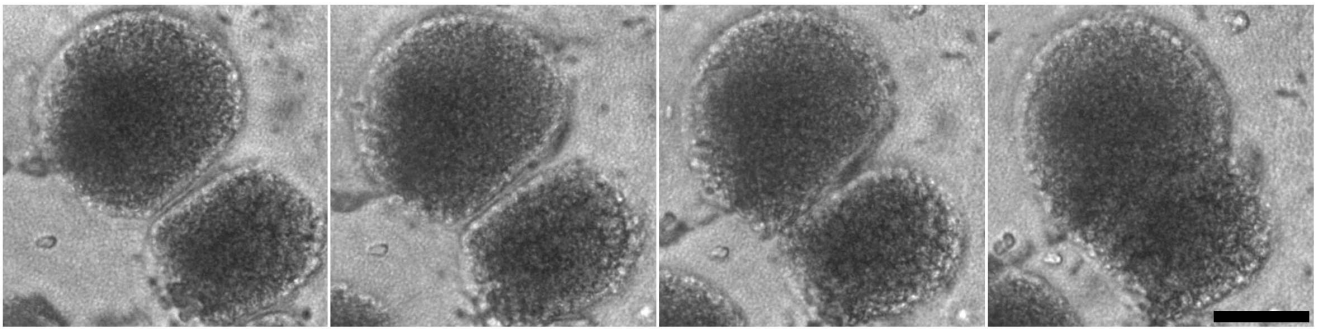

Figure 5.4: The droplets are pressed together before they start to coalesce. The time between the images is approximately 12 seconds. (Note that colloids fall out of the droplets whilst these are rising, this will be discussed further in the text). (Pure microemulsion composition: dodecane: 68%, pentanol: 15.8%, w/s: 16.2%). The scalebar represents 100 μm.

late stage the coalescence only proceeds very slowly, and even when the droplets are pressed together they do not coalesce immediately, as shown in Fig. 5.4. The slowness of the coalescence and the flat regions on each droplet are the notable features of this sequence of images. Tanaka also observed reluctant coalescence in his 'moving droplet phase' [147]. It is possible that the difficulty of deforming a droplet packed with particles adds to its stability.

In the system colloids are not observed to be located on interfaces during phase separation at any stage. This is in contrast to some liquid-liquid systems with high interfacial tension, where the colloids are observed to be trapped on the interfaces [109, 148]. Colloids can become trapped on an interface if the interfacial tension is sufficiently high and the particles have appropriate surface chemistry. This will lead

to a reduction in the free energy as the interfacial area between the two liquids is reduced [148]. When the interfacial tension is low, there will be hardly gain in free energy from colloids sitting on interfaces so this will be unlikely. This is the case for the system studied here, the interfacial tension between the micellar gas and micellar liquid phase is very low, on the order of $\sim 10^{-2}$mN/m [9].

It was observed that the droplets can sit squeezed against each other for up to 3-4 minutes without the film between them breaking up, see Fig. 5.4. When the droplets finally coalesce, it can be seen that a bridge between the droplets forms through which droplet material can flow so that the droplets can merge. The bridge becomes wider after it has formed and coalescence can occur easily once there is a connection between the droplets.

It is striking that at late stage the coalescence between droplets becomes more limited, whilst in early stage the micellar gas droplets coalesce upon touching. This change indicates that after nucleation of the micellar gas there is still material exchange between the micellar gas and liquid phases. When the temperature increases the gas and liquid compositions become more different from each other, see Fig. 4.10 on p. 77. The deeper the quench, the more different the phases are. The micellar liquid, the continuous phase in which the micellar gas droplets are dispersed, is the most rich in micelles. This means that when two micellar gas droplets are approaching each other micelles need to move out of the way for these droplets to contact. This could be a reason for the limited coalescence. To investigate this possibility confocal fluorescence microscopy was used. Both the PMMA colloids and the micelles are fluorescently labelled. The micelles are fluorescently labeled with oxazin 170 perchlorate, so that they could be imaged separately from the colloids that are fluorescently labeled with NBD. The aim of these experiments is to find out if there are micelles trapped in between the large droplets prior to coalescence. In Fig. 5.5 different modes of imaging of the same sample are shown. In the image on the left only the PMMA colloids are visible, here can be seen that the PMMA colloids are mainly located inside the micellar gas droplets (the micelle poor phase) and not in the micelle rich (liquid) phase in which the droplets are dispersed. In the middle image the micelles are imaged, the majority of the micelles are located in the continuous phase in which the formed droplets are now dispersed. It can be seen that between the two droplets there is micellar liquid phase present, preventing the coalescence between the droplets. When two bubbles in a liquid approach each other a thin liquid film is formed between them and this will drain with time [128]. The rate of coalescence between bubbles depends on the rate at which the liquid drains from the film. Coalescence can be slowed down by the viscosity of the surrounding liquid [129]. After draining the film between the droplets has to breakup for the droplets to be able to merge. The interfaces are in constant motion, and when

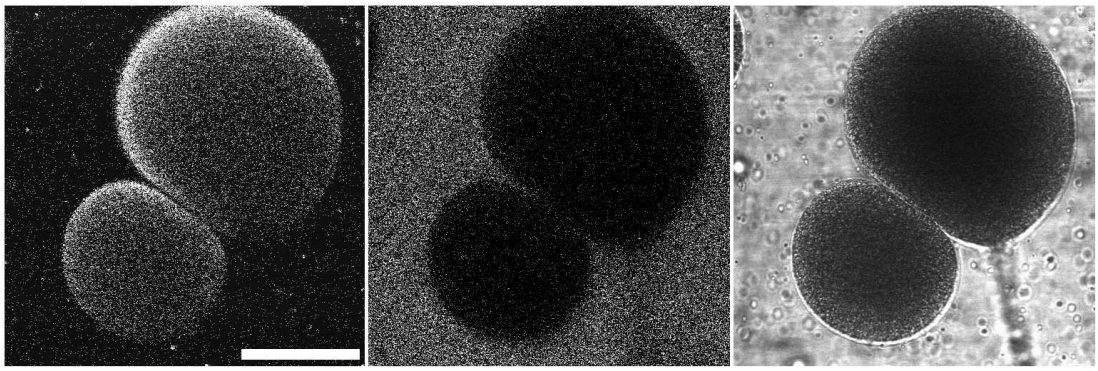

Figure 5.5: Confocal images of droplets in the late stage of phase separation. The droplets are pressed together for long times before coalescing. In the first image (left) the PMMA colloids are imaged, in the middle image the micelles are images, and the third image is a bright-field image of the same droplets. (Note again that colloids fall out of the droplet whilst it is rising, see text for discussion). (Pure microemulsion composition: dodecane: 68%, pentanol: 15.8%, w/s: 16.2%). The scalebar represents 100 μm.

two opposite bulges at the two interfaces meet, the two droplets can merge [130]. The droplets are squeezed together before coalescence actually starts to happen. This can result from a changed the interfacial tension between the micellar gas and micellar liquid phase, compared to early stages in phase separation. A higher interfacial tension makes it harder for a surface to stretch and thus move, which causes a delay to coalescence. Also, the observed behaviour can be caused by the medium surrounding the droplets, the micellar liquid phase. In the system the draining of micellar liquid phase is slow, this is because for the droplets to be able to coalesce with each other the micellar liquid first need to move out of the way. Further slowing of coalescence is likely to be due to the difficulty of deforming a droplet packed with particles.

In the images shown to illustrate the coalescence of the micellar gas phase droplets at the late-stage of phase separation, it was noted that colloids entrained inside the droplets fall out of it (Fig. 5.4). Because the micellar gas phase has a lower density than the micellar liquid phase, the gas phase droplets will rise to the top of the sample with clustered colloids entrained. Some of the colloids, due to their higher density, fall out of the droplet while it is moving (buoyancy) giving the appearance of colloidal comets, see Fig. 5.6. The fact that the colloids easily fall out of the cluster inside the micellar gas phase droplet indicates that the colloids are loosely bound to each other. This figure shows comets at a later stage then those shown in Figs. 5.4 and 5.5, in which only a few colloids are falling out of the droplets.

The interfacial tension of the droplet is so low that it cannot provide a barrier high enough to prevent the colloids from leaving the droplet when it is moving. The interfacial tension between the micellar gas and liquid phase is very low ($\sim 10^{-2}$mN/m

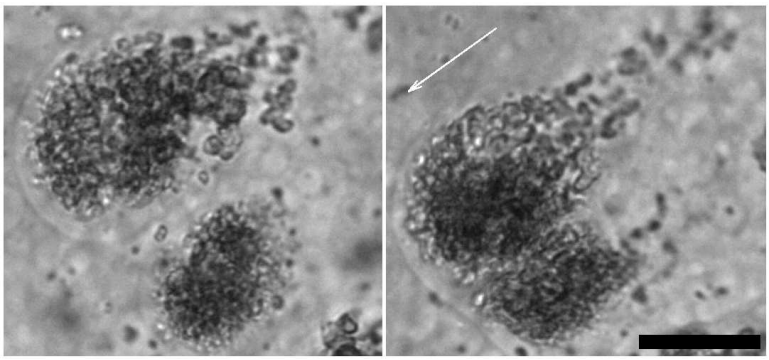

Figure 5.6: Micellar gas phase droplets are rising up because of their lower density. The colloids however have a higher density and can not keep up with the moving droplets, and fall out of the droplet. This indicates that the colloids are loosely bound. The colloids being left behind by the rising droplet has the appearance of a comet. The colloids can become more clustered at later stage when the droplet has risen sufficiently high in the sample, see text. Arrow indicates the upwards flow direction of the droplet. (Pure microemulsion composition: dodecane: 68%, pentanol: 15.8%, w/s: 16.2%). The scalebar represents 50 μm.

[9]) because of the size of the micelles and the similarity of the phases. Both the micellar gas and liquid phase are solutions of (reverse) micelles in dodecane, with the difference between them being the concentration (and size) of micelles. Even though the micellar gas and liquid phase are similar, the colloids prefer to remain in the micellar gas phase because of the presence of the micelles. Because of depletion interaction between the colloids and the micelles in the micellar liquid phase the colloids preferably remain in the micellar gas phase. As the droplet is rising it leaves colloids behind, but the majority of colloids remain in the droplet and end up at the top of the sample, where the bulk micellar gas phase forms. Because of buoyancy forces the colloids are left behind when the droplet is rising. This is illustrated in Fig. 5.7. The rising droplet

Figure 5.7: Buoyancy effect. Because the micellar gas phase has a lower density than the micellar liquid phase the droplets are rising. The colloids' density is higher and they are not able to keep up with the rising droplet and fall out of the droplet. The upward buoyancy force experienced by the droplet is equal to the weight of the micellar liquid displaced by it. The presence of colloids in the droplet makes its density effectively higher.

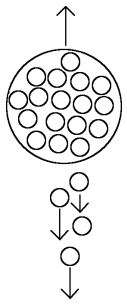

with colloids left behind has the appearance of a comet, Fig. 5.6. Eventually all micellar gas phase droplets rise to the top with the majority of colloids to form bulk gas phase, which means that in the more dense micellar liquid phase only a small proportion of dispersed colloids will have been left behind. None-the-less long after completing phase separation the colloids in both the micellar gas and liquid phases sediment under gravity

to the bottom of the sample container (which takes about 30-40 min), and both the top and bottom phase above the sediment appear transparent.

A similar instance of particles left behind by an advancing interface has been studied by West et al. in the context of particles at an isotropic to nematic phase transition [43]. Here the particles begin in the isotropic phase. A nematic interface advances towards them during the transition. If the particles finish in the nematic phase there is a size-dependent elastic energy cost - for the particles to, instead, be carried forwards by the interface there is inertia to overcome. In the liquid crystal there is a threshold size above which particles are left behind by the advancing interface. In our case the particles are being pulled down by gravity. This force will scale with the mass of the cluster of particles:

$$F_g = \frac{4}{3}\pi R^3 \Delta\rho g \tag{5.1}$$

where R is roughly the PMMA cluster size, $\Delta\rho$ is the density difference between the PMMA and the microemulsion. Countering this is the energy cost of the PMMA being left behind by the creaming droplet. Here the particle surface would be exposed to the unfavourable micellar liquid phase. This effect can be captured by the difference in surface energies of the interface:

$$F_\gamma = 2\pi(\gamma_L - \gamma_G)R \tag{5.2}$$

where γ_L is the interfacial tension for the PMMA-micellar liquid interface and γ_G is the interfacial tension for the PMMA-micellar gas interface. Where these two terms balance is the cluster size for which the surface cost just balances gravity:

$$R_{min} = \sqrt{\frac{3(\gamma_L - \gamma_G)}{2\Delta\rho g}}. \tag{5.3}$$

Particle clusters of a size greater than R_{min} will tend to be left behind. The trail of clusters make the tail of the comet.

5.4 Off-critical low-micelle concentration regime

The microemulsion system in the off-critical low-micelle concentration regime is prepared with $75\%_w$ dodecane, which means that the concentration of micelles here is lower than that of the microemulsion used in the previous section. In the studies presented here a colloidal weight fraction of $0.1\%_w$ was used. The PMMA colloids are dispersed in the microemulsion just before studying the system using microscopy techniques. In this composition regime it is the micellar liquid that nucleates out

when the temperature is raised. The pure microemulsion phase separates around 36^{o}C (see Table 4.1 and Fig. 4.2). The colloids, which remain in the micellar gas phase, are observed to hardly cluster whilst the micellar liquid phase nucleates in droplets. In this early stage the nucleated droplets coalesce when they approach and contact. Bright-field microscopy images of the early stage of phase separation are shown in Fig. 5.8, where it can be seen that the colloids remain in the micellar gas phase (continuous phase). Initially the micellar liquid droplets and colloids are homogeneously distributed

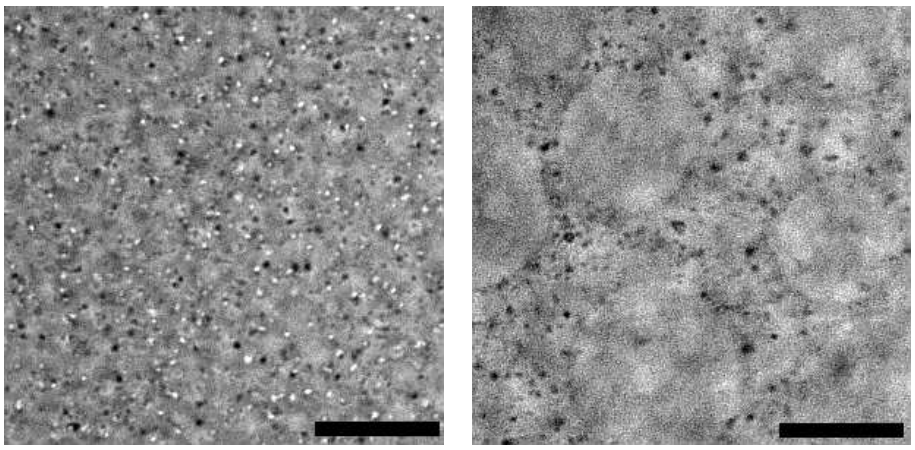

(a) (b)

Figure 5.8: The micellar liquid phase nucleates and the colloids remain in the micellar gas phase: (a) initial stage and (b) later stage ($\sim$ 70 seconds later than stage in (a)) when the micellar liquid droplets have grown and the PMMA colloids remain in the micellar liquid phase. Not much clustering of the colloids during phase separation is observed. (Pure microemulsion composition: dodecane: 72.25%, pentanol: 14.55%, w/s: 10.2%). Scale bars indicate 50 μm.

across the sample in the micellar gas phase as can be seen in Fig. 5.8. Later on 'laning' of the colloids and micellar liquid droplets is observed, see Fig. 5.9. During phase separation the colloids remain in the micellar gas phase whilst the micellar liquid phase nucleates at the bottom. The sample is heated slightly more from the bottom side, which means that there exists a temperature-gradient across the sample; at the bottom it is warmer than the top of the sample, and because of this there is convection. The warmer component will be pulled towards cooler areas. It is observed that the micellar liquid phase droplets and colloids remain at the bottom, but exhibit a sideways flow rather than upwards, along the direction of the colloid lanes that are visible in the microscopy image (Fig. 5.9). This is because the density of both the micellar liquid droplets and the colloids is higher than that of the micellar gas phase. The droplets and colloids are too heavy to be pulled up by the temperature-gradient induced upward flow. Because of this, flow sideways is observed rather than upwards. This is illustrated in Fig. 5.10. The formation of lanes by the colloids can be explained when it is considered

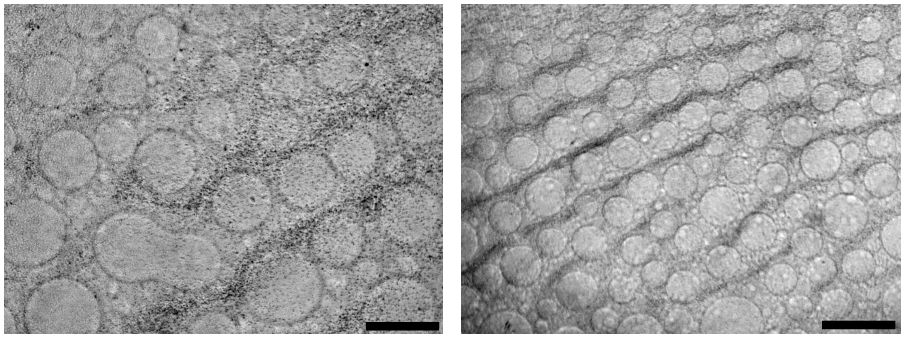

(a) (b)

Figure 5.9: Laning, these images are taken ∼4.5 minutes after the phase separation has started. (Pure microemulsion composition: dodecane: 72.25%, pentanol: 14.55%, w/s: 10.2%). Scale bars indicate 100 μm.

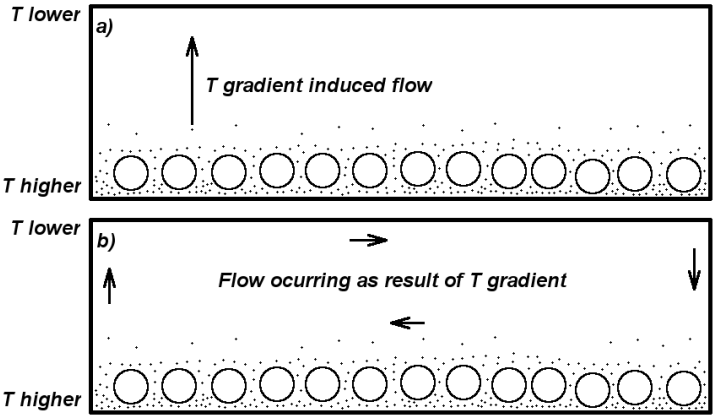

Figure 5.10: Schematic illustration showing how flow arises in the sample cell. (a) The cell is heated slightly more from the bottom, which creates a vertical temperature-gradient. The situation here is that observed 4-5 minutes after the start of phase separation (Fig. 5.9). The micellar liquid droplets (the circles) nucleated at the bottom of the cell and remain there because of their higher density than the micellar gas phase. At this stage some colloids (the small black dots) have sedimented. Since both the micellar liquid phase and the colloids have a higher density than the micellar gas phase they both remain at the bottom of the cell, despite the upwards flow induced by the temperature-gradient. (b) Only the micellar gas phase is pulled up under the influence of the temperature-gradient. This creates a circular flow in the sample as illustrated, which means that a sideways flow at the top and bottom of the cell is induced.

that there is flow occurring in the sample. The micellar gas phase is pulled up by the flow induced by the temperature-gradient, but the micellar liquid phase droplets and colloids are not pulled up because their density is higher than that of the micellar gas phase, which results in that sideways flow occurs (Fig. 5.10). Both the micellar liquid droplets and the colloids are now subject to sideways flow of the micellar gas phase. The colloids and the droplets both experience the same viscous drag induced by the flow. Because the droplets and the colloids have different sizes their velocity is different,

the colloids move faster than the droplets. This has the effect that lanes of colloids and lanes of droplets are formed because this enables both to move with the flow with reduced resistance (Fig. 5.9).

Here we discuss the late stage behaviour as the micellar liquid phase droplets coarsen. The micellar liquid droplets grow in time via coalescence and remain at the bottom of the sample due to their higher density compared to that of the micellar gas phase. At early stage the micellar liquid droplets coalesce on contact, whilst at later stage the coalescence becomes more hindered. This observation is similar to that observed in the off-critical high-micelle concentration regime discussed in the previous section, where also initially coalescence occurred upon touching in early stage, and became more hindered at late stage. At later stage some colloids have sedimented towards the bottom of the cell, where the micellar liquid phase droplets are as well, see the illustration in Fig. 5.10. The composition at the top and the bottom of the cell is not the same and this is very important. In time the micellar liquid droplets grow whilst the colloids remain in the micellar gas (the continuous phase), from which less and less is located at the bottom of the sample as this creams to the top of the sample. In the illustration in Fig. 5.10 this can be seen, the micellar gas phase has creamed to the top of the sample and the micellar liquid phase and the colloids are located at the bottom of the sample cell. At the bottom of the cell the micellar liquid phase has become the majority phase rather than the minority phase. In Fig. 5.11 the composition change that occurs at the bottom of the cell is illustrated schematically. This means that

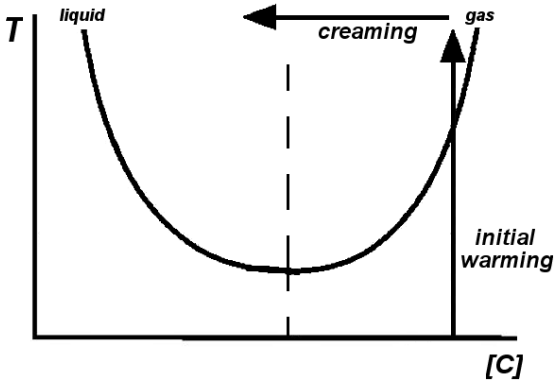

Figure 5.11: The creaming and sedimentation results in a *local* change in composition of the sample. The minority phase becomes the majority phase. This is the situation at the bottom of the cell, see Fig. 5.10.

the images appear as though there is much less gas phase. At this stage the micellar droplets have grown to such a size that they are squeezed to each other. Even though the micellar liquid droplets are touching they are not coalescing for long times and a network-like structure can form (Fig. 5.12). The droplets remained intact for long

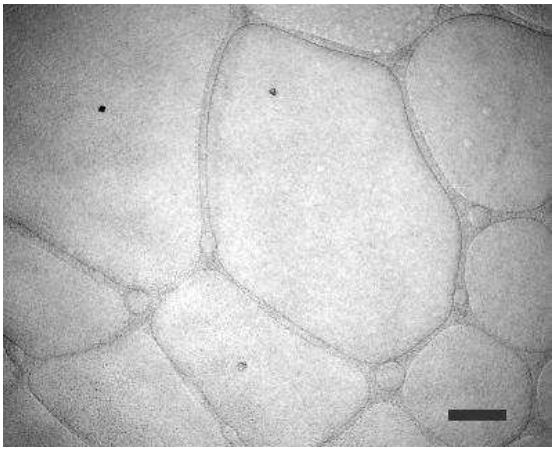

(a)

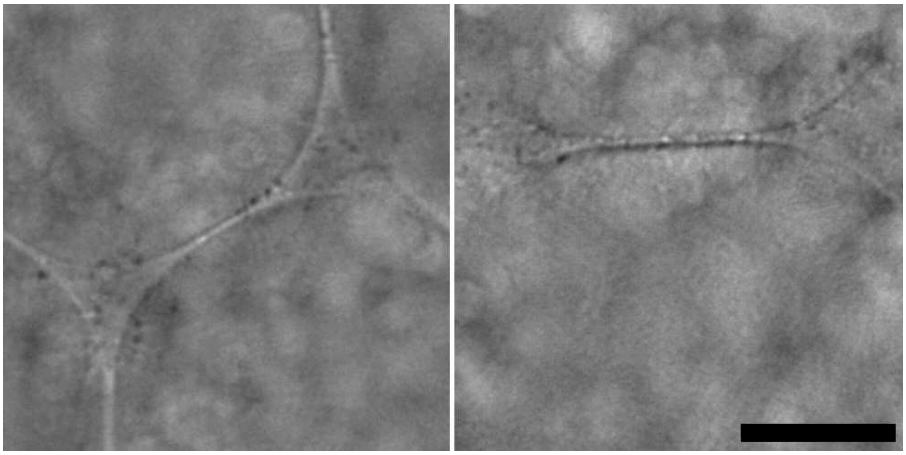

(b)

Figure 5.12: (a) Late stage of the phase separation, The micellar liquid droplets grow whilst the colloids remain in the micellar gas phase. The volume of micellar gas phase at the bottom decreases, as most of this phase rises to the top of the sample due to its lower density. The interfaces only deform slowly and network-like structures can exist for long times (scalebar indicates 100 μm). (b) The colloids are not found to be on the interfaces, but they can be squeezed in between two micellar liquid droplets whilst remaining in the micellar gas phase (scalebar indicates 50 μm). (Pure microemulsion composition: dodecane: 72.25%, pentanol: 14.55%, w/s: 10.2%).

times ($\sim$10 minutes), but at some stage the gas phase containing the colloids between the droplets becomes very thin, and eventually the interface breaks. The interfaces only moved slowly after breakage which is remarkable, see Fig. 5.13, where the slow movement of interfaces is indicated. Coalescence occurs only slowly and punctured interfaces are observed to have viscoelastic properties; it takes a long time (seconds) for the interfaces to retract after breakage. The pattern evolution morphologies observed here are different from that observed in normal fluid PS, see e.g. Fig. 4.3 on p. 65.

The results obtained here in the off-critical low-micelle concentration regime in the

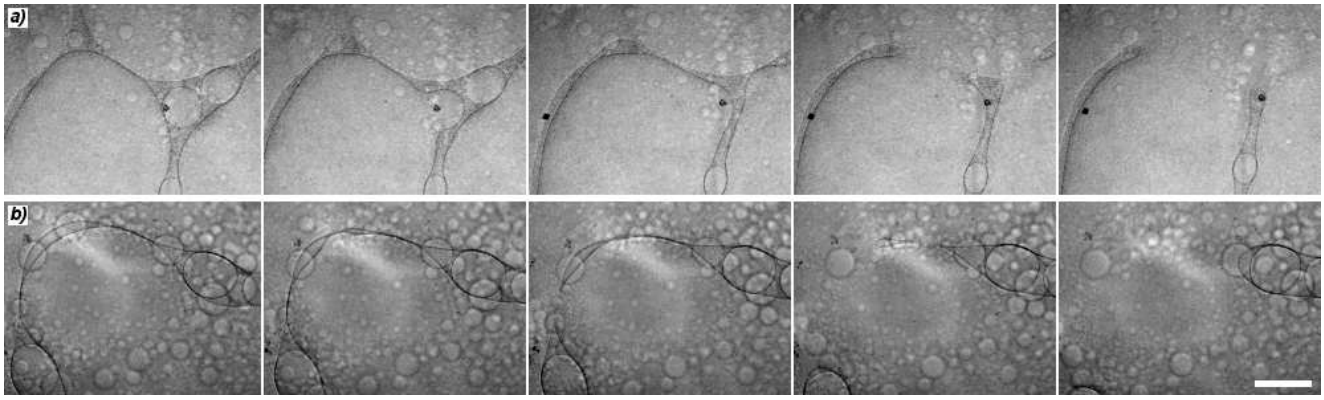

Figure 5.13: The colloids are entrained within the micellar gas phase. The interfaces are changing and rupturing slowly. In these examples the time between subsequent images is 2 seconds (scalebar indicates 100 μm). The two sequences in (a) and (b) represent different parts of the sample. (Pure microemulsion composition: dodecane: 72.25%, pentanol: 14.55%, w/s: 10.2%).

late stage of phase separation are different from standard nucleation and growth. In later stage coalescence does not occur as easily, droplets are squeezed together for long times (∼10 minutes) before merging. Once a bridge has formed between two micellar liquid droplets the movement of the interfaces is slow, because for the droplets to merge the surrounding micellar gas phase, containing the colloids, has to move away. The results obtained in the off-critical low-micelle concentration regime fit in Tanaka's description of viscoelastic phase separation albeit with a crucial role played by sedimentation. Initially the micellar liquid phase nucleates, after which the micellar gas phase decreases in volume (especially locally at the bottom due to sedimentation effects), which leads to the formation of a network-like pattern. Eventually the network-like pattern breaks up in the last stage of the phase separation. In the system under study the colloids make the micellar gas phase viscous, and after phase separation has started there is still material exchange. Because the continuous phase (gas) is slow, the phase separation evolution is affected which results in a changed morphology, a network is formed by the slow component, which is different than the usual nucleation and growth morphology in binary-liquid phase separation.

5.5 Conclusions

In the phase separation of the high-micelle concentration samples the appearance of comets was observed, rising droplets that leave colloids behind because of buoyancy. It is important to note here is that this indicates that the colloids are only loosely bound. In the late stage of phase separation inhibited coalescence of micellar gas droplets was observed. The concentration of colloids entrained in the micellar gas droplets is high.

In the low-micelle concentration regime the micellar liquid phase nucleates in droplets upon warming, and the colloids remain in the micellar gas phase. Because of the presence of flow (induced by a temperature-gradient) the colloids and micellar liquid droplets are observed to arrange themselves in lanes, which is illustrated in Fig. 5.10. The late stage of the phase separation in the low-micelle concentration regime was characterized by a different morphology than that observed in standard nucleation and growth. The system shows the formation of a network, formed by the micellar gas phase with the colloids entrained. The micellar liquid droplets exhibit very slow coalescence in this stage.

The experiments performed both in the high- and low-micelle concentration regimes show interesting late-stage behaviour. After crossing the binodal initially coalescence between nucleated droplets occurs when the droplets contact, in both concentration regimes, whilst at the late stage, when the temperature is higher, the coalescence becomes hindered. After phase separation has started there is still material exchange between the phases. From the schematic in Fig. 5.14 it can be understood that at increased temperature after crossing the binodal the compositions are different than at somewhat lower temperature. When the temperature is higher (T_2) the compositions

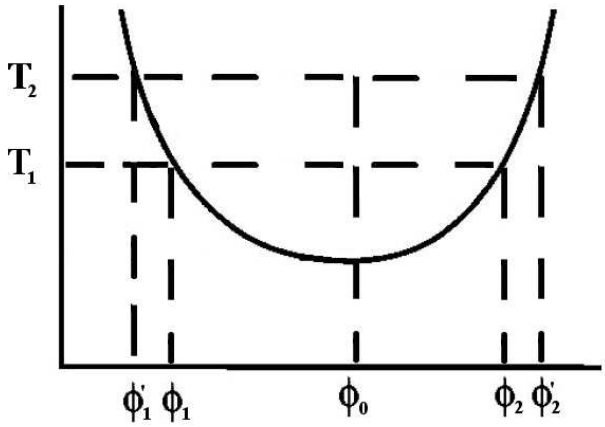

Figure 5.14: Schematic phase diagram in which it is shown how the compositions of the phases ϕ_1 and ϕ_2 change when the temperature is raised some after phase separation has already taken place. On warming the compositions of the phases move further apart and become more different from each other in composition. The phases with compositions ϕ_1' and ϕ_2' are more different from each other in composition than ϕ_1 and ϕ_2.

of the phases move more apart, and as a result from the material exchange the interfacial tension γ between the micellar gas and liquid phase becomes somewhat higher. Because the phases become more different from each other due to material exchange, the properties can change which affects the pattern evolution during further phase separation. This is observed to be true in the experiments performed, both for the high- and low-micelle concentration regimes. Initially when phase separation is induced

via warming the nucleated droplets easily coalesce with each other when they meet, which is true for both micellar concentration regimes. Later when the temperature is higher, and more material exchange has taken place, the coalescence becomes more hindered. The droplets do not coalesce upon touching, even when they are squeezed together for long times. This is true for both micellar concentration regimes.

In the high-micelle concentration regime, the micellar liquid phase surrounding the micellar gas phase droplets (that contain the colloids) increases in volume after material exchange. It can be seen from the schematic in Fig. 5.14 that the micellar gas phase decreases in volume after material exchange, which effectively increases the colloid concentration in this phase. In this concentration regime the coalescence of the micellar gas droplets containing the colloids becomes hindered after material exchange has taken place. The droplets are pressed together for long times (up to 3-4 minutes) before they coalesce. This behaviour is reminiscent of the 'moving droplet phase' observed by Tanaka [147]. In this picture the droplet behaves as an elastic body, and the system is dynamically stable and coalescence is prohibited. This scenario can explain the observed behaviour in the PMMA-microemulsion system. The high concentration of colloids in the droplets make the droplet viscoelastic. The elastic behaviour of the micellar gas phase droplets provides a barrier for coalescence.

The morphology in the low-micelle concentration regime appears quite differently, at late stage a network structure is formed. In this concentration regime the micellar gas phase (containing the colloids) is the continuous phase. The presence of the colloids make the micellar gas phase more viscoelastic, which makes the drainage of the micellar gas phase from the region in between micellar liquid droplets very slow, because also the colloids have to move away from this region (see the image sequence in Fig. 5.13). The effect of creaming and sedimentation is schematically illustrated in Fig. 5.15. The concentration of colloids in the micellar gas phase is increased locally, at the bottom of the cell, giving the micellar gas phase viscoelastic properties. The micellar gas phase morphology resembles that of a network in the late stage, as can be seen in Fig. 5.12(a). Because of the presence of the colloids the micellar gas phase starts to behave more as an elastic material and provides a barrier against coalescence between the micellar liquid droplets.

For the PMMA-microemulsion system this slowing down is the closest the particles come to resisting manipulation by the host system. In the next chapter we explore a system where the particles are much more strongly attractive.

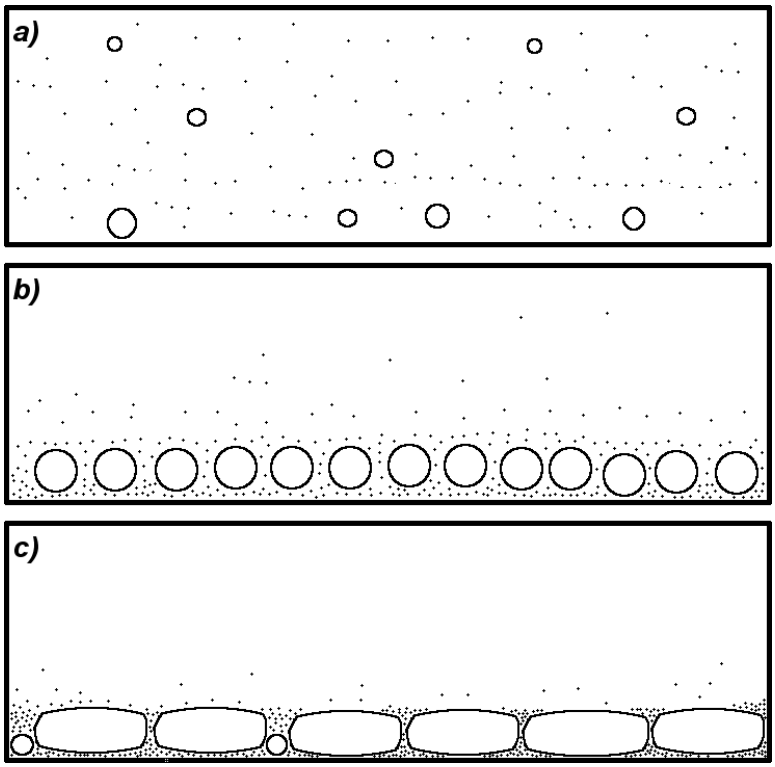

Figure 5.15: Schematic of the creaming and sedimentation effect during the phase separation. (a) Phase separation is induced via increasing the temperature and micellar liquid droplets nucleate. (b) Both the micellar liquid droplets and PMMA colloids are more dense than the micellar gas phase, which means that they sediment. At this later stage the micellar liquid droplets have grown somewhat. (c) The late stage where the network like structure is apparent. The micellar liquid droplets located at the bottom of the cell have grown and are pressed against each other. The locally increased concentration of colloids entrained in the micellar gas phase give this phase viscoelastic properties.

Chapter 6

Structure and properties of 5CB-silica composite

The second system examined in this thesis is comprised of particles with attractive interactions in a liquid crystalline host. In this chapter we carry out initial characterization of structural and bulk properties. The internal structure of the gel formed by the silica in the 5CB is investigated with electron microscopy techniques. Rheology is used to further examine the composite's properties when subjected to controlled perturbation. This structural investigation informs the study of the local dynamics in the next chapter.

6.1 Introduction

The aggregation behaviour of attractive colloids has been studied in some detail. Here we look at what happens in an anisotropic solvent.

The structure of agglomerates in an isotropic solvent relates to the strength of the interactions between the particles [2]. When the attractions between particles is larger than a few k_BT it becomes harder for particles to unstick from each other once they are in contact. When particles are able to rearrange the resulting aggregate is likely to be rather compact. When the attraction between the particles is too strong for the particle to be able to rearrange, the resulting aggregate will have a more open structure which is fractal. For a compact object the relation between the size R and mass M can be written as $R \sim M^{\frac{1}{3}}$, while for a fractal the relation is as follows: $R \sim M^{\frac{1}{d_f}}$, where d_f is the fractal dimension ($1<d_f<3$).

The structure of aggregates in solution is the result of how the aggregation is controlled, in the sense that the aggregation is diffusion or reaction limited [149]. Using light scattering techniques for studying various systems Lin et al. demonstrated that the observed aggregation regimes are universal. In Fig. 6.1 an example from ref. [149] is shown to illustrate the character of the different structures. When the aggregation is diffusion limited the structure has a more open character ($d_f = 1.8$) compared to when it is reaction limited and is more compact ($d_f = 2.1$). For diffusion limited aggregation

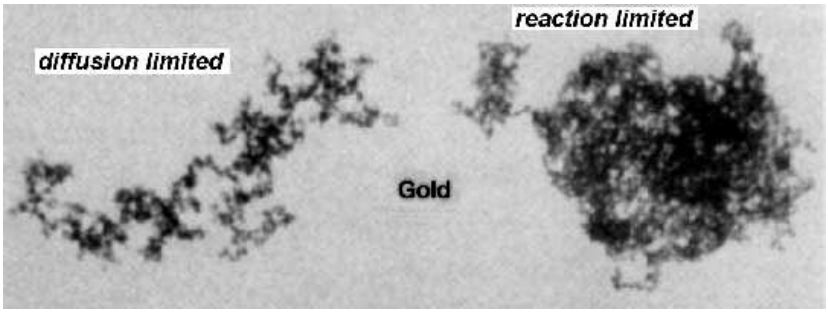

Figure 6.1: Example of the different types of aggregates [149]. The aggregates consist of 15nm diameter gold nanoparticles, that are formed under different conditions. The structure on the left is formed under conditions where the aggregation is diffusion limited. The more compact structure on the right is formed under conditions where the aggregation is reaction limited.

the aggregation rate is limited by the time it takes for clusters to meet each other by diffusion. In reaction limited aggregation the rate of aggregation is limited by the time taken for two clusters to overcome the repulsive force by thermal motion. The structures for these two regimes are distinct from each other and the behaviour, determined by the height of the repulsive barrier between the particles, is found to be universal. The silica nanoparticles used in the project are embedded in an anisotropic host rather than an isotropic one. Studying the fractal dimension will be instructive about the aggregation behaviour of silica in an anisotropic environment.

An early structural investigation of hydrophilic silica and 8CB composites using small angle x-ray scattering (SAXS) showed that the silica assumes a fractal structure [150] consisting of several levels experimentally accessible; primary particle, aggregate, agglomerate. In this study the important result is that the silica structure consists of several levels, experimentally accessible with SAXS. For analyzing the observed scattering the unified approach is used, where each structural level is modeled by two terms, one for the Guinier region and one for the higher q power-law region [151]:

$$\begin{aligned} I(q) \;\cong\; & \sum_{i=1}^{n} \Big\{ G_i \exp(-q^2 R_{gi}^2/3) + \\ & B_i \exp(-q^2 R_{g(i+1)}^2/3) \times \Big\{ [\mathrm{erf}(qR_{gi}/\sqrt{6})]^3/q \Big\}^{d_{f_i}} \Big\}, \end{aligned} \tag{6.1}$$

where n refers to the largest structural level and d_{f_i} is the ith level power-law exponent.

Analysis indicates that primary particles form fractal aggregates, which in turn form agglomerates. The analysis could be used to estimate the sizes of the primary particles and aggregates, but for the agglomerate data at much lower q would have been needed. Different sample preparations were used in order to determine its effect on the final silica structure. Some samples were prepared using the 'solvent-evaporation technique',

others were prepared using mechanical mixing or sonication. In the solvent evaporation technique dispersion of the nanoparticles is promoted using an added volatile solvent, which is vaporized after the constituents are well mixed to leave a mixture of the nanoparticles and liquid crystal. The results are compared with those for a collapsed dry gel prepared using the solvent-evaporation technique, and with those for a dry gel not exposed to any solvents. The higher the silica particle concentration in the composite, the more the gel structure resembles that of a collapsed gel. For low silica densities structures with a fractal dimension of $d_f = 2.0$ were identified, and when the silica density was increased above ρ_s=0.1 g/cm^3 the fractal dimension was observed to decrease, suggesting a partial collapse of the aggregate. The silica structure is found to be essentially independent of temperature and thus of 8CB phase (SmA, N, I).

The structural properties of soft materials including not only gels, but also foams, emulsions and colloidal pastes, can be studied using rheology. When low stresses are applied these materials tend to behave as a weak elastic solid and flow like a viscous liquid when stresses higher than the yield stress are applied. The observed glassy dynamics in many soft materials originate from structural disorder and metastability [152]. For systems to achieve structural relaxation via rearrangements energy barriers large compared to thermal energies need to be crossed. This means that the system exists in a disordered metastable state. In a study performed on a microgel paste history-dependent effects were found using rheology with a cone-plate geometry [153]. The sample's response depends on the waiting time after mechanical preparation in which the sample is rejuvenated via applying a stress larger than the yield stress for 60s and thus fluidized. When the preparation stress is removed the macroscopic flow stops and the microgel is trapped in a metastable state, the spatial arrangement is like that in the fluidized paste. The microgel then relaxes over time, and the measured response depends on the waiting time, at which only configurations with relaxation times smaller than the waiting time will have relaxed.

The rheological behaviour of 8CB confined in a colloidal aerosil gel has been studied as a function of temperature in a cone-plate geometry [154]. The presence of the silica particles introduces quenched disorder in the liquid crystal. The authors find that the presence of the silica nanoparticles significantly increases the shear modulus compared to the pure 8CB in the smectic phase. In the nematic or isotropic phase the modulus is controlled by the elastic behaviour of the colloidal gel. However, the observed growth of G*(ω), the complex modulus, in the smectic phase is attributed to contributions from smectic defects. The composite's dynamics in the smectic phase become increasingly glassy upon increasing silica concentration.

Based on all of these finding I am going to investigate the structure of the composite silica-5CB. Questions to be answered are: What type of aggregates are formed by the

silica nanoparticles while embedded in 5CB? How does this change the bulk rheology of 5CB?

6.2 Experimental system

In the experiments the liquid crystal (LC) used is 5CB (CAS 40817-08-1, 4-cyano-4'-pentylbiphenyl), a thermotropic liquid crystal exhibiting an isotropic to nematic phase transition at around 35^{o}C. In the nematic phase and isotropic liquid the 5CB molecules are associated, forming dimers due to dipole-dipole interaction [155]. In the nematic phase there is orientational long-range order. Fumed silica (SiO_2) particles (Wacker) are used, particles with a smooth surface that is not microporous [156]. In the particle synthesis the primary particles (5-30nm) fuse together permanently to form large units or aggregates (100-1000 nm in size).

6.2.1 Sample preparation

The fumed silica (wacker) and 5CB were mixed together in a glass vial by means of an ultrasonic probe (Sonics & Materials, 18 Watt) combined with using magnetic stirring to help disperse the particles in the 5CB. The batch of particles used here have 42% of the surface covered in silanol (-OH) group while the remaining surface area is covered in methyl groups (-CH_3). The silica particles and 5CB were weighed out at room temperature, such that the particles have a concentration of 1%$_v$ (corresponding to a silica concentration of $\rho_s = 0.02 g/cm^3$), and the composite is named 1/42 ((%$_v$ silica in 5CB)/(% silanol groups on silica)). It is easier to disperse the particles when the 5CB is in the isotropic state and thus less viscous compared to when it is in the nematic phase. For this reason the vials were placed in a water bath which is temperature controlled between 50-55^{o}C while the composites are mixed for 6.5 hours. In the TEM-experiments, after the mixing procedure, the composite was brought into contact with TEM grids. The TEM (LEO EM 912 Omega) is operated at 120 kV, and for the acquisition of the electron micrographs a cooled 1024 x 1024 CCD camera (Proscan, Germering, Germany) was used. The camera was controlled using SIS-image analysis software, version 2.1 (SIS, Münster, Germany). The electron microscopy experiments were carried out by Dr. L. Belkoura.

6.3 Static x-ray scattering

The silica-5CB composite was studied using scattering methods to obtain initial structural information. This formed part of a larger x-ray study described in the next

chapter. In small angle x-ray scattering (SAXS) experiments the scattered intensity $I(q)$ is measured as a function of the magnitude of the wave vector q. SAXS experiments were performed for several composites containing silica with varying surface properties leading to varying hydrophobicity. Composites containing silica with 100%, 42% and 32% silanol groups on its surface were studied, and the remaining surface area of the silica particles is covered in methyl groups. The composite name RT-2-100 indicates that the measurement is performed at room temperature (RT), and that the composite contains $2\%_v$ silica ($\rho_s = 0.04 g/cm^3$) that has 100% silanol groups on its surface. In Fig. 6.2 the structure factor for the four studied composites are presented. The

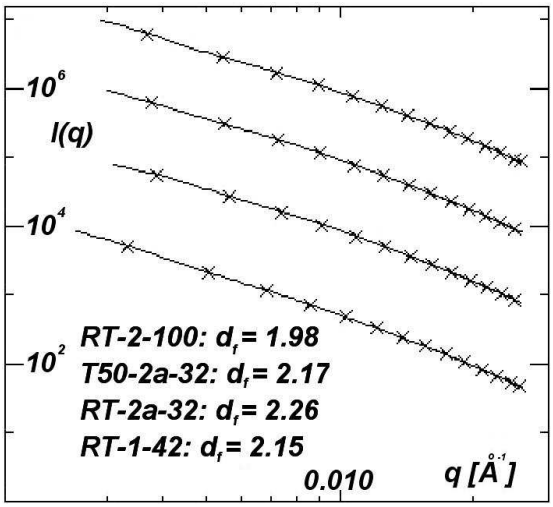

Figure 6.2: Structure factors from four composites that are studied in this and the next chapter, with the fractal dimension indicated for each composite. The crosses represent data, and the solid line is the fitted data. In the T50-2a-32 composite the 5CB is in the isotropic phase (T = 50°C). The 5CB is in the isotropic phase in the other three composites (T = RT).

intensity $I(q)$ is plotted as a function of q on a log-log scale. The curves are not perfect straight lines, but there is a slight bend. The shape of these curves can be described by eq. 6.1, from which the fractal dimension can be deduced [151]. The curves all have more or less the same shape in the q-range studied, indicating that in all the composites the particles are organized in a fractal manner. This is in agreement with the results obtained in the electron microscopy experiments. The q-range studied in the experiments is limited compared to those performed in ref. [150]. In their data a larger range of q was studied, allowing the authors to determine different hierarchical structures; the primary particles, aggregates and agglomerates. In the data presented in Fig. 6.2 only evidence of the structure of the aggregates is accessible (q varies from 0.003 to $0.03 Å^{-1}$). The sizes probed can be found via $d = \frac{2\pi}{q}$, which tells us that sizes between 20nm and 200nm are probed. It is shown here that the silica adopts a

fractal structure in 5CB, and in section 6.5 it will be demonstrated that this gives the composite gel-like properties. The following section deals with the study of structure of the composite using electron microscopy.

6.4 Electron microscopy investigation

Two methods of using freeze-fracture electron microscopy have been used to investigate the structure of the liquid-crystal composites, freeze-fracture electron microscopy (FFEM) and freeze-fracture direct imaging (FFDI) [61]. In these two techniques the preparation of the grids is different, as described in chapter 3 on p. 39. In this procedure, after the grids are prepared, they are assembled into a 'sandwich'. The sandwich is inserted in the composite while this is in the isotropic phase, above the isotropic-nematic (IN) transition. Initially the composite is allowed to penetrate well into the sandwich. After this the sandwich is held still and the temperature is lowered to below the IN transition (34.6^{o}C). The composite is first left to equilibrate, and afterwards the sandwich is rapidly transferred ('plunged') into the cryogen (liquid ethane).

The silica-5CB mixture was prepared several days before the start of the experiment. At the EM facility for preparing the grids the composite was brought into the isotropic (less viscous) phase by introducing the vial in a temperature controlled water bath at 50^{o}C. Inserting the sandwich into the composite when in the isotropic phase rather than the nematic, allows the material to penetrate between the assembled grids better. The open sandwich is inserted very slowly in the composite whilst in the isotropic phase and closed very slowly. The composite at room temperature is in the nematic phase and more viscous compared to the isotropic phase, such that the material would not be able to penetrate in between the grids. In Fig. 6.3 photos of the sample preparation are shown. The sandwich is placed with tweezers in the 5CB-silica composite for 30 minutes to allow the material to penetrate in between the grids assembled in the sandwich. After 30 minutes the water is allowed to cool down to 20^{o}C, a temperature at which the 5CB in the composite will be in the nematic phase. In the photos in Fig. 6.3 it can be seen that the transparency of the composite changes with temperature, indicating in which phase the composite is, isotropic (less opaque) or nematic (more opaque).

First results from the investigations from grids prepared at 20^{o}C (nematic phase) are presented. Subsequently a more limited data set taken when quenching from higher temperature are shown.

Figure 6.3: The preparation of the grid for measurements in the nematic phase. The tube is placed in a temperature controlled water bath. The composite is cooled from 50^{o}C to 20^{o}C. This is shown in the photographs from left to right. On the left the liquid crystal (5CB) is in the isotropic phase, and upon cooling it is brought into the nematic phase.

6.4.1 5CB-silica composite structure at T=20^{o}C

The composite which was prepared at 20^{o}C was studied using FFEM as well as FFDI.

FFEM In brief, in FFEM, the procedure consists of three steps; the preparation and freezing of the sandwich, its fracture and replication (shadowing), and the investigation of the replica with the TEM. The sandwich is 'plunged' into liquid ethane using a device (spring-propelled plunging rod [61]), so that this happens as fast as possible. In Fig. 6.4(a) a FFEM micrograph is presented representative of the whole grid. The image is the shadowed film of the frozen fractured composite, the 'replica'. In the micrograph two different main structures can be seen. In the middle there is a large structure which is composed of building blocks. Around this large structure, which is most likely a silica agglomerate, smaller features are visible, 'ripples' or 'bubbles' due to the liquid crystal structure, which will be considered in more detail later. Apart from some larger features here and there, the features seem relatively smooth and homogeneous. In this regions the features are likely to be representative of the liquid crystal rather than silica agglomerates, that are found in the central large structure. There is a small silica agglomerate visible in the image, giving an idea of what the agglomerates look like. The silica should actually have been washed away using acetyl acetate in the film preparation procedure, but has remained on the carbon film nonetheless, providing us with information about its size. The structures in the composite has sizes about 25.7±10.2nm, larger than the size of the bare silica present on the replica carbon film, 15.3±3.6nm (see Fig. 6.9 where a silica aggregate is present on the carbon film). The agglomerate is thus composed of somewhat larger units than the pure silica agglomerate. This suggests that the silica agglomerates that were used for preparing the replica and here forming the large structure, are covered in a layer of liquid crystal. The units in the agglomerate look like they are connected rather than individual particle clusters. It is likely that the liquid crystal layers on adjacent clusters will connect with each other, thus forming a liquid crystal bridge between

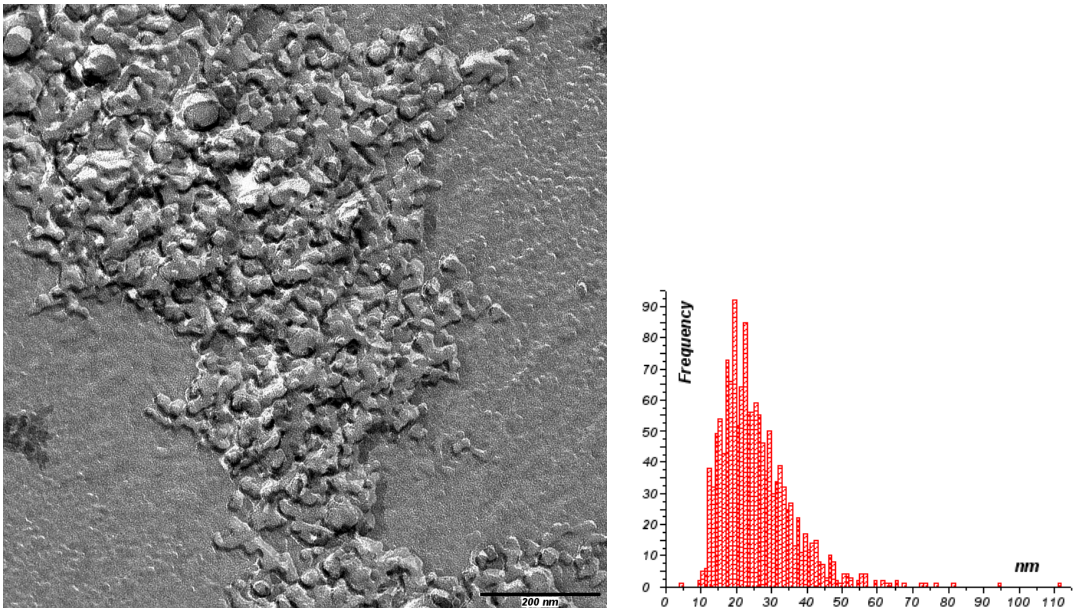

(a) (b)

Figure 6.4: (a) FFEM image of the 1/42 composite prepared at 20°C (RT_1_42 composite). Agglomerates. Scale bar is 200nm. (b) Histogram of the sizes of the features. Diameters of the features were measured manually using SIS-image analysis software. Origin Pro was used to plot the results in a histogram.

neighboring silica clusters. Bridging between regions can then give the appearance of this structure. In the image in Fig. 6.4 the composite fractured in a region where a silica agglomerate is present. In the micrograph the agglomerate remained on the film that was later used for replication. It can be the other way round as well: In Fig. 6.5 a micrograph is shown in which the silica agglomerate did not remain on the shadowed film after fracture but on the complementary film, so that in fact a 'print' of the agglomerate is visible. Around the structure the texture observed in the image in Fig. 6.4 is visible again. In the print of the agglomerate regions of different brightness can be distinguished. The brightness of an area depends on its orientation towards the shadowing target during the replication. In the bottom left the film is somewhat folded after which the film has a different orientation with respect to the shadowing target resulting in a different brightness compared to the rest of the film visible in the image. The features in the print have sizes corresponding to that found in the shadowed agglomerate in the image in Fig. 6.4. When the frozen composite is fractured under liquid nitrogen conditions it will break along regions for which it is easiest to break up. This is for example where there are defect lines between nematic domains or regions where a silica agglomerate separates different nematic domains. In Fig. 6.6 this is schematically illustrated. In Fig. 6.7 a micrograph is presented in which a large

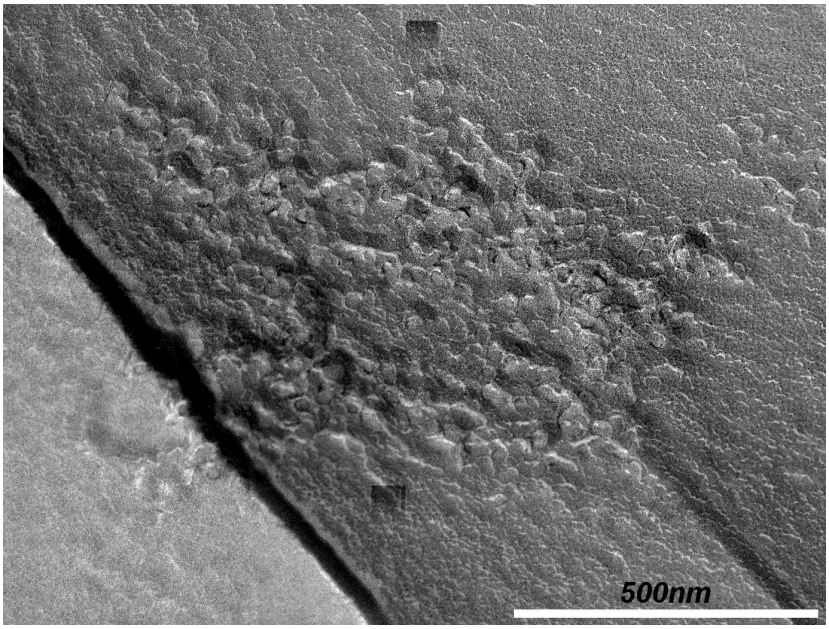

Figure 6.5: The RT_1_42 composite. Example of replica film in which after fracturing the silica agglomerate remained on the complementary film, giving rise to the appearance of a 'print' of the agglomerate. The scalebar indicates 500nm. The squares that appear in the image are an effect of the capturing software.

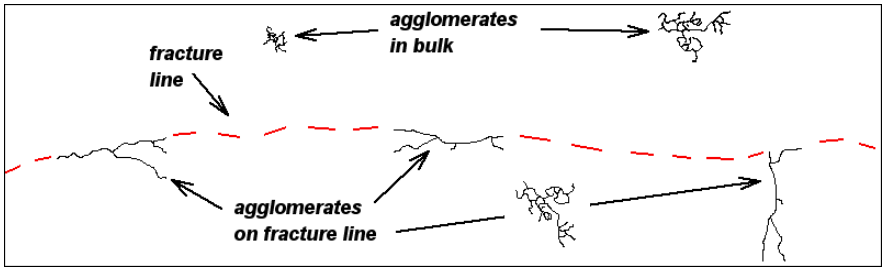

Figure 6.6: Schematic illustrating how the composite can fracture, thus leaving agglomerates on the surface that will be imaged. In one film the agglomerate itself will be imaged (Fig. 6.4(a)), while in the other its print will be imaged (Fig. 6.5).

silica agglomerate has remained on the replica film, in which a large silica agglomerate has been shadowed, after the washing procedure. In the micrograph presented in Fig. 6.7 not only a shadowed and actual silica agglomerate are imaged, but also the liquid crystal film. The dark region in the top right corner of the image is caused by folding of the replica film and is unsuitable for analysis itself. In the bottom left corner there are small features, a small silica cluster and features caused by the liquid crystal. In the features caused by the structure of the liquid crystal there are two main ones, a 'ripple' texture visible all over, and there are steps in the structure. The steps texture look like screw dislocations observed in liquid crystalline material [157]. Each fracture

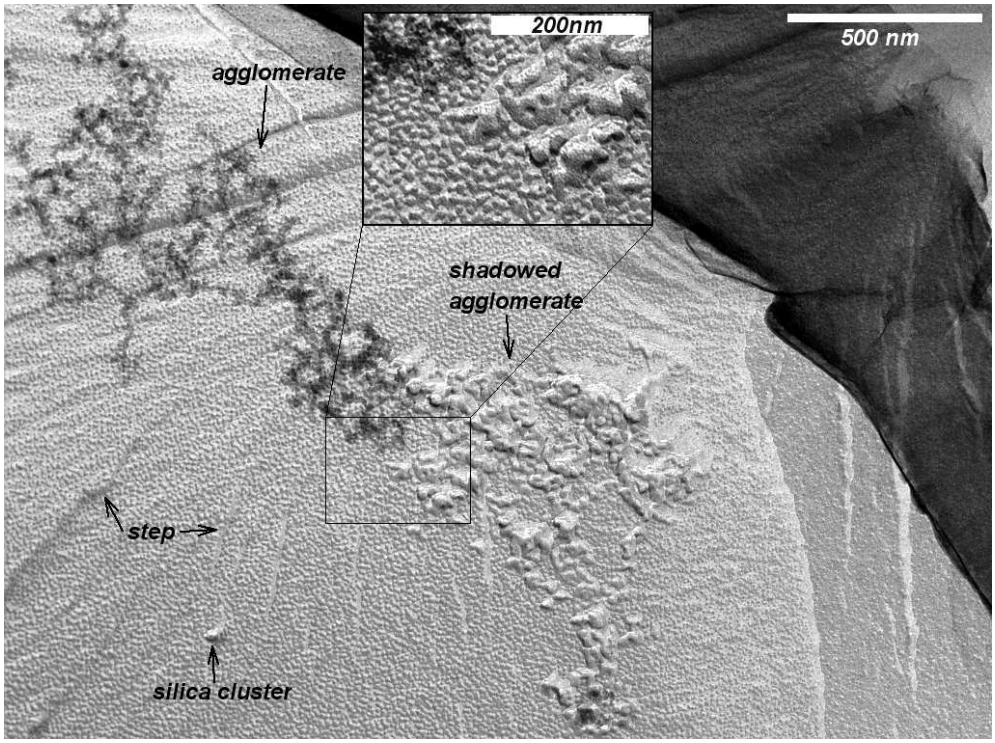

Figure 6.7: The RT_1_42 composite. The structure of silica agglomerates is typically irregular. In the structure of the 5CB liquid crystal nematic subdomains and steps in the structure are visible. The scalebar indicates 500nm. In the inset part of the image is zoomed in, to illustrate the features of the shadowed agglomerates and the 'ripple' texture caused by the 5CB. Scalebar indicates 200nm.

step propagates and can coalesce with other dislocations. In a screw dislocation part of the lattice is shifted with respect to the rest of the crystal, see Fig. 6.8(a) for a schematic illustration. The composite is most likely to fracture in regions in which it is easiest to break up, like at defect lines where nematic regions with different director orientation meet. The 'ripples' have sizes around 12.6±2nm in diameter (see below), which is smaller than the typical silica particle size (15.3±3.6nm). If the 'ripple' structure was caused by silica immersed in 5CB the 12.6nm diameter would be a misleading number, because the silica only partly comes out of the film in that case. The sizes obtained using the FFEM photos are only a rough indication of the actual size. For obtaining more reliable sizes 'rotary shadowing' should be used [158]. When a part of the sample has a different orientation to the shadowing target in the replication step, the size will appear slightly different too. However, the silica agglomerates have an irregular structure while the 'ripple' structure is much more homogeneous. A more likely scenario is that the regular 'ripple' structure is caused by the structure of the liquid crystal. It can be that the structure is formed by nematic 'subdomains' of 5CB. Small scale texture is observed for a different system [159]. The lyotropic

system in that study consists of a mixture of a chiral lipid, nonionic surfactant and water. The observed texture is interpreted by the authors as a direct visualization of a cut of disclination loops. This structure appears different to the 'ripples' observed in the silica-5CB micrographs here. The small scale texture in the article has a length and width of ∼100nm and ∼10nm respectively, while the structure observed in the investigation here have sizes around 12.6±2nm. Since the materials in the studies are fairly different no direct conclusion can be drawn from the scales of the textures. However, this leads to the suggestion that the observed 'ripple' texture might be due to the presence of disclination loops. The steps visible in the micrograph have more or less the same size as the 'ripple' structure, which suggests that the steps represent the terracing in the structure in the liquid crystal. In this scenario the structure in the liquid crystal that is responsible for the appearance of the 'ripple' texture causes the terracing in the structure of the liquid crystal. On the right of the image a darker domain is visible. Here the orientation of the sample is different from that of the rest of the region, evidenced by the darker color of that region. The appearance of this region is different because after fracture this area of the sample had a different orientation towards the shadowing target than the other regions. In this darker region the same features are visible, the nematic 'subdomains' and the steps. The strands

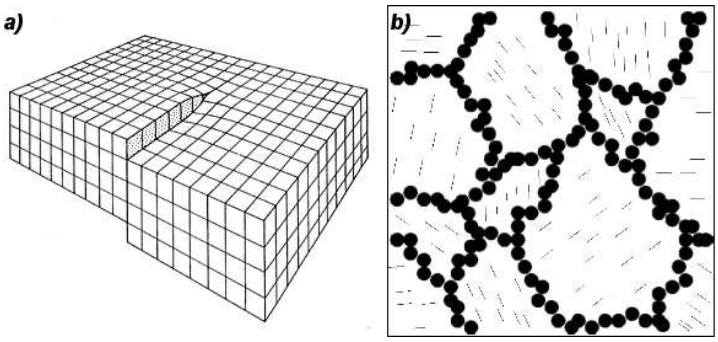

Figure 6.8: (a) Illustration of a screw dislocation in a crystal. (b) The structure of the composite in the proximity of a agglomerate.

of silica particles separate nematic domains from each other and can thus induce a change in the orientation of the nematic director. This is schematically illustrated in Fig. 6.8. From the electron microscopy micrographs the structure of the composite can be assessed, but the exact orientation of the director cannot be distinguished. In the micrograph in Fig. 6.9 the structure of the liquid crystal is further explored. In this image silica agglomerates are still present on the replica film after the washing procedure. In addition various aspects of the liquid crystal are visible. There are defect lines, there is change in direction of nematic director and steps are visible, as well as

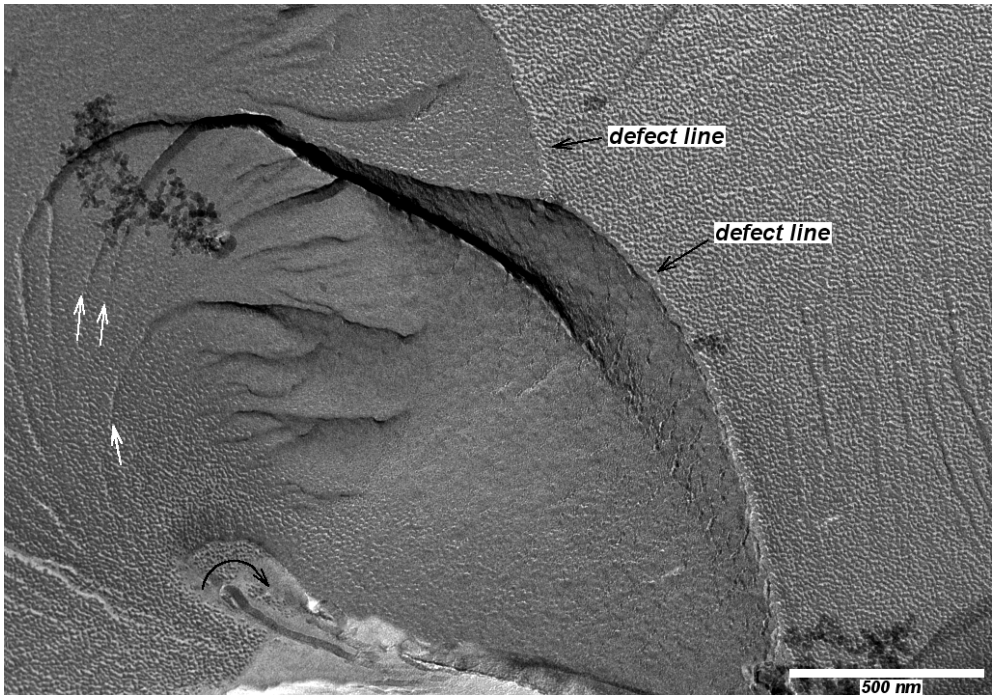

Figure 6.9: The structure of the liquid crystal in the RT_1_42 composite. Different nematic domains build up of nematic 'subdomains' and defect lines are visible. The scalebar indicates 500nm.

indications that the nematic domains are built up of nematic 'subdomains' that have a size of 12.6nm in diameter. On the top right there is again the 'ripple' texture, regions of the size of the nematic 'subdomains' that together form a large nematic domain. The nematic domain is separated from other domain by defect lines, that are indicated in the micrograph. On the other side of the defect line the structure appears different, because the director in that domain has a different orientation. In the bottom left area of the image a continuous variation of the orientation of the nematic director is visible. When going clockwise (see arrow in image) there is a continuous change in the 'ripple' texture, suggesting a changing orientation of the structure responsible for the 'ripple' texture. This implies a changing orientation of the director. Again steps in the structure are visible, which are screw dislocations [157]. In Fig. 6.9 it can be seen that the screw dislocation lines coalesce with each other. The white arrows indicate where each individual screw dislocation line enters the fracture surface. The steps appear differently depending on the region, their appearance depends on how they are oriented with respect to the shadowing target. It is clear from this image that the nematic 'subdomains' are part of the nematic domain which is larger than the size of the image. Nematic domains in a liquid crystal are domains in which the director is different by 90^o. The director can continuously change, or nematic domains can be

separated from each other by defect lines.

FFDI To investigate the composite further, direct imaging was used (FFDI). Here the actual frozen composite is investigated rather than the replica. If anything, the results here are more difficult to understand. Around the edges the fractured film is the thinnest making the film sufficiently transparent for imaging. In the next micrograph, representative for the whole TEM grid, in Fig. 6.10 the structure is examined closely. In the micrograph the fractured film of the frozen composite is

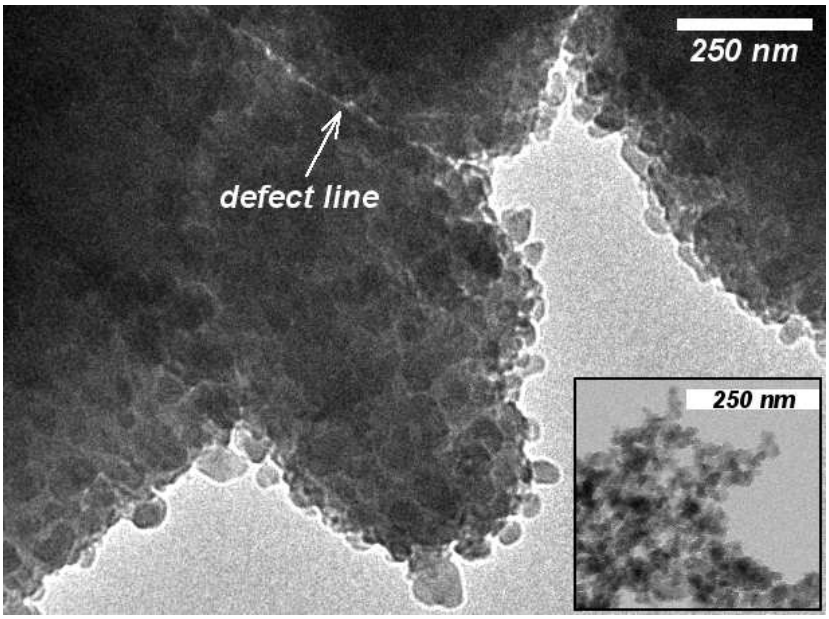

Figure 6.10: FFDI micrograph of the RT_1_42 composite. The structure of the 5CB liquid crystal, which was prepared at 20^{o}C. There is no evidence that silica is present in the imaged region. Inset: a typical transmission image of a silica agglomerate shown on the same scale.

imaged. The contrast depends on the sample thickness and the composition of the material. Darker regions indicate more dense regions. Spherical features are more or less homogeneously distributed in the film. In the inset an image of pure silica particles is shown, at the same scale as the fractured film. The size of the silica aggregates in the inset are roughly a third of the size of the spherical features sticking out of the film in the main image. However, the structure seems more or less similar, they both show irregularities. In the spherical features no subunits can be distinguished, which would have supported the idea that the features sticking out of the film consisted of silica aggregates. For imaging the bare silica the standard TEM method was used. The TEM grid was dipped into a ethanol solution with silica particles, and after evaporation of the solvent the grid was imaged. The silica particles are smaller in size (15.3±3.6nm) compared to the spherical features (49.7± 12.2nm, see Fig. 6.12) visible in the film of the composite. The structure of the silica agglomerate in the inset is

different from that in the fractured film of the composite (apart from the bits that stick out of the film). This means that the spherical features observed in the image is likely to be formed by the liquid crystal. The nematic domains are clearly visible in this micrograph, as well as a large defect line between different regions. Defect lines are not clearly visible between the individual nematic domains, indicating that the transition from one domain to the other is smooth. The director changes orientation between these region continuously rather than abruptly. However, this is not true for the large defect line between two regions. Here there is a clear mismatch between the orientation of the nematic director between the regions. In many places on the grid evidence of terracing in the structure is observed, see Fig. 6.11 for a representative example. The presence of terraces in the liquid crystal is in agreement with the step

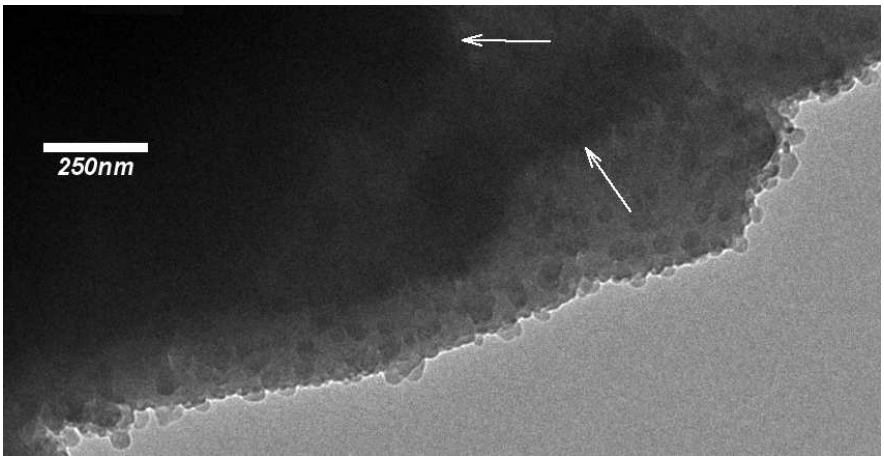

Figure 6.11: FFDI image of the RT_1_42 composite (prepared at 20^{o}C). In the structure different terraces of nematic 'subdomains' are visible. The white arrows indicate where another layer starts.

structure visible in the images in Figs. 6.7 and 6.9. The steps in these figures have around the same size as the nematic 'subdomains' ('ripple' texture), that together from larger nematic domains. The micrograph in Fig. 6.11 again supports the idea that the steps represent the layering of the nematic 'subdomains' in the liquid crystal. The typical size of the spherical features here are larger than those of the nematic 'subdomains' that were observed in Fig. 6.7. This indicates that the spherical features in this image consist of several nematic 'subdomains', in which the director has the same orientation, forming a larger nematic domain. In Fig. 6.12 a micrograph is shown in which a thin part of the frozen composite is imaged, zoomed out more to show more macroscopic detail. In the composite the nematic domains with an average size of 49.7±12.2nm in diameter can be distinguished, that are more or less homogeneously arranged. In Figs. 6.4 and 6.7 it is established that the silica particles form irregularly shaped agglomerates. In this image the irregular shape like that found in the silica

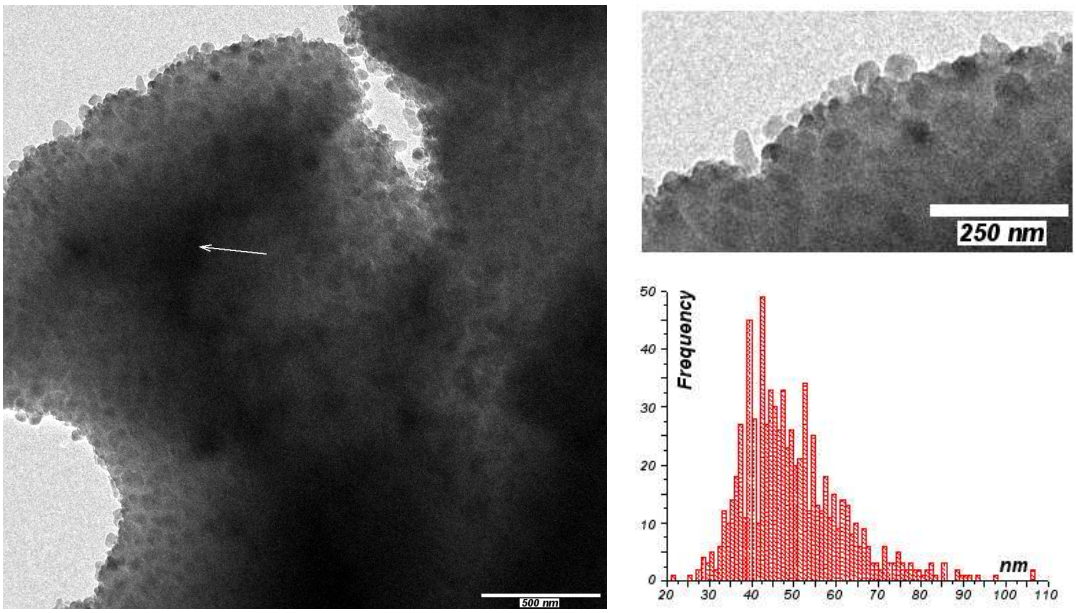

(a) (b)

Figure 6.12: FFDI (a) The RT_1_42 composite. Photograph taken at -196^{o}C of the frozen and fractured composite (scalebar 500nm). Spherical features are apparent. White arrow: see text. (b) Histogram displaying diameter (nm) of spherical features. The average size is 49.7±12.2nm in diameter. The composite was prepared at 20^{o}C before the freezing and fracturing.

agglomerates can be vaguely distinguished in the thicker region of the composite film (white arrow in Fig. 6.12). Due to the composite film being thick the resolution of imaging is not very good on that region.

In the investigation one region with a different structure was found, not representative for the rest of the grid (Fig. 6.13). This part of the film has a structure that is surprisingly similar to that of the silica agglomerates, which have a fractal character. The structure between the silica particles (insets) and that of the film are both shaped irregularly. For imaging the bare silica the standard TEM method was used. The structure in this image generally has sizes larger than the spherical features that are observed in many regions of the grid (see for example Fig. 6.12). The structures in this image have sizes that are roughly ten times that of the silica aggregates that are visible in the insets. The inset on the top right illustrates silica particles on the same scale as the main image. The inset on the bottom left shows a higher resolution micrograph of the bare silica particles to illustrate the structure of the silica agglomerates. When one compares the structure in the main image with that for the bare silica in the high resolution inset, it can be seen that the structures are roughly similar, but on different scale. The silica structure is roughly ten times smaller than

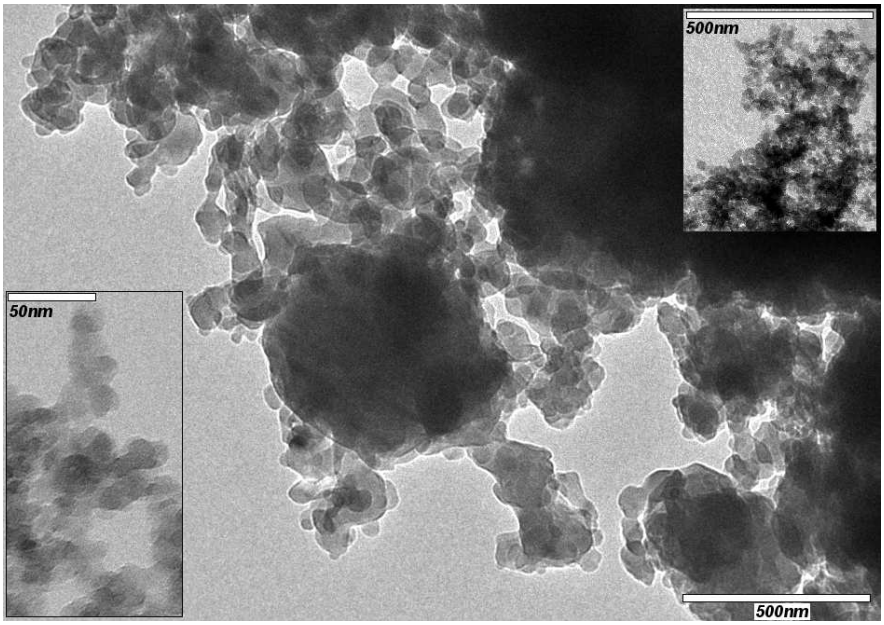

Figure 6.13: Rare FFDI image of the RT_1_42 composite (prepared at 20^{o}C) showing structure reminiscent to that of the structure of silica aggregates (see the insets).

the structure in the main image. When the structure in the main image is compared with the bare silica structure on the same scale, low resolution inset on the top right, again the irregular structure in both can be recognized. However, in the structure in the main image the silica particles cannot be recognized as individual building blocks like in the low resolution inset. The structure in the main image does seem to be build up of certain building blocks, but it is not clear whether these are silica units or 5CB units. Since this structure is not observed elsewhere on the grid, the formation of this structure could be the result of an artefact in the preparation process.

To clarify the uncertainties in the study the liquid crystal needs to be investigated in the same manner without silica particles dispersed in it. So far it is unclear what exactly causes the spherical features found in the FFDI investigation (e.g. Fig. 6.10), whether it is the silica or the liquid crystal responsible for the appearance of those features.

6.4.2 5CB-silica composite structure at T=50^{o}C

The structure of the same composite (1/42) is investigated when the composite is prepared at 50^{o}C. The constituents were mixed together in a glass vial using an ultrasonic probe set at 18 Watts (Sonics & Materials). The silica particles and 5CB were weighed out at room temperature, such that the particles have a concentration of 1%$_v$. The composite was brought to 50^{o}C using a temperature-controlled water bath.

The sandwich was inserted in the composite at 50^{o}C and was left for approximately 30 minutes to equilibrate. After equilibration the sandwich was 'plunged' into liquid ethane, to freeze the composite as fast as possible without affecting the structure. For the plunging in this case the plunging device could not be used due to experimental constraints, which means that the freezing step was not optimal. The frozen composite is fractured under liquid nitrogen (see p. 40 for a more detailed description), after which the sample is replicated using the shadowing technique. The replica film is studied using electron microscopy (FFEM procedure). Figure 6.14 shows an image representative of the structure found in the investigation. The features observed are less sharp than those found in the study for the same composite prepared at 20^{o}C.

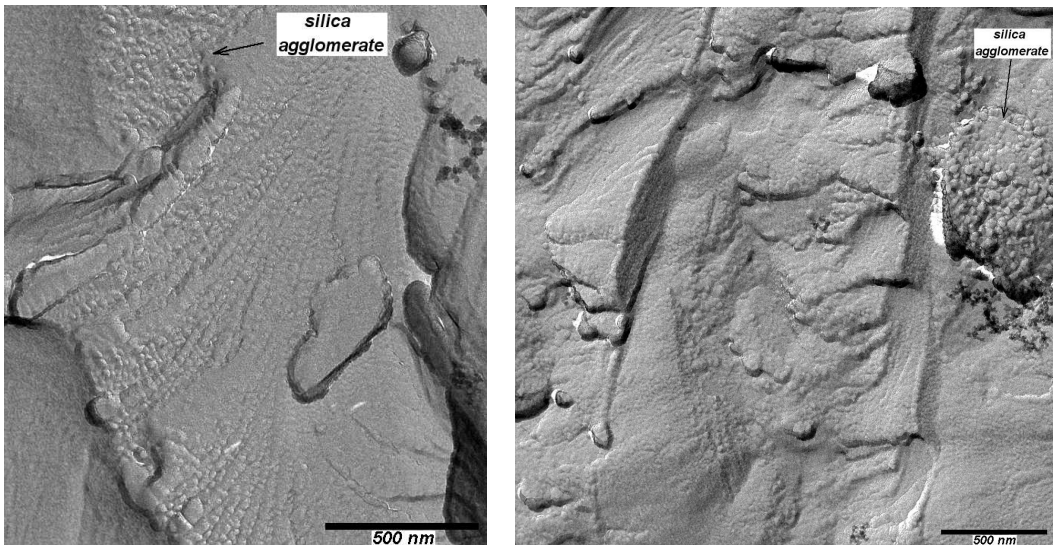

(a) (b)

Figure 6.14: Micrographs made in the FFEM investigation of the 1_42 composite which is prepared at 50^{o}C (T50_1_42). Scale bar is 500nm.

The micrograph in Fig. 6.14(a) is somewhat enlarged for clarity. The structure is different from that for the composite when it is prepared at 20^{o}C. Silica agglomerates are visible in the images (indicated by the arrows), but the structure is not as clear as in the micrograph in Fig. 6.4. There is still a more or less regular structure in the liquid crystal, with steps still present in the structure. This indicates that the structure that the liquid crystal has when it is in the nematic phase is not completely vanished for the composite prepared at 50^{o}C. It is most likely that the freezing of the sandwich was not fast enough, which means that the composite will most likely have changed in this step.

6.5 Rheological properties of the 5CB-silica composite

The structural properties of the composite at room temperature was studied using rheology measurements. The aim of the experiments is to examine whether the 5CB exhibits different rheological behaviour when silica particles are added. The pure liquid crystal, 5CB, was studied as well as the 1/42 and 2/32 composites. The cone-plate geometry was used in all experiments for measuring the composite's properties.

In all experiments a preconditioning step was applied to erase the composite's history that is introduced by the loading of the sample onto the apparatus. In this step the composite is subjected to a constant shear of 5.0 1/s for 60 seconds.

Stress sweep In this measurement the composite or pure 5CB is subjected to oscillatory shear at a constant frequency which is chosen to be 1 Hz. Here the stress is varied from 0.1Pa to 10Pa and is swept back as well. The behaviour of the elastic (G') and loss (G") moduli are studied, which describe the mechanical response of the material. In the graph in Fig. 6.15 the response of the system as function of the

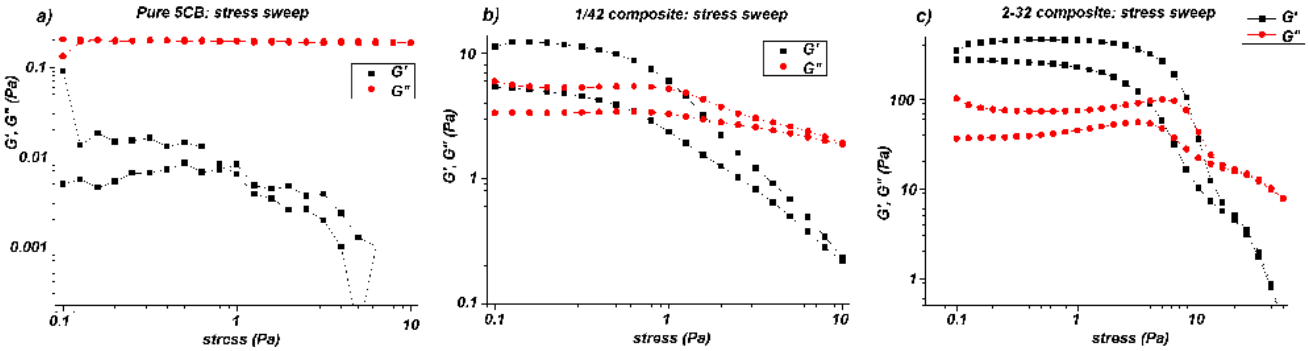

Figure 6.15: The mechanical response to varying applied stress at a constant frequency (1 Hz). The composites studied are pure 5CB and the 1/42 and 2/32 composites. Measurements are made from 0.1Pa to 10Pa and back. In all graphs the upper curves represent the sweep to 10Pa, while the lower curves are those for the sweep back to 0.1Pa. The 2/32 composite is swept to 50Pa and back.

applied stress is measured. The behaviour of G" for 5CB is independent of the applied stress, both on the sweep with increasing stress and decreasing stress. G" describes the liquidlike response of the material. The value of G' shows a decrease for increasing oscillatory shear, the lower curve for G' is the one where the measurement is performed from 10Pa to 0.1Pa. Over the whole range G" dominates indicating that the system, pure 5CB, is liquidlike over the entire stress range probed. The behaviour observed for the 2/32 system in Fig. 6.15 is significantly different compared to the pure liquid crystal. There are two curves for each modulus, the lower curve is the sweep back from high stress to lower stresses for both moduli, and the values of G' and G" are roughly 1000 times larger than for the pure 5CB. This means that the mechanical response of

the 2/32 composite is significantly larger than that of the pure 5CB. For low stresses G' is dominant, meaning that the composite shows primarily solidlike behaviour. When the oscillatory stress is increased G' starts to drop, indicating the response becomes less solidlike. At the same time G" is changing upon increasing oscillatory stress. Initially it is more or less constant after which a maximum is exhibited before falling off at high oscillatory stresses. Similar behaviour is observed for dense hard-sphere suspensions [160]. At a certain oscillatory stress the G' and G" curves cross each other, this is the oscillatory stress where the response of the composite changes from mostly solidlike to mostly liquidlike. For this composite this occurs roughly at a oscillatory stress of 10Pa. This point can be interpreted as being the yield stress of the composite, because after this point the composite starts to exhibit flow. The yield stress is the applied stress that must be exceeded in order to make the material flow, and the material will not return to its original shape after the removal of the applied stress. At higher oscillatory stresses, i.e. higher deformation, shear-thinning occurs, both moduli drop to lower values. Shear-thinning means that the viscosity of the material drops with increasing oscillatory stress. The values measured for G' and G" for the 1/42 in Fig. 6.15 as a function of oscillatory stress are roughly 10 times smaller than those for the 2/32 composite, and roughly 100 times larger than those for the 5CB. This composite has half as much silica compared to the 2/32 composite and this appears to lead to significant changes. The 1/42 composite is less rigid than the 2/32 composite and therefore has a less strong mechanical response resulting in lower values for G' and G". Also for the 1/42 composite a crossover from a mostly solidlike response to a mostly liquidlike response is measured. For oscillatory stresses below roughly 1.5Pa the response is dominated by G' indicating mostly solidlike behaviour. For oscillatory stresses above $\sim$1.5Pa the 1/42 composite starts to exhibit flow which means that G" dominates the behaviour, indicating that the material response is mostly liquidlike.

Frequency sweep In the elastic regime the behaviour is studied more closely at a constant shear stress, which is chosen to be 0.2Pa. The elastic regime is the regime where the materials show elastic behaviour in the stress sweep experiments (performed at 1Hz), this is the regime where G' is dominant for the composites measured, before the crossover point where the behaviour goes from mostly solidlike to mostly liquidlike. The composites all showed elastic behaviour for stresses at and below 0.2Pa, except the pure 5CB whose behaviour is dominated by G" over the whole stress range probed. The composites studied here are the same as in the previous measurement: pure 5CB, the 1/42 and 2/32 composites. The mechanical response is studied as function of frequency (Hz) at a constant stress 0.2Pa. Both the elastic and loss moduli are measured as a function of frequency. The frequency is swept from 0.1Hz to 100Hz and then back to 0.1Hz. Features such as shear thinning and shear thickening can

be distinguished. In Fig. 6.16 the measurements for the pure liquid crystal 5CB and

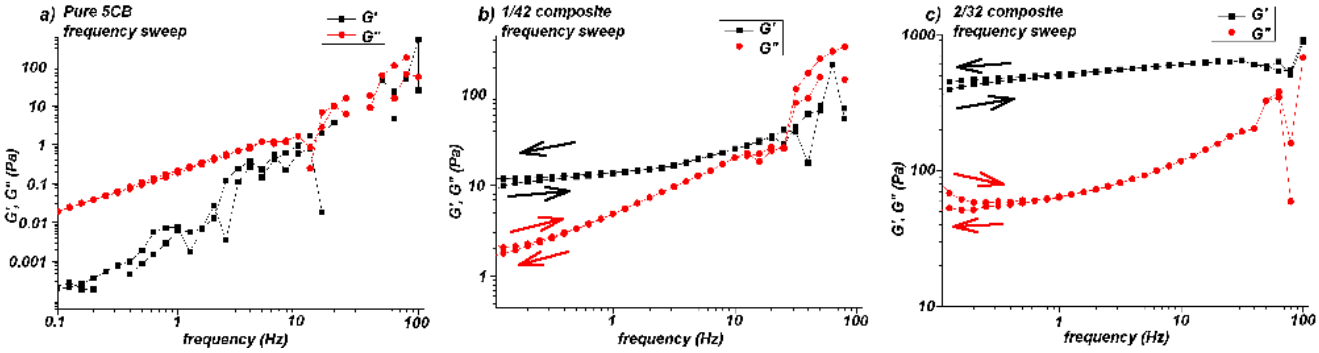

Figure 6.16: The mechanical response to varying frequency at a constant stress (0.2Pa). The composites studied are pure 5CB and the 1/42 and 2/32 composites. Measurements are made from 0.1Hz to 100Hz and back. The response at low frequencies for the composites is different for the sweeps up and down. The direction of the sweeps are indicated with the arrows.

the 1/42 and 2/32 composites are presented. The 5CB exhibits liquidlike behaviour at all frequencies measured, the solidlike response is always smaller than the liquidlike response. For higher frequencies the values of G' and G" both increase, which means that the mechanical response is larger. When the frequency is higher the cone rotates over a shorter distance with larger velocity than at lower frequencies. For the higher frequencies the data is noisy, in this regime the composite does not attain equilibrium in the measurement time. In the graph of 5CB in Fig. 6.16 there are some points missing, at the higher frequencies. The measured values for G' and G" were negative for the points that are missing in the graph, due to the noise. The value G' and G" measured for the 1/42 composite is roughly 100 times larger than for that of the pure 5CB. Also in this measurement the data exhibits more noise at higher frequencies. G' dominates the behaviour of the 1/42 composite for most frequencies, which means that the mechanical response is mostly solidlike. At a certain frequency the G' and G" curves cross each other, the composite makes a transition from solidlike to liquidlike behaviour. For the 1/42 composite this crossover is at ca. 28Hz. In the liquidlike regime the structure in the composite is destroyed, while in the solidlike regime the structure does not break and behaves elastically. It can be seen that the curves do not exactly overlap at low frequency (0.01Hz). For G' the value at 0.1Hz is smaller at the sweep to 100Hz than at the sweep back to 0.1Hz. For G" the effect is opposite, at the sweep to 100Hz the value of G" is larger than at the sweep back. This means that the composite initially behaves somewhat less solidlike than after the frequency sweep. This can originate from the preconditioning step in which the composite is subjected to 5.0 1/s pre-shear for 60 seconds, during which bonds in the composite can break leading to a somewhat more liquidlike behaviour. When the composite is

subjected to stress at high frequency the behaviour becomes more liquidlike as said before. When swept back from 100Hz to 0.1Hz bonds in the structure can reform when the frequency is low enough so that bonds can stay intact. This can also account for the result that the values for G' and G" at 0.1Hz are as observed. The behaviour of the 2/32 composite is mostly solidlike over the frequency range probed, the value of G' increases somewhat with increasing frequency. The value of G" increases more rapidly over the frequency range probed than G', which means that the behaviour becomes increasingly more liquidlike. However, no crossover is observed in the probed frequency range of G' and G" which means that the 2/32 composite response is mostly solidlike over this range. Again it can be seen that the curves do not exactly overlap at high frequency, which was also the case for the 1/42 composite for the same reason. Also in this measurement the data at higher frequencies is more noisy, as was observed for the pure 5CB and 1/42 composite as well.

Steady state flow The behaviour of the shear stress (Pa) as a function of the shear rate (1/s) is measured in this experiment. From these measurements the yield stress can be deduced, in addition to the measurements performed in the stress sweep. From the stress sweep measurements yield stresses for the 1/42 and 2/32 were found to be ∼1.5Pa and ∼10Pa respectively. In the curves several measurements for every shear rate were performed. The conditions were chosen such that the values of the stress response had to be within 2% from each other for 4 subsequent measurements. The shear rate is swept from 0.01 (1/s) to 1000 (1/s) and back. However the maximum measurement time per point was set to be 5 minutes. In Fig. 6.17 the flow curve of pure

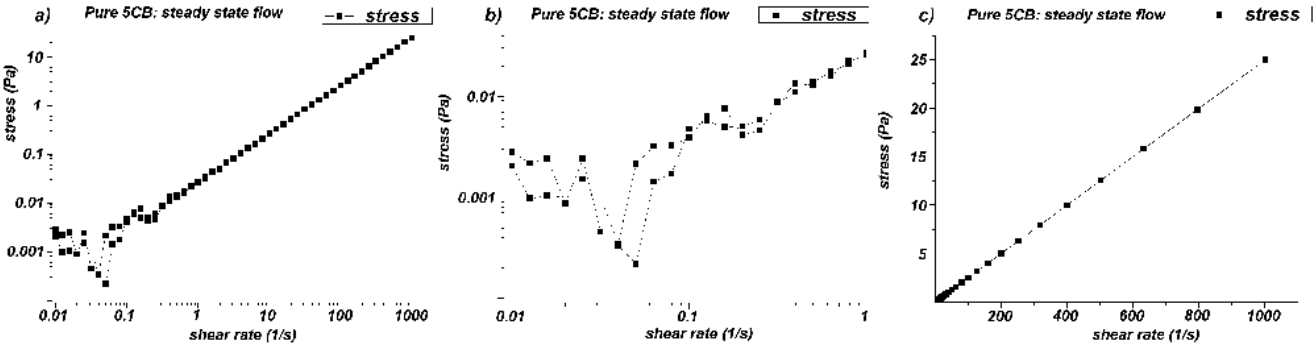

Figure 6.17: Pure 5CB: shear stress as function of shear rate. The curves are plotted on a log-log scale for the graphs in (a) and (b). In (c) the data is plotted on a linear scale to illustrate more clearly the Newtonian behaviour exhibited by the pure 5CB.

5CB is presented. At low shear rates the measured response values were not within 2% from each other and is observed to be very noisy. In this low shear rate regime the composite is able to change significantly during the measurement but equilibrium is not attained during the measurement time (which is set be maximal 5 min.). For shear

rates larger than 1 (1/s) a straight line is observed in Fig. 6.17(a). In Fig. 6.17(c) the same measurement is plotted, but then on a linear scale, to visualize the behaviour. On the linear scale a straight line is observed, characteristic for Newtonian liquids. The 5CB exhibits no yield stress.

In Fig. 6.18 the flow curve of the 1/42 composite is presented. The behaviour is different compared to that of the pure 5CB. Initially the shape of the curve is not

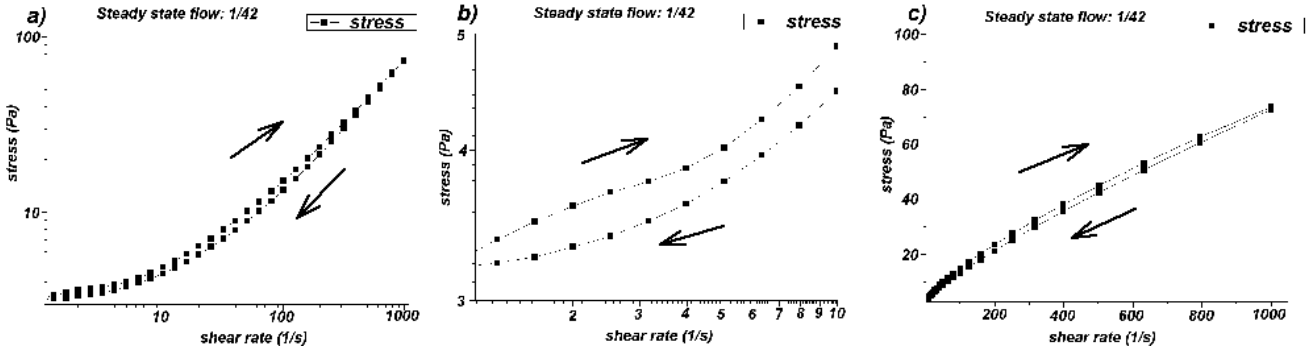

Figure 6.18: 1/42 composite: shear stress as function of shear rate. The curves are plotted on a log-log scale for the graphs in (a) and (b). In (c) the data is plotted on a linear scale to illustrate more clearly the shear-thinning behaviour exhibited by the 1/42 composite.

straight, even though for high shear rates the curve is more and more like a straight line. From these measurements the yield stress of the 1/42 composite can be deduced more precisely. This is the value of the stress at zero shear rate, which is more or less 3.3Pa. Another feature is that the two measurements have not exactly the same curve as is the case for the 5CB, there is hysteresis. The arrows in the figure indicate the direction of the measurements, the upper curve is the measurement starting at 0.01 (1/s) while the lower curve is the measurement from 1000 (1/s) to 0.01 (1/s). In Fig. 6.18(b) the curve measured at low shear rates are plotted to show the hysteresis more clearly. Before the measurement the composite has a certain structure in which the silica particles are expected to exist as agglomerates. These are broken up in the measurement at higher shear rates, which means that the curve measured after this breaking up is different as the structure now has changed. In Fig. 6.18(b) there is a slight 'bump' visible in the curve measured from 1 (1/s) upwards, at a shear rate of $\sim$3.5 (1/s). This is most likely caused by the break-up of large silica agglomerates. The higher the shear rate the more the structure is destroyed. The agglomerates are broken up into smaller aggregates or clusters. This means that for the measurement that starts at a shear rate 1000 (1/s) the composite has a structure in which the silica is broken up into smaller clusters. After the agglomerate break-up the composite starts to behave more liquidlike. In Fig. 6.18(c) the same curve is shown, but on a linear scale. From this graph can be seen that the composite shows shear-thinning behaviour.

In Fig. 6.19 the flow curve of the 2/32 composite is presented. From these

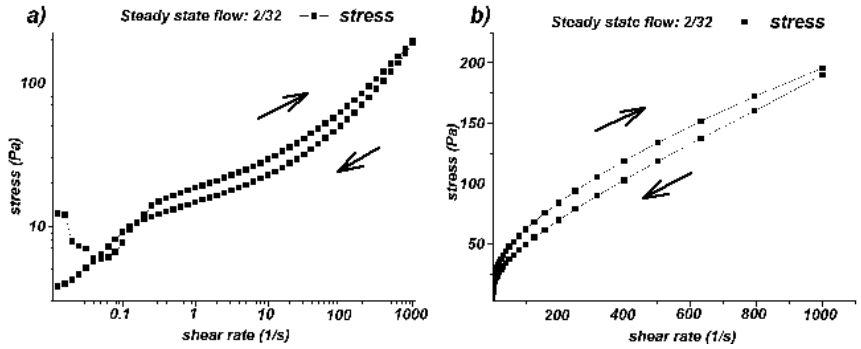

Figure 6.19: 2/32 composite: shear stress as function of shear rate. The curves are plotted on a log-log scale for the graph in (a). In (b) the data is plotted on a linear scale to illustrate more clearly the shear-thinning behaviour exhibited by the 2/32 composite.

measurements follows that the yield stress for the 2/32 composite is about 15Pa. The curve measured shows hysteresis, originating from the silica structure in the composite, as occurs in the 1/42 composite. The hysteresis behaviour is more dramatic for the 2/32 composite. Initially upon increasing shear rate the stress response has low values before increasing at shear rates between 0.1 and 1 (1/s). It can be seen that just after starting the measurement the response stress drops from ∼15Pa to ∼6Pa before increasing again after 0.1 (1/s). This has to do with the yield stress of the 2/32 composite. This stress needs to be overcome before the material starts to flow. In this case for the 2/32 composite a minimum shear rate of 0.1 (1/s) needs to be applied before flowlike behaviour is exhibited.

6.6 Conclusion

In this chapter the structure and properties of the silica-5CB composite were investigated.

In the electron microscopy (FFEM) investigation it has become clear that the silica exist as agglomerates in the 5CB. These agglomerates are fractal in character, which is evidenced in the SAXS measurements as well. The silica agglomerates are distributed over the 5CB, and there are many regions where no silica is imaged. In the FFEM investigation certain features in the 5CB could be detected. The existence of defect lines separating nematic domains were evidenced, and the 5CB within the domains exhibits a 'ripple' or 'bubble' texture, This could be an indication of how the 5CB molecules are arranged in the nematic domain. However, it is not certain that this is not just an effect of the fracturing on the composite during the preparation.

In the FFDI investigation extra features could be detected that can not be evidenced using FFEM. The presence of defect lines are evidenced like in FFDI. However, using FFDI more-or-less spherical features, with sizes larger than the primary silica particles, were detected in the composite. On the edge of the fractured film spherical objects stick out of the film. This is possibly the 5CB, but to be absolutely certain investigations for pure 5CB would need to be performed.

Rheological measurements show rich behaviour. The composites show viscoelastic behaviour, depending on the measurement conditions the response of the studied composite can be mostly solidlike or liquidlike. The addition of silica nanoparticles to the 5CB modifies the behaviour considerably. Upon addition of silica nanoparticles the composite starts to exhibit a yield stress. The yield stress represents the stress that needs to be applied to the material before it starts to exhibit flow behaviour. The more rigid the gel, the higher the yield stress exhibited by the gel, which is true for the experiments. The yield stress for the more rigid composite, the 2/32 composite, is $\sim$15Pa versus that of the less rigid 1/42 composite for which the yield stress is $\sim$3.3Pa. The flow curves demonstrate that the silica structures are breaking on sweeps to high shear rate and reform somewhat as the shear rate is decreased.

The characteristic relaxation time τ can be approximated from the frequency at which the behaviour changes from solidlike to liquidlike [85]. For the 1/42 composite the crossover (G' = G") occurs at a frequency of roughly 25Hz, which means that the characteristic relaxation time is $\sim 4 \cdot 10^{-2}$s. The relaxation time for the 2/32 composite is shorter than that, because the crossover is expected at a higher frequency (which out of the regime probed in the experiments performed in this chapter). This result means that it takes longer for the composite to relax when the concentration of silica nanoparticles is not too high. In the more dense composites it is likely that the silica nanoparticles have stronger bonds because the nanoparticle number density is higher so that the nanoparticles can approach each other more closely. When the silica nanoparticles are closer to each other bonds between them can reform more easily after breakage upon applied deformation. The ability to reform bonds more quickly than the lower density gel can account for the faster relaxation time.

In the following chapter the study of the local dynamic properties of the silica-5CB composite follows.

Chapter 7

The local dynamics of 5CB-silica composite

The dynamics of a gel formed by silica in 5CB is investigated using x-ray photon correlation spectroscopy. Composites with different silica nanoparticles with varying surface hydrophobicity are examined.

7.1 Introduction

The dispersion of colloids in anisotropic media is currently being studied, partly because interesting materials, e.g. cellular structures [161] or soft solid [47], can be formed. Phenomena observed in colloids-LC mixtures originates from the distortion of the director field by the particles. Different defect structures can be formed around single particles depending on the anchoring strength, the elastic properties of the LC and the particle radius. When two or more particles are close to each other, the interaction of these defect fields can induce new types of colloidal interaction [41]. Interesting phenomena have been observed in dispersions of colloids in liquid crystals that undergo isotropic to nematic transition upon cooling [43, 47, 162]. In these studies the particles have moderate attraction and do not stick together. Here we are interested in the case of nanoparticles where the particles have strong attractions. The properties of aerosil silica nanoparticles dispersed in liquid crystal is a subject under intensive study because of the subtle interplay between a soft and tenuous gel and a partially ordered fluid [42, 50, 51, 150, 163–171]. Aerosil (one brand of fumed) silica, pure silicon dioxide (SiO_2), can form agglomerates via hydrogen bonding and form structures when dispersed in a medium, for example a liquid crystal. The particles can hydrogen bond in a network, which introduces disorder in the liquid crystal [163]. Not only does the aerosil perturb on the director of the liquid crystal, but the director also acts on the aerosil particles [42]. The director can be oriented in an external field (e.g. magnetic or electric) which can induce rearrangement of the particles, a process during which hydrogen bonds break and reform.

The hydrophilic surface of the particles gives rise to homeotropic anchoring of the

LC molecules at the surface, and therefore produces a local distortion of the director, resulting in elastic strain (ES), which increases with increasing aerosil concentration. The hydrogen-bonds between the particles can break and reform, so that silica chains can rearrange such that ES is relieved (annealed). The ES that is introduced by the silica particles in 7CB and 8CB is not totally removed (annealed) at the NI-transition [51]. At the NI-transition the LC molecules become aligned to form the nematic phase. In 7CB, at the NI-transition, some ES strain is removed due to the nematic alignment, a fraction of the homeotropically anchored LC molecules now becomes aligned more and more upon cooling in the nematic phase. In 7CB the annealing (removing of ES) is completed at the Sm-N-transition. In 8CB however the ES remains while it is in the nematic phase, and only becomes partially removed at the Sm-N transition [50]. The annealing of disorder introduced by the silica taking place upon cooling is thus not complete, the 8CB molecules remain anchored at the particles' surface upon cooling and cannot align in the same direction as the molecules in the bulk. The phase transition temperature in the low density composite (no gel formation) shifts to lower temperatures upon addition of aerosil [51].

The memory effect in different nematic liquid crystals using an external field is stronger for composites with hydrophilic silica (e.g. Aerosil 300) than hydrophobic silica (e.g. Aerosil R812) [164]. How much the LC molecules remain aligned after removal of an external aligning field is termed the memory effect. The memory effect is not only dependent on the aerosil surface but also the concentration. When aerosil concentration becomes very high the memory effect decreases because ordering of the liquid crystal becomes completely suppressed and alignment of the molecules can not be achieved anymore. Deuteron NMR studies performed on 8CB with hydrophilic silica for a range of silica concentrations show that at low concentration the orientational order of the liquid crystal is mostly bulk like [165, 166]. Increasing the silica concentration results in the formation of a network in which strands grow along the field induced by NMR and stabilize the LC alignment. At low silica density (soft gel) there are still sharp transitions. When the gel is more stiff at higher silica concentration, the introduced random disorder is increased and the ordering under the influence of the aligning NMR magnetic field is less effective. With increasing concentration the random disorder dominates, a rigid and isotropic network forms, and the liquid crystal phase transitions become more broad. Once disorder is fully quenched (stiff-gel regime), phase transitions become first smeared or very broad, and eventually are completely suppressed. Then, a continuously evolving and considerably reduced orientational order is all that remains.

Upon addition of silica to a liquid crystal the isotropic-nematic phase transition is found to exhibit a two-step process rather than a single step as in the pure liquid crystal [167, 168]. This two-step process is demonstrated for silica in 8CB using calorimetric

measurements [167], and the transition temperature shifts to lower temperatures upon increasing aerosil concentration (up to ρ_s=0.1 g/cm^3) [150]. The 8CB molecules relatively far away from the particles' surface shows a NI transition as in bulk 8CB, whilst the 8CB molecules adjacent to the particles' surface have an induced frozen local orientational order. This means that below the NI-transition there still exists isotropic phase due to the particle's presence. When the aerosil concentration is higher than 0.1 g/cm^3 the transition temperature decreases slowly and a single broad peak in the heat capacity is found rather than two sharp peaks [150]. At higher aerosil concentration ES is quenched due to the presence of the aerosil. The authors suggest that the broad peak in the heat capacity indicates ES 'smearing'. The randomness, resulting from the aerosil's presence, introduces a distribution of strains. The authors propose that in the soft gel regime ES responsible for smearing of the transition can be annealed, but the LC at the particle surfaces remains in a disordered state (quenched). Calorimetric measurements performed on CCN47 liquid crystal indicate a two-step process in the NI-transition [168]. Birefringence observations reveal that initially upon cooling nematic domains appear as isolated regions and grow in number, after which the domains distort (defect lines). The defect lines indicate that there is increased coupling of the director with the silica surfaces (more elastic strain). Upon further cooling disordered LC at the aerosil surface orders as well. The situation described here is schematically sketched in Fig. 7.1. The authors conclude that the two successive processes differ in the strength

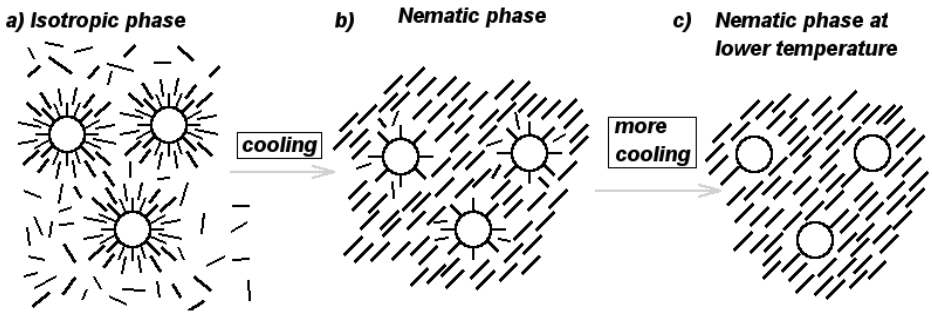

Figure 7.1: (a) Due to anchoring to the particles' surface the molecules have an induced local orientational order. (b) Because the molecules are anchored there still exists isotropic phase below the NI-transition. (c) After sufficient cooling the molecules at the particles' surface orders as well.

of coupling with the silica surfaces. At a lower temperature there is stronger coupling, and the layer of disordered LC at the silica surface, screening the surface, becomes thinner.

When fumed silica is inserted into a liquid crystal the molecular dynamics are affected [163, 169–171]. For silica concentrations of up to 3 wt% the order is suppressed, but more strongly for hydrophilic silica [169]. Electron spin resonance [169]

and dielectric spectroscopy [170, 171] studies performed on 5CB show that molecular relaxation processes such as tumbling and rotation are found to slow down upon insertion of fumed silica. 7CB liquid crystal molecules adjacent to the surface of silica particles are found to have a decreased relaxation time compared to molecules in bulk 7CB using dielectric spectroscopy [163]. This indicates that the molecules located in the surface layers formed by the 7CB molecules at the silica aerosil surface experience hindrance in the molecular rotation. Moreover, it was found that the transition temperature T_{NI} is lowered upon addition of hydrophilic silica particles, at which the 7CB molecules exhibit homeotropic anchoring.

To try and understand how the silica particles and the liquid crystal influence each other the dynamics of the composite are investigated. Studies of dynamics in other glassy systems showed interesting behaviour [76, 172, 173]. Dynamics of these systems are dependent on age and intermittent behaviour can be exhibited.

Scattering data can be analyzed by exploring time-resolved correlation (TRC) [74], a technique that allows the study of intermittent dynamics. In this method the degree of correlation ($c_I(t_w,\tau) = \frac{<I_p(t_w)I_p(t_w+\tau)>_p}{<I_p(t_w)>_p<I_p(t_w+\tau)>_p}$) between pairs of images (taken at a delay time τ) is then measured as a function of waiting time t_w at which the first image was taken. The authors in ref [74] analyze diffusing wave spectroscopy (DWS: a technique which allows one to do light scattering studies on multiply scattering samples.) data using TRC, and demonstrate the existence of temporal inhomogeneities in a concentrated colloidal gel. This same technique was applied by Ballesta et al. to data collected via DWS in colloidal suspensions that are close to the jamming transition [172]. Upon approaching the jamming transition fluctuations in the dynamics were found to increase, but the amplitude of the fluctuations markedly decrease at even higher colloid volume fractions, a result obtained for the first time. They achieved this via quantifying the fluctuations of the dynamics in time by calculating the variance of the degree of correlation $c_I(t_w,\tau)$, a quantity corresponding to the dynamical susceptibility χ_4 [174]. χ_4 quantifies the amplitude of dynamical fluctuations, if the value of χ_4 is higher, the correlations are more long-range. The first experimental measurement of χ_4 has been made by Mayer et al. [175] in a coarsening foam using diffusing wave spectroscopy (DWS).

The fluctuations of the dynamics in a colloidal glass were for the first time studied using XPCS by Wandersman et al. [173]. XPCS is applicable in a wide range of systems, in the study of for example domain coarsening of sodium borosilicate [176], kinetic evolution of unmixing in AlLi alloys [177], or slow dynamics and aging in a colloidal depletion gel [76]. The number of independent cooperative regions in glasses

is much higher than in gels, and the dynamic fluctuations (inversely proportional to the number of independent regions) are much smaller, which results in a smaller χ^* (maximum value of χ_4) for glasses. χ_4 is peaked around τ_c, the systems' characteristic relaxation time. The peak height can be different for different q-values, but it can also be the same height for the q-range studied. If the maximum peak height is not dependent on q, this indicates that dynamical heterogeneities do not depend on the length scales probed in the system. A smaller value of χ_4 indicates that there are smaller dynamical fluctuations.

Retsch et al. studied the behaviour of an aerosil gel embedded in 8CB liquid crystal using x-ray intensity fluctuation spectroscopy (XIFS, XPCS) [178]. They use an aerosil concentration above the percolation threshold but below the stiff gel regime (used: 0.06g/ml). Importantly, they studied the pure aerosil gel, not embedded in 8CB, but with the aerosil sprinkled on a silicon nitride window, which revealed that the pure gel is a dynamical system itself. When embedded in 8CB, the gel dynamics can be activated by coupling to the 8CB. The authors explain that here the gel acts as a 'shock absorber' to thermally driven director fluctuations in the 8CB. The fluctuations of the nematic director can lead to torques acting on the gel network, such that the gel network has prolonged relaxation times. Because the gel takes away energy from the nematic director fluctuations by absorbing it, the effect of the fluctuations on the 8CB dynamics is reduced. The gel basically dampens the director fluctuations, which is possible because the gel and the liquid crystal are coupled to each other.

Duri and Cipelletti study the dynamics of a colloidal fractal gel, and demonstrate, by investigating the temporal fluctuations of c_I for various q values, that the slow dynamics are due to intermittent rearrangements [179]. The rearrangement events are interpreted to correspond to forming and breaking of bonds along the gel network.

The aging of a colloidal gel is explained using a dipole model [180]. The authors looked at experimental data presented in ref. 6 [181] in their article. In those experiments the time decay was observed to be faster than exponential. The static structure factor exhibits the same shape when the sample is aging, while the relaxation of the gel dynamics becomes slower. In the model described by Bouchaud and Pitard the gel is visualized as chains of beads and springs. If one imagines a chain of particles in the gel all at an equivalent distance from each other to start of with. Two adjacent particles can aggregate, and the particles both impose forces on the chain in opposite directions from the aggregate. At the aggregate a dipole of forces is now created, and strain is now present in the chain. This happens all throughout the gel. The local

aggregation of particles in the gel is referred to as an event, a 'micro-collapse'. The micro-collapses induce strain on the surrounding non-collapsed regions. For particles in the strained region the barrier for rearrangement has now increased, which makes it harder for these regions to collapse. New events are more likely to occur in less strained regions, away from collapsed regions, which induces spatial correlations between micro-collapses.

Here we expand our characterization of the structure and bulk flow properties of chapter 6 with a study of the aging and dynamics of the 5CB-silica gels. Although the silica nanoparticles are strongly attractive the structure of the gel is far from permanent and stationary.

7.2 Experimental Methods: silica in 5CB

7.2.1 Compound details

In the experiments the liquid crystal (LC) used is 5CB (CAS 40817-08-1, 4-cyano-4'-pentylbiphenyl), a thermotropic liquid crystal exhibiting an isotropic to nematic phase transition at 35.3^{o}C. In the nematic phase and isotropic liquid the 5CB molecules are associated, forming dimers due to dipole-dipole interaction [155]. In the nematic phase there is long-range order. When fumed silica is added to the 5CB this leads to the formation of intermolecular hydrogen bonds between the LC and silica nanoparticles. The more hydrophilic the nanoparticle surface is, the more strongly homeotropic the induced alignment will be. The fumed silica nanoparticles used in the experiments are from Wacker Chemie AG, Germany. The silica nanoparticles are synthesized via hydrolysis at over 1000^{o}C [156]. Volatile chlorosilanes ($SiCl_4$, $HSiCl_3$, H_2SiCl_2) are introduced into an oxyhydrogen (O_2 and H_2 mixture) flame, producing hydrogen chloride (HCl) and high-viscosity SiO_2 primary particles about 5-30nm in size. These particles have a non-microporous smooth surface. In the flame, the primary particles fuse together permanently to form large units, or aggregates (100-1000 nm in size). Hydrophilic HDK has ca. 2 silanol groups per nm^2. If the Si-OH groups are allowed to react with organosilicon compounds, the silica has more hydrophobic properties included. Hydrophilic silica is wetted by water and can be dispersed in water.

7.2.2 Sample preparation

The fumed silica (wacker) and 5CB were mixed together in a glass vial by means of an ultrasonic probe (Sonics & Materials, 18 Watt) combined with using magnetic stirring to help disperse the particles in the 5CB. The silica particles and 5CB were weighed off at room temperature, such that the particles have a concentration of 1%$_v$ or 2%$_v$,

corresonding to silica concentrations ρ_s=0.02g/cm^3 and ρ_s=0.04g/cm^3. It is easier to disperse the particles when the 5CB is in the isotropic state and thus less viscous compared to when it is in the nematic phase. For this reason the vials were placed in a water bath which is temperature controlled between 50-55^{o}C while the samples are mixed for 6.5 hours. For the XPCS and cryo-TEM measurements samples from the same prepared batch were used.

In the XPCS experiments, after mixing the sample was slowly put into a capillary after preparation using a syringe. After the capillary has been filled it was sealed using 'hot gun glue'. Syringing the sample can be considered as a form of mixing as it will definitely induce rearrangements in the sample and so this effect has to be taken into account when analyzing the data obtained afterwards. In some cases mixing after filling the capillary was performed by using a wire inside the capillary that could me moved through the sample by using a magnet.

7.2.3 Experiments

The aim of the experiments is to study the dynamics of colloidal silica particles dispersed in a liquid crystal, forming a LC-particle composite. The behaviour of the liquid crystal (its anisotropy) is expected to influence the dynamics and interactions of the particles. Because of the structure of the liquid crystal there are effective interactions between the particles due to the nematic order. These new interactions can exist both prior to the isotropic-nematic transition as well as in the ordered nematic phase [168]. The nature, more hydrophobic or hydrophilic, of the silica nanoparticles dispersed in the liquid crystal is important, as this is expected to influence the disorder introduced differently [164, 169].

The partial coherence of the x-ray source and the motion of the instrument and the beam eventually lead to decorrelation even for a perfectly stationary sample. To obtain meaningful measurements it is essential to check that this correlation occurs on a much longer timescale than the sample dynamics (and that it is isotropic), Fig. 7.2. We tested this by packing dry silica powder tightly into an x-ray capillary (Hilgenberg). The intensity-intensity correlation function revealed that the instrument itself decorrelated after ∼2000 seconds and that its performance was the same in horizontal and vertical directions.

Yuriy Chushkin, an expert in this field, has been so kind to let me use his Matlab based software (XPCSGUI) to calculate the time averaged correlation function $g_2(q,\tau)$ and the two-time correlation function $G_2(q,t_1,t_2)$. After $g_2(q,\tau)$ is calculated for each q IDL 6.3 was used to evaluate the best fit of a model. $g_2(q,\tau)$ is fitted with a function that describes exponential decay $f(q,t) = BL + b \cdot e^{-2(\frac{t}{\tau_c})^{\mu}}$, where BL indicates the

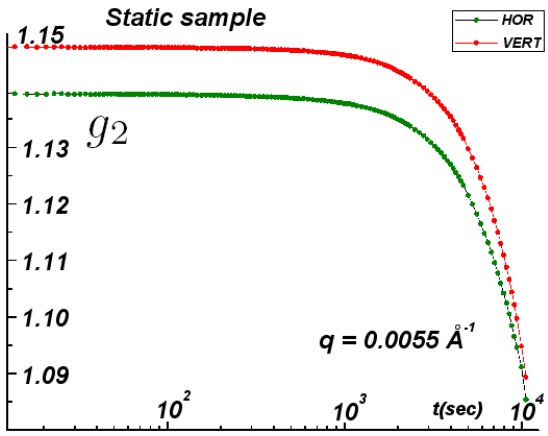

Figure 7.2: The intensity-intensity correlation function of the static sample for orthogonal directions, consisting off dry silica powder packed tightly in a x-ray capillary (Hilgenberg). The measurement demonstrates that the slowest dynamics that can be measured are ∼2000 sec.

value to which the curve decays, and b determines the contrast between the initial and final level of the curve. τ_c is the characteristic decay time which determines where the $g_2(q,\tau)$ curve falls off, indicating how long it takes before the intensity fluctuations decorrelate. μ adjusts the slope of the exponential curve. Values of μ larger than 1.0 implies a faster decay than a normal exponential (compressed exponential), and a value smaller than 1.0 indicates decay that is slower than exponential decay (stretched exponential). Extracting the fitting parameters gives us the opportunity to establish a relationship between the wave vector q and the characteristic decay time τ_c.

7.3 Results

In this section the study of the dynamics of the silica nanoparticle-5CB composite is presented.

The first example taken here is a sample with $2\%_v$ volume fraction of wacker fumed silica particles (ρ_s=0.04g/cm^3), measured at room temperature. The silica particles used in this sample have a surface chemistry such that 32% of the surface is occupied by hydroxy groups (-OH) whilst the remaining surface area is covered in methyl groups (-CH_3), which means the wacker particles are more hydrophobic than when all surface groups are hydroxy groups. This sample is termed RTa_2a_32, where 2 refers to the nanoparticle volume fraction and 32 refers to the surface chemistry of the silica. The capillary was filled approximately 4.5 hours prior to measuring the sample at room temperature, after which the sample was heated to 50^{o}C and measured again. After these two measurements the sample was allowed to cool down back to room temperature and measured again.

The silica-5CB composite shows very rich behaviour, which, to my knowledge, has not been reported before. The results are highly varied, which means that the sample is dynamically heterogeneous on the scale of the beam spot size (few tens of microns on an edge), which is smaller than the nematic correlation length for silica gels ($\sim$ micron) [182]. The wavevector q varies from 0.0033Å^{-1} to 0.017Å^{-1} (corresponding to length scales probed ranging from 190nm to 37nm). In the experiment a CCD camera is used to record the speckle pattern of the light scattered by the sample. The camera captures images at a constant rate at a certain exposure time. The exposure time is determined prior to each experiment, it is chosen such that there is sufficient intensity captured without overexposing the camera. Before every measurement 100 dark images are recorded at the same exposure time. The signal that is still recorded in the dark images is subtracted (pixel by pixel) from the raw signal measured in the experiment [183]. In the analysis the intensity correlation function ($g_2(\tau) = \frac{\langle I(\vec{q},0)I(\vec{q},\tau)\rangle}{\langle I(\vec{q},t)\rangle^2}$) was calculated from the x-ray speckle pattern, to see the sample dynamics. The result for this sample is shown in Fig. 7.3, in which it can be seen that the system decorrelates completely after a time $\simeq$ 1000s with different characteristic relaxation times depending on wavevector. The intensity autocorrelation function g_2 was calculated for different q, which corresponds to different radii on the CCD camera. From Fig. 7.3 (a) it can be seen that the dynamics are slower for smaller (lower) q values. The arrow

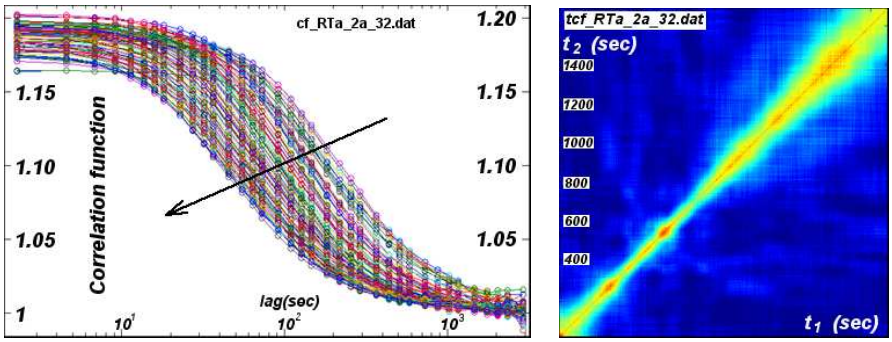

(a) (b)

Figure 7.3: (a) The intensity correlation function (g_2) measured for the RTa_2a_32 composite. The arrow indicates increasing q. From the graph thus can be seen that there are slower dynamics for smaller (low) q. (b) The two-time correlation, from which is clear there is speeding up and slowing down in the dynamics (q is 0.00345Å^{-1}). The numbers indicate the time in seconds.

in Fig. 7.3(a) indicates increasing q, it is observed that the dynamics are slower for lower q values (larger sized scatterer). The curve for g_2 starts of at a certain value $\leq$1.2, representing the maximum degree of correlation (as permitted by details of the experiment). For long delay times the system is no longer correlated which means that g_2 becomes 1. This means that $\langle I(\vec{q},t)I(\vec{q},\tau)\rangle = \langle I(\vec{q,t})\rangle^2$, which means that any

correlations are due to random fluctuations. This also shows that this sample at this temperature appears to be ergodic. In Fig. 7.3(b) the two-time correlation function ($G_2(\vec{q}, t_1, t_2) = \frac{\langle I(\vec{q},t_1)I(\vec{q},t_2)\rangle}{\langle I(\vec{q},t_1)\rangle\langle I(\vec{q},t_2)\rangle}$ see p.46) is shown. The variables used here to describe the two-time correlation function are the average time or age $t_a (= (t_1 + t_2)/2)$ and the time difference $\Delta t = |t_1 - t_2|$ [76]. The two-time correlation function in Fig. 7.3(b) shows that the sample shows interesting behaviour. The age of the sample increases along the diagonal (where $t_1 = t_2$). After the start of the measurement initially the sample's dynamics are speeding up, correlation is lost more quickly. At a later age (300s and 600s) an event is visible, for a short period of about 50s the dynamics are slower. After the events the dynamics slow down again after an age older than 800s. The behaviour shown by the sample is interesting and varied. The intermittent behaviour observed could be due to sudden (re)arrangements in the sample that occur randomly in time. The observed behaviour could have many origins and further analysis is required.

To investigate the sample's behaviour further the analysis repeated for both the horizontal and vertical direction, to see if there is a variation in the behaviour for different direction. To be able to study the speckle dynamics in the horizontal and vertical direction, appropriate regions on the CCD images are selected, as illustrated in Fig. 7.4. For the two different regions selected, again the intensity autocorrelation

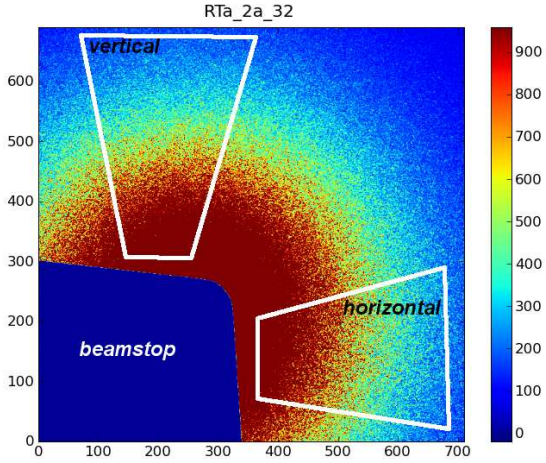

Figure 7.4: Illustration of how the analysis is done when different directions are considered. The analysis for different directions is analyzed. For doing this, speckles in orthogonal directions were selected to analyze, the horizontal and vertical direction. The colour scale on the right indicates the intensity.

function $(g_2(\tau) - 1)$ was calculated from the x-ray speckle patterns. It is possible that the dynamics are different in orthogonal directions, because gravity can have an effect on the aging of a system [174]. When a system relaxes in time this can be influenced by gravity. Because of this we might expect dynamics in the horizontal direction to be faster as the system relaxes faster in this direction. Indeed when calculations are

performed for the sample (RTa_2a_32) it is revealed that the system not only shows a speeding up in relaxation times followed by a slowing down, but also shows directional anisotropy. This can be seen from the graphs presented in Fig. 7.5. In Fig. 7.5(a) the autocorrelation functions for different q for the horizontal direction is presented, and in Fig. 7.5(b) that for the vertical direction. In each graph several curves are

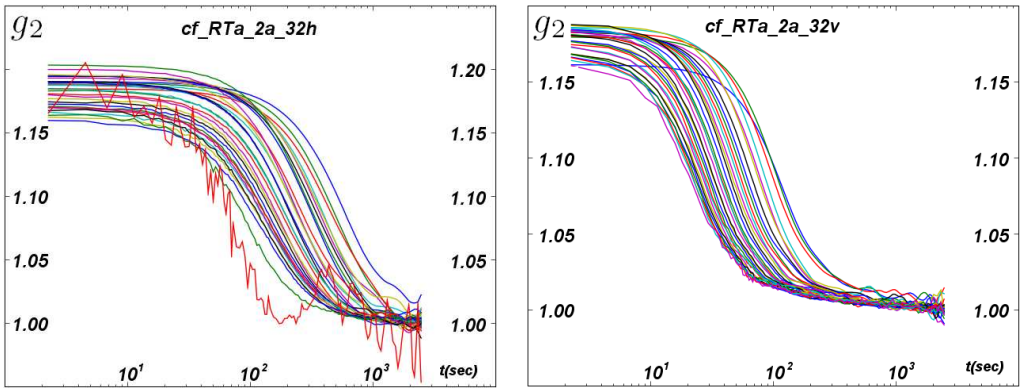

(a) (b)

Figure 7.5: The RTa_2a_32 composite. The intensity correlation functions $g_2(\tau)$ calculated as a function of the delay time for (a) the horizontal and (b) the vertical direction. The anisotropy of the wacker-5CB composite is evidenced here. The system decorrelates faster in the vertical direction.

shown, each curve is the intensity autocorrelation function for a certain q-value. Like in Fig. 7.3, slower dynamics are observed for smaller values of q. For larger values of the delay time (x-axis) the curve is not smooth, in this region the errors are larger. This is because the larger the delay time chosen, the less data there is available, thus increasing the error. In this sample (RTa_2a_32), the decorrelation in the horizontal direction is slower than in the vertical direction. This result is intuitive, when the effect of gravity is considered. Because gels are likely to relax faster in the vertical direction, the direction in which gravity has an effect, a faster decorrelation in this direction is expected. The investigation of the sample (RTa_2a_32) is taken further to explore the sample's behaviour more. To understand the sample's behaviour further the fit parameters for $g_2(\tau) - 1$ are looked at in more detail. As mentioned before, $g_2(\tau) - 1$ is fitted with a function that describes exponential decay $f(q,t) = BL + b \cdot e^{-2(\frac{t}{\tau_c})^{\mu}}$. From the fitting data the relationship between the wavevector q and the characteristic decay time τ_c and μ can be examined. Both the horizontal and vertical directions are examined, see Fig. 7.6. A first clear observation to be made is that $\frac{1}{\tau_c}$ varies linearly with q, which indicates that the mechanism(s) leading to the decorrelation is not of diffusive origin (for which $\frac{1}{\tau_c} \propto q^2$ [174]). The linear relationship between $\frac{1}{\tau_c}$ and q observed here has also been observed in many other soft glassy systems [174] and has

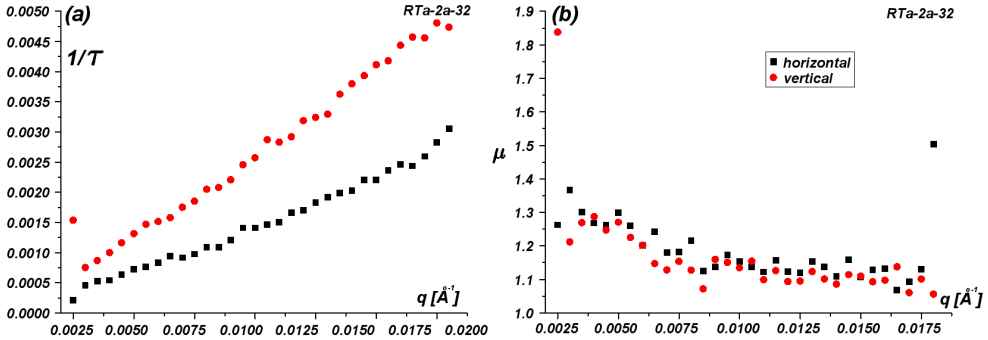

Figure 7.6: The RTa_2a_32 composite. Fit parameters as function of wavevector q for the horizontal and vertical direction. A linear relationship between $\frac{1}{\tau_c}$ (a) and q is obtained for both directions. The values obtained for the fit parameter μ (b) indicates that the decorrelation is faster than exponential (compressed exponential).

been attributed to randomly distributed internal stress sources acting on the sample. It is suggested that the q dependence of $\frac{1}{\tau_c}$ indicates movement in the sample with a velocity $v \sim (q\tau_c)^{-1}$ [181]. Secondly, the behaviour of the fit parameter μ is observed to be around a value of around 1.3, indicating that the decorrelation is faster than exponential (we have a compressed exponential). μ in the horizontal direction is 1.5 for small q and decreases to 1.16 for larger q, while for the vertical direction μ varies from 1.52 to 1.22. For both the horizontal and vertical direction the decorrelation is faster than exponential (we have a compressed exponential), but for the vertical direction μ is larger, indicating a different character of relaxation vertically. This is in agreement with the graphs shown in Fig. 7.5. The observed behaviour is characteristic for gel-like samples which show intermittent dynamics. Because of this it is useful to study the behaviour of the sample as a function of age. The two-time correlation function ($G_2(q, t_1, t_2)$) was computed ($q = 0.005$ Å^{-1}), so that the dependence of the dynamics on the sample's age could be investigated. This was performed for both the horizontal and vertical direction, see Fig. 7.7. The composite's dynamics are clearly changing as a function of age. For both directions the dynamics initially are speeding up, after which they slow down again. However, also in $G_2(q, t_1, t_2)$ anisotropy in the behaviour depending on direction was observed. The anisotropy that was observed in Fig. 7.5 as function of direction, is also observed here for the two-time correlation, the system decorrelates faster in the vertical direction than the horizontal direction.

Both the information from $g_2(\tau) - 1$ and $G_2(q, t_1, t_2)$ reveal that the RTa_2a_32 sample has dynamics that are faster in the vertical direction compared to the horizontal direction. The behaviour observed in this wacker-5CB composite is consistent with occasional events and has anisotropic character. The anisotropy can be the result from how the composite is locally arranged. 5CB domains probed can be aligned such that

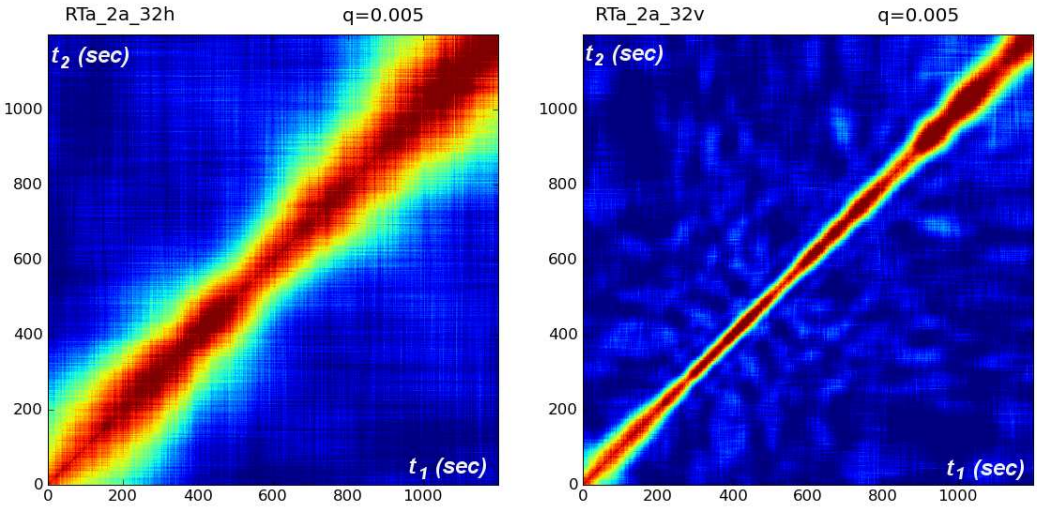

(a) (b)

Figure 7.7: The two-time correlation functions for (a) the horizontal and (b) the vertical direction, for the RTa_2a_32 composite ($q = 0.005$ Å^{-1}). From these graphs it it clear that the system is faster in one direction (vertical) than the other. Not only is there an anisotropy in how fast the system decorrelates, but also there is unusual behaviour in each direction. In both directions the system speeds up, after which it slows down again.

the director is either parallel or perpendicular to the strands of wacker particles.

To investigate the dynamics further the behaviour of the dynamic susceptibility (χ_4) is considered. This quantity describes the variance in the degree of correlation $c_I(t, \tau)$, which describes how much deviation there is from the mean value of correlation at a certain lag time τ, basically how much spread there is in the intensity. When there are homogeneous dynamics, it means that for a certain τ the fluctuations are homogeneous in time, which means that the variance will be small as all the fluctuations will be close to the mean value of the fluctuations. This corresponds to a low value of χ_4. However, when there are heterogeneities in the dynamics, the dynamic susceptibility will change, as the variance in the degree of correlation will change. This does not necessarily have to be true for all τ, but this can be peaked around a certain τ value, mostly the characteristic relaxation time for the system τ_c [172]. For the τ at which the dynamics are observed to be heterogeneous the variance in the degree of correlation is larger, and thus the value of χ_4. The dynamics at τ=τ_c are more strongly heterogeneous, there is intermittency for dynamics with the characteristic relaxation time. There are jumps for the dynamics here, sometimes the intensity is high for fluctuations with this τ_c and sometimes low, leading to the high value of the variance in the degree of correlation (and thus χ_4). Around τ_c the degree of correlation varies more.

For the sample under study here the dynamic susceptibility has been considered

too, to investigate the intermittent behaviour of the system. In Fig. 7.8 the behaviour of χ_4 can be seen.

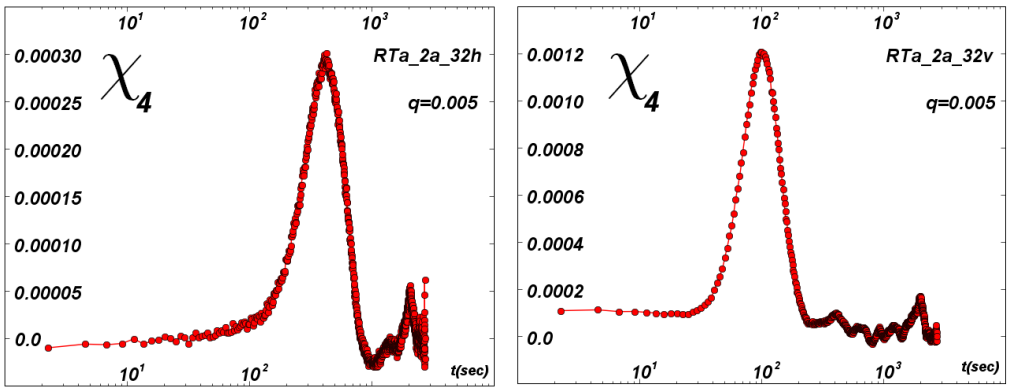

(a) (b)

Figure 7.8: The dynamic susceptibility $\chi_4(\tau)$ for (a) the horizontal and (b) the vertical direction, for the RTa_2a_32 composite ($q = 0.005$ Å^{-1}). $\chi_4(\tau)$ is peaked around the characteristic relaxation time τ_c for both directions. This can be compared with Fig. 7.5, in which it was seen that the system decorrelates at different speeds depending on the direction. The maximum height for $\chi_4(\tau)$ is four times higher in the vertical direction, indicating that there is intermittency to a larger degree compared to the horizontal direction, for which $\chi_4(\tau)$ has a smaller maximum value for $\chi_4(\tau)$.

The first important point here is that again the directional anisotropy is present, not only is χ_4 peaked at different relaxation (lag) times, but also the maximum value of χ_4 varies. Here the maximum value of χ_4 for the vertical direction is larger, indicating more deviations from the mean degree of correlation. This means that there is intermittency to a larger degree compared to the horizontal direction. Secondly, it is important to note that χ_4 has its peak at τ_c, the system's characteristic relaxation time (for that direction).

The composite presented above (RTa_2a_32) shows rich behaviour, like anisotropy and intermittency. Rich behaviour is found in a large range of different composites, that contain different wacker particles (properties), experimental temperature, and history. Certain properties in the behaviour, such as anisotropy and χ_4 behaviour are found to be a returning theme. The highly varied range of results is certainly intriguing. To further illustrate the interesting behaviour of the wacker-5CB composite two more datasets of the 2a_32 composite are presented (different histories than that from RTa_2a_32), and RT_2_100.

7.3.1 Is gravity driving the anisotropy?

In the 2a_32 composite it was observed that dynamics in the vertical direction decorrelate faster compared to those in the horizontal direction. This might be an

indication that sedimentation has an effect on the dynamics in the vertical direction. However, this anisotropy in the dynamics for different directions was not observed to be the same for all composites. Some composites show dynamics that decorrelate faster in the vertical direction such as the RTa_2a_32 composite, but other composites show dynamics that decorrelate faster in the horizontal direction instead. This is illustrated with data obtained for the RT_2_100 composite. After the wacker fumed silica was dispersed in 5CB in the isotropic phase it was stirred for a whole night. Prior to measuring the RT_2_100 composite was filled into a 2mm diameter capillary using a syringe. When analyzing the data, the first obvious result is the anisotropy in the characteristic relaxation time, as found in the curves for g_2. The result here (figs 7.9

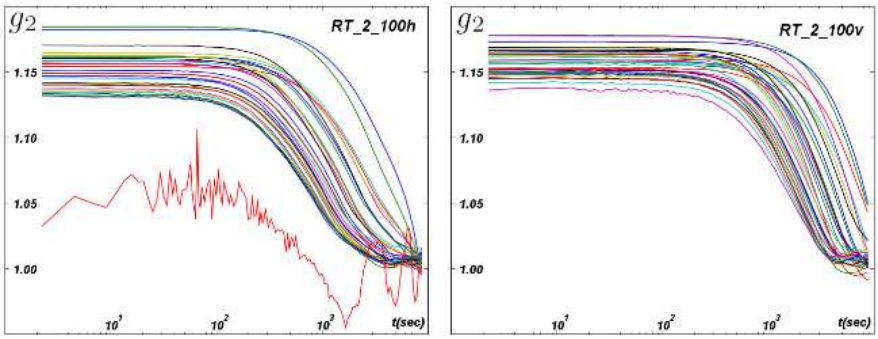

Figure 7.9: The intensity correlation function (g_2) measured for the RT_2_100 composite for both the horizontal and vertical direction. From the graphs can be seen that for both directions the dynamics are slower for smaller (low) q. The dynamics in the horizontal direction decorrelate faster compared to the vertical direction.

and 7.10) is opposite to that for the data presented prior to this dataset (figs. 7.5, 7.7, and 7.8). Here the dynamics in the horizontal direction decorrelate faster than in the vertical direction, which is counter-intuitive, when the effect of gravity is considered. Dynamics in the vertical direction are expected to decorrelate faster, because gravity is working on the system's dynamics in this direction, and intuitively one might expect the dynamics in this direction thus to be faster. The opposite scenario is true for this composite, the dynamics in the horizontal direction are faster. This tells us that the dependence of the speeds of the dynamics on direction is not influenced by gravity, so the cause for this anisotropy must be from the properties of the composite (particle arrangement, nematic director orientation).

The composite shows a dramatic aging for both directions, as can be seen in the graphs for the two-time correlation functions in Fig. 7.10. With age the dynamics decorrelate more slowly in both directions. The examination of χ_4 shows that the composite is intermittent in the horizontal direction, but not in the vertical direction. In the vertical direction there is no evidence of intermittency, χ_4 does not exhibit a

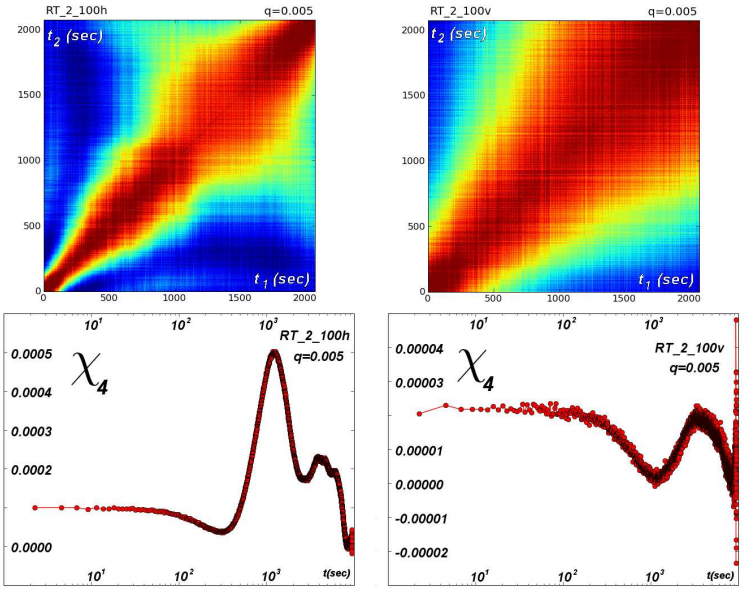

Figure 7.10: Dramatic aging is observed in the RT_2_100 composite for both the horizontal and vertical direction. With age the dynamics decorrelate more slowly. Via examining χ_4 for both directions, it can be observed that the composite shows intermittent behaviour only in the horizontal direction.

peak.

It is clear from the data presented here that sedimentation does not play a crucial role in the decorrelation of the composites' dynamics. No specific influence on the observed behaviour as a function of the surface properties of the silica particles was found.

7.3.2 Does the sample dynamics always slow down with the sample age?

In the wide variety of composites that were measured in the experiments many aspects were observed. For example, the theme of this section, the speeding up and slowing down of the composites' dynamics. So far the presented results mostly indicated that the dynamics slow down with sample age. However, this was not observed in all composites. In several composites it was observed that the dynamics could speed up with age. To illustrate this with an example, results obtained for the RT_2a_32 composite are presented. The capillary was filled approximately 4.5 hours before the measurement was made at room temperature. The first striking observation to be made here is that the aging behaviour is very anisotropic, see Fig. 7.11. In the horizontal direction the dynamics start to decorrelate faster as the composite ages, the dynamics speed up. This contrasts the dynamics for the vertical direction, in which the dynamics are slowing down as the composite ages. The second striking observation

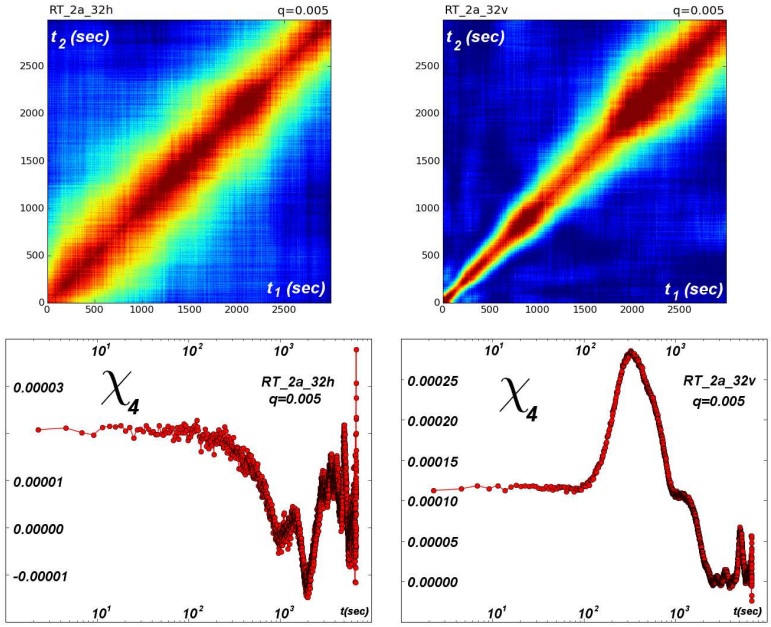

Figure 7.11: The RT_2a_32 composite shown anisotropic behaviour in the dynamics as a function of age. In the horizontal direction the dynamics are speeding up with age, while in the vertical direction the dynamics are slowing down. Intermittent behaviour is only evidenced for the vertical direction.

is in the behaviour of χ_4 for the different directions. In the horizontal direction χ_4 does not exhibit a peak around the characteristic relaxation time (which can be found via examining g_2 (Fig. 7.12)), which means there is no intermittency. This contrasts strongly with the behaviour in the vertical direction, for which χ_4 exhibits a peak around the characteristic relaxation time, evidencing intermittent behaviour.

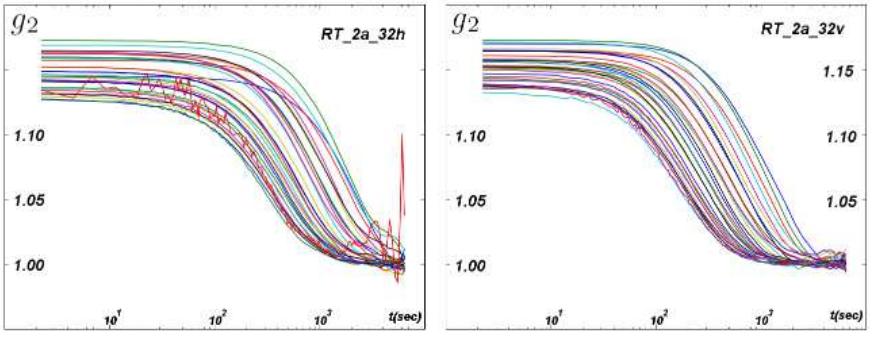

Figure 7.12: The intensity correlation function (g_2) measured for the RT_2a_32 composite for both the horizontal and vertical direction. Decorrelation of the dynamics in the vertical direction is slightly faster than in the horizontal direction.

7.3.3 Is χ_4 always highly anisotropic?

Via accessing the behaviour of χ_4, the dynamic susceptibility, the intermittency of the dynamics can be assessed. Various examples of χ_4 have been presented in the previous sections, in which mostly anisotropy was observed, i.e. the composites show more intermittency in one direction compared with the orthogonal direction. However this does not mean that this is always the case. In this section results are presented for χ_4 that show that intermittency is not always highly anisotropic. This is demonstrated by presenting results obtained for the T50_2a_32 composite. To start, the capillary was filled approximately 4.5 hours prior to measuring the composite at room temperature, after which the composite was heated to 50^{o}C and measured. This data has been analyzed for orthogonal directions in the same manner as described before. After the start of the measurement aging is observed in the composite. The variety in behaviour depending on the direction is again observed, the dynamics in the vertical direction are faster than in the horizontal direction, see Fig. 7.13. When examining the variance

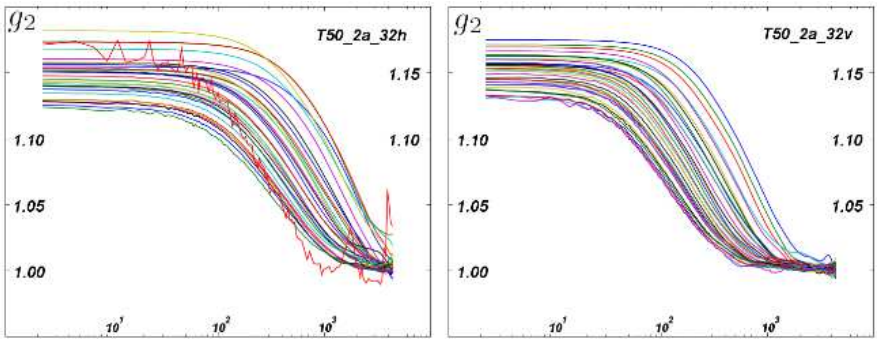

Figure 7.13: The intensity correlation function (g_2) measured for the T50_2a_32 composite for the horizontal and vertical direction. Decorrelation of the dynamics in the vertical direction is somewhat faster than in the horizontal direction.

of the degree of correlation c_I, which corresponds to the dynamic susceptibility χ_4, peaks centered around the characteristic relaxation time are found for both directions. However, for the vertical direction there is a second smaller peak next to the main peak (peak with highest intensity is taken to be the main peak) at $\tau \sim 300$s in the graph of χ_4 vs the delay time, at around $\sim$1000s, see Fig. 7.14. This is most likely to be a result of bad statistics, as at this point the delay time τ is large, which means a smaller amount of data points are considered. To investigate if there is actually a second characteristic relaxation time in the system's dynamics, an experiment lasting for longer would be required, to investigate if the lack of statistics can be ruled out or not.

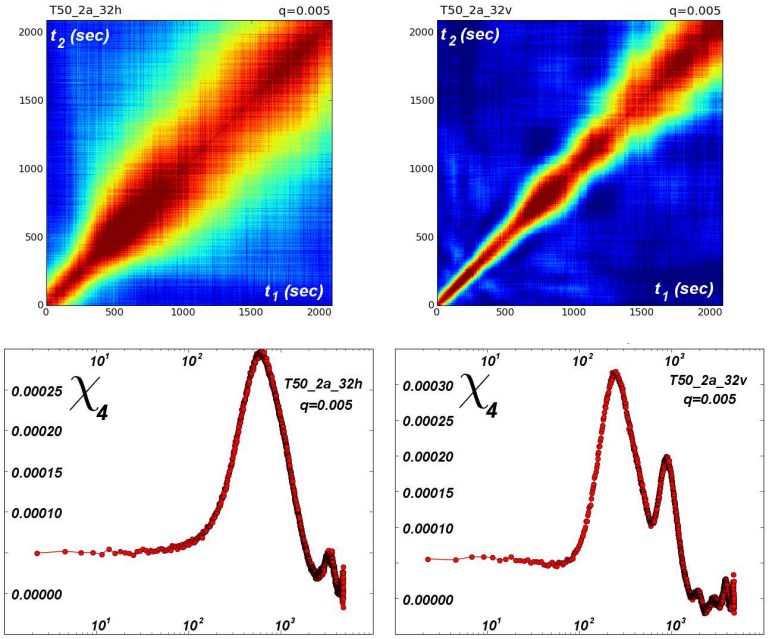

Figure 7.14: Aging in the T50_2a_32 composite is observed for both directions, more dramatic for the horizontal direction than the vertical direction. In both directions intermittent behaviour is observed, evidenced by the peak exhibited by χ_4. The second peak found in the graph for χ_4 in the vertical direction is most likely due to bad statistics and thus not real.

7.3.4 What is regular?

For understanding the behaviour better the fit parameters for g_2-1 are looked at in more detail. As mentioned before, $g_2(\tau) - 1$ is fitted with a function that describes exponential decay $f(q,t) = BL + b \cdot e^{-2(\frac{t}{\tau_c})^{\mu}}$, where BL indicates the value to which the curve decays, and b determines the contrast between the initial and final level of the curve. τ_c indicates the characteristic decay time which determines where the curve falls of indicating how long it takes before the intensity fluctuations decorrelate. μ adjusts the slope of the exponential curve. Values of μ larger than 1.0 implies a faster decay than a normal exponential (compressed exponential), and a value smaller than 1.0 indicates decay that is slower than exponential decay (stretched exponential). From the fitting data the relationship between the wave vector q and the characteristic decay time τ_c and μ can be examined.

The fit parameters for both the horizontal and vertical directions are examined. In the graphs in Fig. 7.15 τ_c versus q is presented for the three different composites discussed in sections 7.3.1 , 7.3.2, and 7.3.3. A first clear observation that can be drawn from the graphs presented here is that $\frac{1}{\tau_c}$ varies linearly with q, indicating that the mechanism(s) responsible for the decorrelation is not of diffusive origin (for which $\frac{1}{\tau_c} \propto q^2$ [174]). This behaviour has been attributed to randomly distributed internal

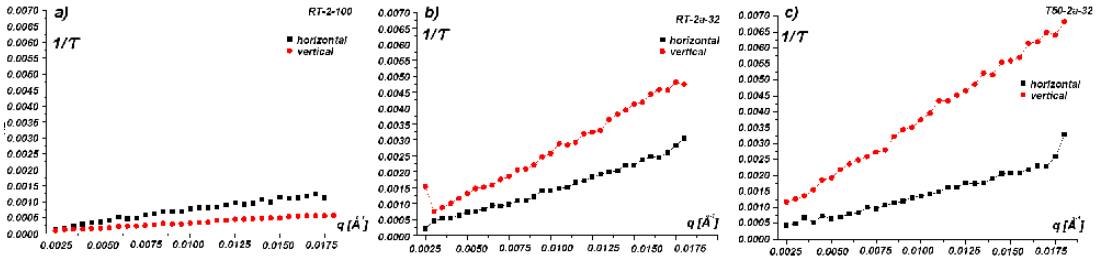

Figure 7.15: τ_c versus q for (a) the RT-2-100 composite, (b) the RT-2a-32 composite, and (c) the T50-2a-32 composite. For all three composites it is observed that $\frac{1}{\tau_c}$ varies linearly with q.

stress sources acting on the composite [174].

In Fig. 7.16 graphs of μ versus q are presented for the three different composites.

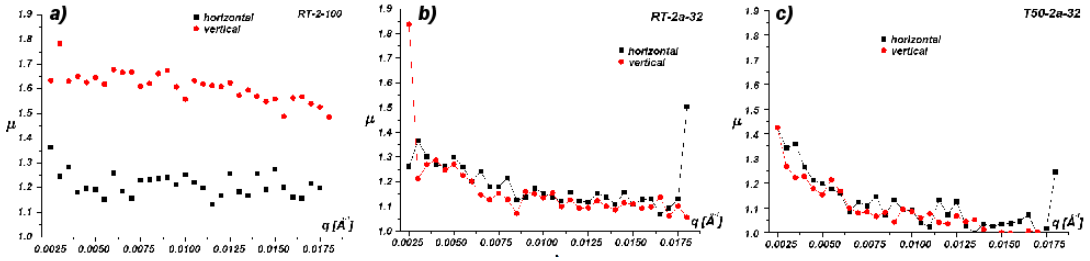

Figure 7.16: μ versus q for (a) the RT-2-100 composite, (b) the RT-2a-32 composite, and (c) the T50-2a-32 composite.

μ tends to be around 1.3 except for RT_2_100v (about 1.6), and in T50_2a_32 there is a slight decrease in μ from about 1.4 to 1 with increasing wave vector q for both directions. The character of the relaxation for the RT_2_100 composite in the vertical direction (μ ∼1.6) is thus different from the other direction for which μ ∼1.3. For the T50_2a_32 composite the mode of relaxation depends in the wave vector q, with increasing wave vector μ decreases from about 1.4 to 1. The exponent μ>1 indicates a decorrelation which is faster than exponential. Linear $\frac{1}{\tau_c}$ versus q and μ>1 have often been associated with intermittent dynamics [179].

7.4 Conclusion

From the data presented here it is clear that the systems show very interesting and varied behaviour. The composite's dynamics are very heterogeneous and show intermittent behaviour, evidenced by the behaviour of χ_4. Non-diffusive motion is evidenced via $1/\tau$ vs q [174].

The fact that the results are so highly varied can result from the length scales in this system. The beam spot size used in the experiment is 20μmx20μm, and the silica

agglomerates have various sizes, ranging from ∼20nm to ∼1-2.5μm depending on if the diameter is measured about the long or short side. See Fig. 6.7 on page 110 for a representative image of a silica agglomerate. The results will be strongly dependent on the location of the beam in the sample. In the volume probed by the beam spot however only $2\%_v$ consists of silica agglomerates. See the following schematic for illustration on this point: In the figure only the area is schematically represented, to illustrate

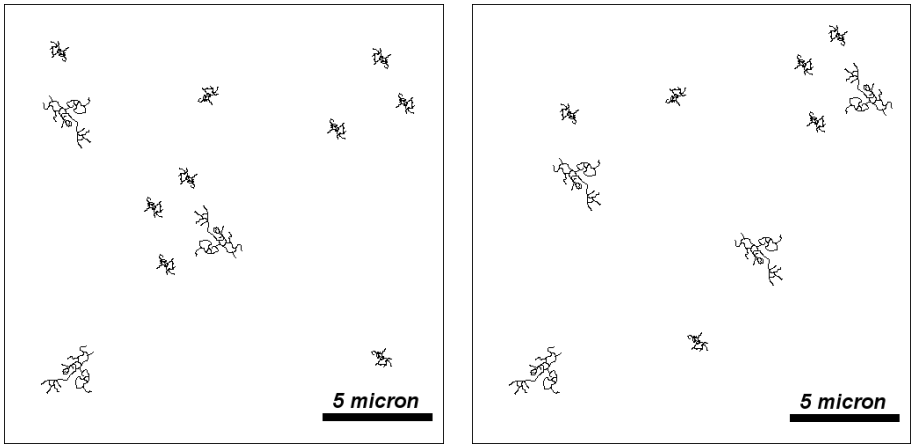

(a) (b)

Figure 7.17: Schematic representation of the area probed by a beam spot of the size 20μmx20μm. The volume consisting of silica in (a) and (b) is the same, but the arrangement is different, which can lead to different results.

the inhomogeneous distribution of the silica in the liquid crystal. The results obtained in the scattering experiment will strongly depend on how the silica agglomerates are arranged in the liquid crystal in the volume probed. From the schematic it is clear, that if rearrangement takes place in the silica gel, intermittency will be observed. This is because there is only a finite number of aggregates in the probed volume. When one agglomerate breaks a bond the dynamics change a lot during this event, resulting in that χ_4 exhibits a peak. The peak is observed to be at the characteristic relaxation time of the dynamics, because the event causes the variance for c_I to be large. After the rearrangement the dynamics can be different. In some two-time correlation functions a rearrangement can be observed (Fig. 7.10 horizontal direction), and the dynamics can be slower or faster after the rearrangement compared to before the rearrangement. The anisotropy that is observed in the data depending on the direction results from the fact that the volume probed is heterogeneous because of the way the silica is arranged in the sample. As said before, the particles exist in large agglomerates and are thus not homogeneously dispersed over the sample. The observed dynamics depend on how the arrangement of the composite is in the volume probed during the experiment. The

dynamics in one direction, horizontal or vertical, can be faster or slower than in the orthogonal direction. It is demonstrated that this is not caused by gravity effects, but by how the composite relaxes (and rearranges) during the experiment.

The motion of the silica in the liquid crystal is observed to be non-diffusive as evidenced by the behaviour of $1/\tau$ vs q [174]. The surface of the silica particles is covered with both hydroxyl and methyl groups. The hydroxyl groups give the particles the ability to form hydrogen bonds with each other and thus form agglomerates. Because of this the gel can be formed, and diffusion is prohibited. The gel however is obviously not rigid, the dynamics change with age and intermittency is observed. The composite can age in time, which means that the configuration at the start of the measurement is not in equilibrium. When the composite is prepared and injected into the capillary the silica agglomerates have a certain configuration which is not necessarily energetically the most favorable. The hydrophilic surface of the particles induces homeotropic anchoring of the 5CB molecules at the surface, which means disorder in the liquid crystal is induced. The liquid crystal also acts on the particles [42]. When the liquid crystal molecules are attempting to arrange themselves to form a nematic phase this has an effect on the silica particles. Over time stress can build up in the composite, the liquid crystal molecules attempt to arrange themselves in a certain way depending on the temperature and the silica particles form agglomerates because of hydrogen bonding. The stress build-up leads to the aging of the composite, the silica particles get closer to each other because of the hydrogen bonding. After sufficient build up of internal stress the gel 'yields' which means that rearrangements take place which gives rise to the observed intermittent behaviour.

Chapter 8

Conclusions and future work

From our studies we can conclude that the PMMA colloids are influenced by the microemulsion system at every stage. This is from pre-transitional effects through to late stage coarsening. By contrast the behaviour of silica particles are only sensitive to the gross alignment of the liquid crystal and not at all to the details of the transition. We conclude that:

- The PMMA colloids preferentially partition into the micellar gas phase.
- During an off-critical quench dodecane pre-wets the PMMA surface.
- The apparent wetting layer at a later stage is in fact due to heterogeneous nucleation.
- The presence of both PMMA colloids and creaming strongly modify the coarsening behaviour after phase separation.
- Late stage coarsening in the PMMA-microemulsion system has viscoelastic character.
- Silica particles aggregate strongly in 5CB even in the case of a high surface coverage of methyl groups.
- The aggregation behaviour is apparent via static probes and via bulk rheology.
- The locally anisotropic nature of the silica-5CB gel is reflected in the anisotropic dynamics.

The heterogeneous nature of these systems makes them challenging to study. We will review this aspect before looking at potential new directions.

8.1 Microemulsion-PMMA

In the experiments performed in the off-critical regime it proved difficult to study the growth of the PMMA clusters quantitatively. It was attempted to study the cluster growth as a function of warming rate and colloid concentration. Due to the significant density difference between the various constituents the system was very mobile. Less

dense components move to the top of the sample cell while more dense components sediment. Clusters move in and out of focus during microscopy experiments prohibiting the possibility of careful size determination. To improve the prospect of a study of the cluster growth, buoyancy matching or using smaller colloids might prove useful. In this system this can only be achieved via modifying the particles that are inserted in the microemulsion. Buoyancy matching might also facilitate making qualitative measurements in the critical regime. It would be interesting to examine the influence of the PMMA concentration on the growth rate of the spinodal domains during phase separation.

This system could provide a convenient tool for investigating coalescence dynamics, because the colloid and micelle concentration can be tuned. The rate of coalescence between droplets depends on how fast the liquid in between the droplets can drain from the region in between them. The draining progresses more slowly when the liquid situated between adjacent droplets has a higher viscosity, a property that can be tuned in the microemulsion system.

8.2 Silica-5CB

The structure of the silica-5CB composite is thoroughly investigated in this thesis, however some questions remained unanswered. In the FFDI investigations it is not completely determined what structure exactly is responsible for the appearance of the spherical features observed. This is also true for the spherical features sticking out of the frozen film. For full understanding the structure of the silica-5CB composite it is necessary to repeat the investigation to examine the structure of 5CB without silica nanoparticles embedded in it.

The composite's dynamics are observed to be very heterogeneous and show intermittent behavior. It is clear from the electron microscopy investigation that the sample is dynamically heterogeneous on the scale of the beam spot size. The silica is arranged in the 5CB as agglomerates that are distributed over the volume. This could possibly be controlled by changing the mixing procedure. It would be interesting to investigate the effect of a more homogeneous distribution of silica nanoparticles on the composite's dynamics. This could be instructive regarding the observed anisotropy in the composite's dynamics studied in this thesis.

8.3 New directions

It would be of great interest to study a composite with a character intermediate between these two. It would be curious to have particle-particle attractions that can be overcome

during the phase transition but which are not completely dominated by it. Here we might see a more subtle interplay.

It would also be valuable to study pre-transitional effects in colloidal systems with the use of laser-tweezers. Using this technique pre-wetting effects might be visible as a change to the dynamics of a trapped particle. We recognize that such experiments present formidable practical challenges.

Further studies could focus on the PMMA-microemulsion system as it dries in a controlled manner in a thin film geometry. Here the steady increase in the volume fraction of the non-volatile components would present a new drive for composite self-organization.

Bibliography

[1] M. E. Cates, M. R. Evans, eds., Soft and Fragile Matter, p. 1-3, Institute of Physics, 2000.

[2] R. A. L. Jones, Soft Condensed Matter, Oxford University Press, 2002.

[3] P. G. Debenedetti, Metastable Liquids: Concepts and Principles, Princeton University Press, 1996.

[4] P. M. Chaikin, T. C. Lubensky, Principles of condensed matter physics, Cambridge University Press, 1995.

[5] I. W. Hamley, Introduction to Soft Matter Revised Edition Synthetic and Biological Self-Assembling Materials, John Wiley & Sons, Ltd, 2007.

[6] J. M. Yeomans, Statistical mechanics of phase transitions, Oxford University Press, 1992.

[7] A. Kumar, H. R. Krishnamurthy, E. S. R. Gopal, *Physics Reports* **98** (1983) 57–143.

[8] T. C. Frank, F. A. Donate, A. S. Merenov, G. A. V. Wald, B. J. Alstad, C. W. Green, T. C. Thyne, *Ind. Eng. Chem. Res.* **46** (2007) 3774–3786.

[9] A. M. Bellocq, D. Gazeau, *J. Phys. Chem.* **94** (1990) 8933–8938.

[10] M. J. Rosen, Surfactants and Interfacial Phenomena, John Wiley & Sons, Ltd, 2004.

[11] T. C. ed., Colloid Science: Principles, Methods and Applications, Blackwell Publishing Ltd, 2005.

[12] C. L. Liu, Y. J. Nikas, D. Blankschtein, *Biotechnol. Bioeng.* **52** (1996) 185–192.

[13] M. Fanun, ed., Microemulsions: Properties and Applications, CRC Press, 2009.

[14] T. P. Hoar, J. H. Schulman, *Nature* **152** (1943) 102–103.

[15] P. Winsor, *Trans. Faraday Soc.* **44** (1948) 376398.

[16] D. Langevin, *Adv. Coll. Int. Sci.* **34** (1991) 583–595.

[17] D. Roux, A. M. Bellocq, M. S. Leblanc, *Chem. Phys. Lett.* **94** (1983) 156–161.

[18] A. Ponton, R. Nozaki, T. K. Bose, *J. Chem. Phys.* **97** (1992) 8515–8521.

[19] G. S. Grest, I. Webman, S. A. Safran, A. L. R. Bug, *Phys. Rev. A* **33** (1986) 2842–2845.

[20] S. A. Safran, I. Webman, G. S. Grest, *Phys. Rev. A* **32** (1985) 506–511.

[21] P. de Gennes, C. Taupin, *J. Phys. Chem.* **86** (1982) 2294–2304.

[22] S. A. Safran, L. A. Turkevich, *Phys. Rev. Lett.* **50** (1983) 1930–1933.

[23] S. Brunetti, D. Roux, A. M. Bellocq, G. Fourche, P. Bothorel, *J. Phys. Chem.* **87** (1983) 1028–1034.

[24] J. S. Huang, S. A. Safran, M. W. Kim, G. S. Grest, M. Kotlarchyk, N. Quirke, *Phys. Rev. Lett.* **53** (1984) 592–595.

[25] P. I. Fletcher, A. M. Howe, B. H. Robinson, *J. Chem. Soc., Faraday Trans. 1* **83** (1987) 985–1006.

[26] A. M. Bellocq, D. Roux, 'Microemulsions', ed. S. Friberg, P. Bothorel, CRC Press, 1987.

[27] G. Fourche, A.-M. Bellocq, S. Brunetti, *J. Coll. Int. Sci.* **88** (1982) 302–307.

[28] P. Dorion, J. R. Lalanne, B. Pouligny, S. Imaizumi, C. W. Garland, *J. Chem. Phys.* **87** (1987) 578–588.

[29] N. Rebbouh, J. R. Lalanne, *J. Chem. Phys.* **90** (1989) 1175–1187.

[30] D. Roux, A. M. Bellocq, *Phys. Rev. Lett.* **52** (1984) 1895–1898.

[31] A. M. Bellocq, P. Honorat, D. Roux, *J. Physique* **46** (1985) 743–748.

[32] D. Roux, *J. Physique* **47** (1986) 733–738.

[33] N. Rebbouh, D. Beysens, J. R. Lalanne, *J. Chem. Phys.* **93** (1990) 9026–9030.

[34] V. M. Starov, M. G. Velarde, C. J. Radke, Wetting and Spreading Dynamics, CRC Press, 2007.

[35] B. M. Law, *Prog. Surf. Sci.* **66** (2001) 159–216.

[36] J. W. Cahn, *J. Chem. Phys.* **66** (1977) 3667–3672.

[37] H. T. Dobbs, J. M. Yeomans, *J. Phys.: Cond. Matter* **4** (1992) 10133–10138.

[38] P. G. de Gennes, J. Prost, The Physics of Liquid Crystals, Oxford University Press, 1993.

[39] I. Dierking, Textures of Liquid Crystals, Wiley-VCH Verlag, 2003.

[40] S. Singh, Liquid Crystals: Fundamentals, World Scientific Publishing, 2002.

[41] J. Cleaver, W. C. K. Poon, *J. Phys.: Condens. Matter* **16** (2004) S1901–S1909.

[42] M. Kreuzer, T. Tschudi, W. H. de Jeu, R. Eidenschink, *Appl. Phys. Lett.* **62** (1993) 1712–1714.

[43] J. L. West, A. Glushchenko, G. Liao, Y. Reznikov, D. Andrienko, M. P. Allen, *Phys. Rev. E* **66** (2002) 012702–1 – 012702–4.

[44] I. Muševic, M. Škarabot, *Soft Matt.* **4** (2008) 195–199.

[45] H. Stark, *Phys. Rep.* **351** (2001) 387–474.

[46] R. W. Ruhwandl, E. M. Terentjev, *Phys. Rev. E* **55** (1997) 2958–2961.

[47] S. P. Meeker, W. C. K. Poon, J. Crain, E. M. Terentjev, *Phys. Rev. E* **61** (2000) R6083–R6086.

[48] P. Poulin, D. A. Weitz, *Phys. Rev. E* **57** (1998) 626 – 637.

[49] R. W. Ruhwandl, E. M. Terentjev, *Phys. Rev. E* **56** (1997) 5561–5565.

[50] M. Marinelli, A. K. Gosh, F. Mercuri, *Phys. Rev. E* **63** (2001) 061713–1 – 061713–9.

[51] F. Mercuri, A. K. Ghosh, M. Marinelli, *Phys. Rev. E* **60** (1999) R6309–R6312.

[52] M. Abramovitz, Microscope, Basics and Beyond, Olympus America Inc., 2003.

[53] D. B. Murphy, Fundamentals of light microscopy and electronic imaging, Wiley-Liss, Inc., 2001.

[54] T. R. Corle, G. S. Kino, Confocal Scanning Optical Microscopy and Related Imaging Systems, Academic Press, San Diego, 1996.

[55] L. Isa, Capillary flow of dense colloidal suspensions, PhD thesis, University of Edinburgh, 2007.

[56] M. Brenner, *American Laboratory* **26** (1994) 14–19.

[57] J. B. Pawley, Handbook of Biological Confocal Microscopy, Spinger-Verlag, New York, 3rd ed., 2006.

[58] A. R. Clarke, C. N. Eberhardt, Microscopy Techniques for Material Science, Woodhead Publishing Ltd. and CRC Press LLC, 2002.

[59] M. Minsky, *Scanning* **10** (1988) 128–138.

[60] D. Chescoe, P. J. Goodhew, The Operation of Transmission and Scanning Electron Microscopes, Oxford University Press, 1990.

[61] L. Belkoura, C. Stubenrach, R. Strey, *Langmuir* **20** (2004) 4391–4399.

[62] A. Baszkin, W. Norde, Physical Chemistry of Biological Interfaces, Marcel Dekker, Inc., 2000.

[63] J. Dubochet, M. Groom, S. Mueller-Neuteboom, *Advances in optical and electron microscopy* **8** (1982) 107–135.

[64] S. M. Bailey, J. A. Zasadzinski, *J. Microsc.* **163** (1991) 307–320.

[65] S. Burauer, L. Belkoura, C. Studenrauch, R. Strey, *Coll. Surf. A* **228** (2003) 159–170.

[66] H. W. Meyer, W. Richter, *Micron* **32** (2001) 615–644.

[67] W. Jahn, R. Strey, *J. Phys. Chem.* **92** (1988) 2294–2301.

[68] P. N. Pusey, D. E. Koppel, D. W. Schaefer, R. D. Camerini, S. Koenig, *Biochem.* **13** (1974) 952–960.

[69] O. Glatter, O. K. eds., Small Angle X-ray Scattering, Academic Press Inc. (London) Ltd., 1982.

[70] P. Lindner, T. Z. eds., Neutrons, X-rays and Light: Scattering Methods Applied to Soft Condensed Matter, Elsevier, 2002.

[71] A. Robert, Dynamic Behavior of Charge Stabilized Colloidal Suspensions, PhD thesis, Université Joseph Fourier-Grenoble I, 2001.

[72] R. Borsali, R. P. eds., Soft Matter Characterization, Springer Science+Business Media, LLC., 2008.

[73] J. C. S. Johnson, D. A. Gabriel, Laser Light Scattering, Dover Publications, Inc. New York, 1981.

[74] L. Cipelletti, H. Bissig, V. Trappe, P. Ballesta, S. Mazoyer, *J. Phys.: Condens. Matter* **15** (2003) S257–S262.

[75] M. Sutton, K. Laaziri, F. Livet, F. Bley, *Optics Express* **11** (2003) 2268–2277.

[76] A. Fluerasu, A. Moussaïd, A. Madsen, A. Schofield, *Phys. Rev. E* **76** (2007) 010401–1 – 010401–4.

[77] E. M. Herzig, Bijel a novel composite material from colloids on liquid-liquid interfaces, PhD thesis, University of Edinburgh, 2008.

[78] http://www.esrf.eu/UsersAndScience/Experiments/SoftMatter/ID10A.

[79] G. Grübel, F. Zontone, *J. Alloys Compd.* **362** (2004) 3–11.

[80] D. Lumma, L. B. Lurio, S. G. J. Mochrie, *Rev. Sci. Instrum.* **71** (2000) 3274–3289.

[81] P. Falus, L. B. Lurio, S. G. J. Mochrie, *J. Synchotron Rad.* **13** (2006) 253–259.

[82] I. Sikharulidze, Dynamics of smectic membranes as studied by X-ray nd neutron scattering, PhD thesis, FOM-Institute for Atomic and Molecular Physics, Amsterdam, 2005.

[83] P. R. Bevington, D. K. Robinson, Data Reduction and Error Analysis for the Physical Sciences, Mc Graw Hill, 2nd Ed, 1992.

[84] C. W. Macosko, Rheology: Principles, Measurements and Applications, Wiley-VCH, 1994.

[85] R. G. Larson, The Structure and Rheology of Complex Fluids, Oxford University Press, Inc., 1999.

[86] J. F. Steffe, Rheological Methods in Food Process Engineering, Freeman Press, USA, 1996.

[87] P. D. Gallagher, M. L. Kurnaz, J. V. Maher, *Phys. Rev. A* **46** (1992) 7750–7755.

[88] M. L. Kurnaz, J. V. Maher, *Phys. Rev. E* **55** (1997) 572–576.

[89] C. Hertlein, L. Helden, A. Gambassi, S. Dietrich, C. Bechinger, *Nature* **451** (2008) 172–175.

[90] F. Schlesener, A. Hanke, S. Dietrich, *J. Stat Phys.* **110** (2003) 981–1013.

[91] M. E. Fisher, P.-G. de Gennes, *C. R. Acad. Sci. Paris B* **287** (1978) 207–209.

[92] H. Löwen, *Phys. Rev. Lett.* **74** (1995) 1028–1031.

[93] V. Gurfein, D. Beysens, F. Perrot, *Phys. Rev. A* **40** (1989) 2543–2546.

[94] R. D. Koehler, E. W. Kaler, *Langmuir* **13** (1997) 2463–2470.

[95] T. J. Sluckin, *Phys. Rev. A* **41** (1990) 960–964.

[96] Y. Jayalakshmi, E. W. Kaler, *Phys. Rev. Lett.* **78** (1997) 1379–1382.

[97] S. R. Kline, E. W. Kaler, *Langmuir* **10** (1994) 412–417.

[98] V. Gurfein, F. Perrot, D. Beysens, *J. Coll. Int. Sci.* **149** (1992) 373–378.

[99] B. M. Law, J.-M. Petit, D. Beysens, *Phys. Rev. E* **57** (1998) 5782–5794.

[100] J.-M. Petit, B. M. Law, D. Beysens, *J. Coll. Int. Sci.* **202** (1998) 441–449.

[101] D. Beysens, D. Estéve, *Phys. Rev. Lett.* **54** (1985) 2123–2126.

[102] J. S. van Duijneveldt, D. Beysens, *J. Chem. Phys.* **94** (1991) 5222–5225.

[103] T. Narayanan, J.-M. Petit, M. L. Broide, D. Beysens, *Phys. Rev. E* **51** (1995) 4580–4584.

[104] M. L. Broide, Y. Garrabos, D. Beysens, *Phys. Rev. E* **47** (1993) 3768–3771.

[105] D. Beysens, T. Narayanan, *J. Stat. Phys.* **95** (1999) 997–1008.

[106] T. Narayanan, A. Kumar, E. S. R. Gopal, D. Beysens, P. Guenoun, G. Zalczer, *Phys. Rev. E* **48** (1993) 1989–1994.

[107] A. Kumar, D. Beysens, *Physica A* **224** (1996) 68–73.

[108] N. Rebbouh, J. Hamelin, T. K. Bose, J. Thoen, *J. Chem. Phys.* **96** (1992) 8470–8476.

[109] P. D. Gallagher, J. V. Maher, *Phys. Rev. A* **46** (1992) 2012–2021.

[110] B. Rathke, H. Grüll, D. Woermann, *J. Coll. Int. Sci.* **192** (1997) 334–337.

[111] M. F. Shu, E. R. Dufresne, D. A. Weitz, *Langmuir* **21** (2005) 4881–4887.

[112] G. S. Roberts, R. Sanchez, R. Kemp, T. Wood, P. Bartlett, *Langmuir* **24** (2008) 6530–6541.

[113] G. Petekidis, L. A. Galloway, S. U. Egelhaaf, M. E. Cates, W. C. K. Poon, *Langmuir* **18** (2002) 4248–4257.

[114] F. Soyka, O. Zvyagolskaya, C. Hertlein, L. Helden, C. Bechinger, *Phys. Rev. Lett.* **101** (2008) 208301–1 – 208301–4.

[115] H. Gue, T. Narayanan, M. Sztuchi, P. Schall, G. H. Wegdam, *Phys. Rev. Lett.* **100** (2008) 188303–1 – 188303–4.

[116] X. Lu, S. G. J. Mochrie, S. Narayanan, A. R. Sandy, M. Sprung, *Phys. Rev. Lett.* **100** (2008) 045701–1 – 045701–4.

[117] Q. Wu, F. A. Merchant, K. R. Castleman, Microscope Image Processing, Elsevier, 2008.

[118] H. Tanaka, T. Miura, *Phys. Rev. Lett.* **71** (1993) 2244–2247.

[119] H. Tanaka, *J. Chem. Phys.* **100** (1994) 5323–5337.

[120] M. Laradji, M. J. A. Hore, *J. Chem. Phys.* **121** (2004) 10641–10647.

[121] H. Tanaka, *J. Phys.: Condens. Matter* **12** (2000) R207–R264.

[122] H. Tanaka, T. Koyama, T. Araki, *J. Phys.: Cond. Matter* **15** (2003) S387–S393.

[123] M. Buzzacchi, P. Schmiedel, W. von Rybinski, *Coll. Surf. A: Physicochem. Eng. Asp.* **273** (2006) 47–54.

[124] S. N. Tan, D. Fornasiero, R. Sedev, J. Ralston, *J. Coll. Int. Sci.* **286** (2005) 719–729.

[125] N. Louvet, F. Rouyer, O. Pitois, *J. Coll. Int. Sci.* **334** (2009) 82–86.

[126] B. S. Murray, R. Ettelaie, *Curr. Opin. Coll. Int. Sci.* **9** (2004) 314–320.

[127] I. B. Ivanov, *Pure Appl. Chem.* **52** (1980) 1241–1262.

[128] D. Li, *J. Coll. Int. Sci* **181** (1996) 34–44.

[129] D. G. A. L. Aarts, H. N. W. Lekkerkerker, H. Guo, G. H. Wegdam, D. Bonn, *Phys. Rev. Lett.* **95** (2005) 164503–1 – 164503–4.

[130] D. G. A. L. Aarts, H. N. W. Lekkerkerker, *J. Fluid Mech.* **606** (2008) 275–294.

[131] A. C. Balazs, *Curr. Opin. Coll. Int. Sci.* **4** (2000) 443–448.

[132] H. Tanaka, A. J. Lovinger, D. D. Davis, *Phys. Rev. Lett.* **72** (1994) 2581–2584.

[133] H. Tanaka, *J. Phys.: Condens. Matter* **13** (2001) 4637–4674.

[134] A. Karim, J. F. Douglas, G. Nisato, D.-W. Liu, E. J. Amis, *Macromolecules* **32** (1999) 5917–5924.

[135] H.-J. Chung, A. Taubert, R. D. Deshmukh, R. J. Composto, *Europhys. Lett.* **68** (2004) 219–225.

[136] Y.-L. Tang, Y.-Q. Ma, *J. Chem. Phys.* **116** (2002) 7719–7723.

[137] B. P. Lee, J. F. Douglas, S. C. Glotzer, *Phys. Rev. E* **60** (1999) 5812–5822.

[138] H. Tanaka, T. Araki, *Europhys. Lett.* **51** (2000) 154–160.

[139] T. Araki, H. Tanaka, *Phys. Rev. E* **73** (2006) 061506–1 – 061506–7.

[140] T. Araki, H. Tanaka, *J. Phys.: Condens. Matter* **20** (2008) 072101–1 – 072101–6.

[141] M. Rex, C. P. Royall, A. van Blaaderen, H. Lowen, Lane formation in driven colloidal mixtures: is it continuous or discontinuous? (2008).
URL `http://www.citebase.org/abstract?id=oai:arXiv.org:0812.0908`

[142] M. Rex, H. Löwen, *Eur. Phys. J. E* **26** (2008) 143–150.

[143] M. Rex, H. Löwen, *Phys. Rev. E* **75** (2007) 051402–1 – 051402–10.

[144] J. Chakrabarti, J. Dzubiella, H. Löwen, *Phys. Rev. E* **70** (2004) 012401–1 – 012401–4.

[145] J. Dzubiella, G. P. Hoffmann, H. Löwen, *Phys. Rev. E* **65** (2002) 021402–1 – 021402–8.

[146] K. R. Sütterlin, A. Wysocky, A. V. Ivlev, C. Räth, H. M. Thomas, M. Rubin-Zuzic, W. J. Goedheer, V. E. Fortov, A. M. Lipaev, V. I. Molotkov, O. F. Petrov, G. E. Morfill, H. Löwen, *Phys. Rev. Lett.* **102** (2009) 085003–1 – 085003–4.

[147] H. Tanaka, *Macromol.* **25** (1992) 6377–6380.

[148] B. Binks, T. Horozov, Colloidal Particles at Liquid Interfaces, Chapter 1, 1-74, Cambridge University Press, 2006.

[149] M. Y. Lin, H. M. Lindsay, D. A. Weitz, R. C. Ball, R. Klein, P. Meakin, *Nature* **339** (1989) 360–362.

[150] G. S. Iannacchione, C. W. Garland, J. M. Tang, T. P. Rieker, *Phys. Rev. E* **58** (1998) 5966–5981.

[151] G. Beaucage, *J. Appl. Cryst.* **28** (1995) 717–728.

[152] P. Sollich, F. Lequeux, P. Hébraud, M. E. Cates, *Phys. Rev. Lett.* **78** (1997) 2020–2023.

[153] M. Cloitre, R. Borrega, L. Leibler, *Phys. Rev. Lett.* **85** (2000) 4819–4822.

[154] R. Bandyopadhyay, D. Liang, R. H. Colby, J. L. Harden, R. L. Leheny, *Phys. Rev. Lett.* **94** (2005) 107801–1 – 107801–4.

[155] I. I. Gnatyuk, G. A. Puchkovskaya, Y. G. Gohsov, L. A. Matkovskaya, M. Drozd, *J. Therm. Anal. Calorim.* **62** (2000) 365–371.

[156] http://www.wacker.com/cms/media/publications/downloads/6174_EN.pdf.

[157] O. Mondain-Monval, *Curr. Opin. Coll. Int. Sci.* **10** (2005) 250–255.

[158] L. H. Margaritis, A. Elgsaeter, D. Branton, *J. Cell Biol.* **72** (1977) 47–56.

[159] P. Moreau, L. Navailles, J. Giermanska-Kahn, O. Mondain-Monval, F. Nallet, D. Roux, *Europhys. Lett.* **73** (2006) 49–54.

[160] K. Miyazaki, H. M. Wyss, D. A. Weitz, D. R. Reichmann, *Europhys. Lett.* **75** (2006) 915–921.

[161] V. J. Anderson, E. M. Terentjev, S. P. Meeker, J. Crain, W. C. K. Poon, *Eur. Phys. J. E* **4** (2001) 11–20.

[162] P. G. Petrov, E. M. Terentjev, *Langmuir* **17** (2001) 2942–2949.

[163] A. Hourri, T. K. Bose, J. Thoen, *Phys. Rev. E* **63** (2001) 051702–1 – 051702–6.

[164] A. Glushchenko, H. Kresse, V. Reshetnyak, Y. Reznikov, O. Yaroshchuk, *Liq. Cryst.* **23** (1997) 241–246.

[165] T. Jin, D. Finotello, *Phys. Rev. Lett.* **86** (2001) 818–821.

[166] T. Jin, D. Finotello, *Phys. Rev. E* **69** (2004) 041704–1 – 041704–12.

[167] B. Zhou, G. S. Iannacchione, C. W. Garland, T. Bellini, *Phys. Rev. E* **55** (1997) 2962–2968.

[168] M. Caggioni, A. Roshi, S. Barjami, F. Mantegazza, G. S. Ianncchione, T. Bellini, *Phys. Rev. Lett.* **93** (2004) 127801–1 – 127801–4.

[169] A. Arcioni, C. Bacchiocchi, I. Vecchi, G. Venditti, C. Zannoni, *Chem. Phys. Lett.* **396** (2004) 433–441.

[170] F. N. Aliev, G. P. Singha, M. Kreuzer, *Mol. Cryst. Liq. Cryst.* **359** (2001) 217–230.

[171] M. A. Zaki-Ewis, G. Nabil, B. Stoll, S. Herminghaus, *Liq. Cryst.* **30** (2003) 1241–1250.

[172] P. Ballesta, A. Durì, L. Cipelletti, *Nature Physics* **4** (2008) 550–554.

[173] E. Wandersman, A. Duri, A. Robert, E. Dubois, V. Dupuis, R. Perzynski, *J. Phys.: Cond. Matt.* **20** (2008) 155104–1 – 155104–7.

[174] L. Cipelletti, L. Ramos, *J. Phys.: Cond. Matt.* **17** (2005) R253–R285.

[175] P. Mayer, H. Bissig, L. Berthier, L. Cipelletti, J. P. Garrahan, P. Sollich, V. Trappe, *Phys. Rev. Lett.* **93** (2004) 115701–1 – 115701–4.

[176] A. Malik, A. R. Sandy, L. B. Lurio, G. B. Stephenson, S. G. J. Mochrie, I. McNulty, M. Sutton, *Phys. Rev. Lett.* **81** (1998) 5832–5835.

[177] F. Livet, F. Bley, R. Caudron, E. Geissler, D. Abernathy, C. Detlefs, G. Grübel, *Phys. Rev. E* **63** (2001) 036108–1 – 036108–7.

[178] C. C. Retsch, I. McNulty, G. S. Iannacchione, *Phys. Rev. E.* **65** (2002) 032701–1 – 032701–4.

[179] A. Durì, L. Cipelletti, *Europhys. Lett.* **76** (2006) 972–978.

[180] J.-P. Bouchaud, E. Pitard, *Eur. Phys. J. E* **9** (2002) 287–291.

[181] L. Cipelletti, S. Manley, R. C. Ball, D. A. Weitz, *Phys. Rev. Lett.* **84** (2000) 2275–2278.

[182] T. Bellini, N. A. Clark, V. Degiorgio, F. Mantegazza, G. Natale, *Phys. Rev. E* **57** (1998) 2996–3006.

[183] A. Durì, H. Bissig, V. Trappe, L. Cipelletti, *Phys. Rev. E* **72** (2005) 051401–1 – 051401–17.